



저작자표시-비영리-변경금지 2.0 대한민국

이용자는 아래의 조건을 따르는 경우에 한하여 자유롭게

- 이 저작물을 복제, 배포, 전송, 전시, 공연 및 방송할 수 있습니다.

다음과 같은 조건을 따라야 합니다:



저작자표시. 귀하는 원저작자를 표시하여야 합니다.



비영리. 귀하는 이 저작물을 영리 목적으로 이용할 수 없습니다.



변경금지. 귀하는 이 저작물을 개작, 변형 또는 가공할 수 없습니다.

- 귀하는, 이 저작물의 재이용이나 배포의 경우, 이 저작물에 적용된 이용허락조건을 명확하게 나타내어야 합니다.
- 저작권자로부터 별도의 허가를 받으면 이러한 조건들은 적용되지 않습니다.

저작권법에 따른 이용자의 권리는 위의 내용에 의하여 영향을 받지 않습니다.

이것은 [이용허락규약\(Legal Code\)](#)을 이해하기 쉽게 요약한 것입니다.

[Disclaimer](#)

공학박사학위논문

**Flame Response Characteristics of
Non-premixed Flames on Acoustic Excitation**

**비에혼합화염의 음향 가진에 따른
화염응답특성**

2022년 2월

서울대학교 대학원

기계항공공학부

안 명 근

ABSTRACT

Although the cause and mechanism of combustion instability have not been elucidated yet, it is known that the presence or absence of combustion instability is determined by the interaction of reactant flow perturbation, heat release perturbation, and perturbation due to the acoustic boundary of the combustion chamber. When these three perturbations form a positive feedback loop, the probability of combustion instability increases, and when a negative feedback loop is formed, the probability decreases. Therefore, to reduce the appearance of combustion instability, it is essential to identify the conditions required for and the factors influencing combustion instability. In this study, the correlation between heat emission perturbation and velocity perturbation was investigated among the factors governing combustion instability. For pinch-off flames, a phenomenon in which flames are separated under specific acoustic excitation conditions, the mechanism of combustion instability was investigated by simultaneous OH-planar laser-induced fluorescence (PLIF) and particle image velocity (PIV) laser measurements. In addition, the nitrogen oxide (NO_x) emission and the flow characteristics were analyzed. OH* chemiluminescence and OH-PLIF laser measurements were used for flame structure analysis, and simultaneous OH-PLIF and PIV measurements were used for flow field characterization. A photomultiplier tube (PMT) was used to measure the heat release needed to calculate the flame transfer function (FTF). The flow boundary layer between the fuel and air was also analyzed.

To predict combustion instability, we conducted a comparative study of the response characteristics and dynamic characteristics of non-premixed and premixed flames generated by acoustic excitation. Two flames with different combustion reactions have different dynamic behavior characteristics, depending on acoustic excitation. Non-premixed flames show acoustically created waves projected from the flame surface, with a flapping dynamic behavior, and are flame-shaped with an open flame tip. On the other hand, the premixed flame from the single nozzle fluctuates vertically with a conical shape. For the non-premixed flame, the number of modulations on the flame surface

increases with increasing excitation frequency, but the flame structure does not change significantly. The flame transfer function analysis by measuring the heat release rate of both flames during acoustic excitation revealed that the non-premixed and premixed flames showed nonlinear and linear results, respectively. By introducing the flame height and the Strouhal number (St number), correlation analysis between heat release and flame structure was performed and the results were compared with those of numerical studies. For non-premixed flames, the nonlinearity was verified by the numerical analysis results in the velocity perturbation of 20% or more. The numerical analysis and the premixed flame results were consistent but showed a locally different tendency. For premixed flames, the Strouhal number calculation does not consider the flame surface curvature, flame propagation speed, and flame tip shape. A more accurate Strouhal number analysis will be possible if these factors are included in the analysis.

Various flame structure analyses were conducted in terms of the velocity perturbation intensity and the excitation frequency during acoustic excitation in a non-premixed flame. The non-premixed flame is one example of the Buck-Schumann flame (B-S flame). A pinch-off flame is defined as a phenomenon in which the flame is cut off; the flame attached to the nozzle is defined as the main flame, and the separated flame is defined as the pocket flame. It was confirmed that a pinch-off flame appears in a constant range of excitation frequencies and velocity perturbation intensities. Simultaneous OH PLIF and PIV measurements were performed to investigate the mechanism of the pinch-off flame. By mapping the flame structure in terms of excitation frequency and velocity perturbation intensity, it was classified into three dynamic behaviors. We observed a flickering flame with a large perturbation in the vertical direction in the low-frequency range, a pinch-off flame in the mid-frequency range, and a wrinkled flame with a modulated surface in the high-frequency range. The double dipole vortex caused by the tidal flow during acoustic excitation in the non-reactive field flow was confirmed by Mie scattering analysis. The inflow of air by the vortical structure was found to cause the flame deformation when the flame in the reaction field was pinched off, and a strong

strain rate was observed in the flame neck. Accordingly, it was confirmed that the pinch-off flame was an interaction between the inflow of external air by the vortical structure and the high strain rate.

NO_x and carbon monoxide (CO) emission characteristics were analyzed considering the pocket flame separated from the pinch-off flame. With increasing velocity perturbation intensity, the mixing intensity of the fuel and the oxidizer increases and thus, the amount of NO_x emitted decreases. With good mixing of the fuel and oxidizer and complete combustion, NO_x emissions are reduced. On the other hand, CO emissions increased with increasing velocity perturbation intensity, but it was confirmed that the emissions were very small. The height of the pinch-off flame was subdivided into the main flame and the pocket flame to analyze the two emission characteristics, viz. the emission index of NO_x (EINO_x) and the flame residence time. The subdivided flame height and flame residence time analysis showed the same trend of reducing NO_x emissions as the flame residence time decreased, but it did not follow the trend of the excitation frequency. Therefore, it was concluded that there is a limit to the analysis of NO_x emission characteristics when using only the flame residence time. The correlation analysis between Strouhal number and EINO_x confirmed that the EINO_x value was the same even though the Strouhal number was different. This means that the flame height is independent of the trend analysis whether the main flame or the pocket flame is selected. To verify this tendency, it was confirmed that EINO_x normalized by flame residence time followed 1/2-power well.

Strain rate and shear stress correlation analyses were performed under pinch-off and non-pinch-off conditions. The fuel and air velocities are the same, and by changing these, the shear stress was generated based on the condition of no theoretical shear stress. Simultaneous measurements of OH^* chemiluminescence and PIV was performed for boundary layer flow analysis of fuel and air velocity. The physical boundary was confirmed by performing pinch-off mapping for various fuels and air velocities. As the shear effect increased under the pinch-off condition with increasing fuel velocity, the strain rate increased by ~80% compared to the reference data, and the shear stress increased by 15%. Under the non-pinch-off condition, the

shear effect was further increased by further increasing the fuel velocity, but the strain rate was reduced by 50% compared to the previous data, and the shear stress was increased 3.3 times. The tendency was also verified by analyzing the correlation between strain rate and shear stress under non-pinch-off conditions with increasing air velocity. Shear stress tends to decrease when strain rate has a major influence, and the applicability of shear stress, as a parameter to control pinch-off, was confirmed

Keywords: Non-premixed flame, Pinch-off flame, Burke-Schumann flame, Premixed flame, Acoustic excitation, Combustion instability, Flame transfer function, Flame structure, OH-planar laser-induced fluorescence (OH-PLIF), OH* chemiluminescence, Particle image velocity (PIV), Laser simultaneous measurement, NO_x, EINO_x, Flame residence time, Strain rate, Shear stress.

Student Number: 2017-34984

LIST

ABSTRACT.....	i
LIST	v
LIST OF FIGURES	x
LIST OF TABLES	xv
NOMENCLATURE.....	xvi

CHAPTER 1

INTRODUCTION	1
1.1 Background.....	1
1.2 Combustion instability.....	4
1.3 Flame transfer function (FTF)	5
1.4 Acoustic excitation in non-premixed flame.....	7
1.5 Strain rate and local flame extinction in non-premixed flame.....	9
1.6 Motivation.....	10
1.7 Objectives.....	11
1.8 Outline.....	12

CHAPTER 2

EXPERIMENTAL AND MEASUREMENT SYSTEMS.....	13
2.1 Combustor and nozzles.....	13
2.2 Flame imaging.....	16
2.2.1. Chemiluminescence Spectroscopy.....	16
2.2.2. OH planar laser induced fluorescence (OH PLIF) measurement.....	19
2.2.3. OH PLIF system.....	22
2.2.4. High-speed OH PLIF system.....	23
2.2.5. Particle image velocimetry (PIV) measurement.....	26
2.2.6. Simultaneous measurement of PIV and OH PLIF system.....	30
2.3 Flame Transfer Function (FTF)	32
2.4 NO _x measurement system.....	34

CHAPTER 3

COMPARISON OF FLAME RESPONSE CHARACTERISTICS BETWEEN NON-PREMIXED FLAMES AND PREMIXED FLAMES OF UNDER ACOUSTIC EXCITATION.....	35
3.1 Objectives.....	35
3.2 Experimental setup and methodology.....	38
3.3 Flame appearance comparison between the non-premixed flame and the premixed flame.....	42

3.4 Flame dynamic characteristics under acoustic excitation of non-premixed flame.....	44
3.5 Flame dynamic characteristics under acoustic excitation of premixed flame.....	48
3.6 Comparison of the flame response characteristics between non-premixed and premixed flames.....	55

CHAPTER 4

PINCH-OFF PROCESS OF BURKE-SCHUMANN FLAME UNDER ACOUSTIC EXCITATION.....

4.1 Objectives	63
4.2 Experimental setup and methodology.....	66
4.3 Flame response characteristics under various excitation frequencies...	71
4.4 Flame response characteristics of pinch-off process at 80 Hz.....	73
4.5 Flame response characteristics at pinch-off boundary.....	76
4.6 Vortex-flame interaction and strain rate analysis for the pinch-off mechanism.....	79

CHAPTER 5

NOX EMISSION CHARACTERISTICS OF PINCH-OFF FLAME UNDER ACOUSTIC EXCITATION.....

5.1 Objectives.....	86
---------------------	----

5.2 Experimental setup and methodology.....	89
5.3 Global appearance characteristics of non-premixed flame under acoustic excitation.....	93
5.4 Effects of acoustic excitation on EINO _x and CO concentration.....	98
5.5 Effects of velocity perturbation intensity (u'/\bar{u}) and forcing frequency on main flame (F_M) and net hot product (F_N)	102
5.6 Effects of Strouhal number and forcing frequency on flame residence time (τ_{res})	104

CHAPTER 6

EFFECTS OF STRAIN RATE AND SHEAR STRESS ON STRUCTURE OF PINCH-OFF AND NONPINCH-OFF FLAMES.....

6.1 Objectives	108
6.2 Experimental setup and method.....	110
6.3 Flame response characteristics according to fuel and air bulk velocity.....	114
6.4 Characteristics of pinch-off flame with increasing fuel bulk velocity.....	117
6.5 Characteristics of non-pinch-off flame by increasing fuel bulk velocity.....	120
6.6 Characteristics of non-pinch-off flame with increasing air bulk velocity.....	123

CHAPTER 7

CONCLUSION.....	126
7.1 Conclusions.....	126
7.1 Limitation and future work.....	128
REFERENCES.....	129
ABSTRACT IN KOREAN.....	145

LIST OF FIGURES

Fig. 1.1	Twin-annular premixed swirler (TAPS) employing a premixed flame as the main flame and a non-premixed flame as the pilot flame; (a) GE's TAPS concept [1], (b) Schematic of the main and pilot flames [2].	2
Fig. 1.2	Concept of oscillating combustion. [3]	2
Fig. 1.3	Schematic of the flat multi-cluster injector and its main burner (Hitachi Research Laboratory); schematic of a (a) flat multi-cluster injector and (b) the flat main burner and a typical flame image obtained in preliminary experiments. [4]	3
Fig. 1.4	Schematic of the feedback loop for combustion instability [5].	5
Fig. 2.1	Combustors described in chapter 3: schematics of (a) the non-premixed flame combustor, (b) nozzle tip of the non-premixed flame, (c) the premixed flame combustor, and (d) nozzle tip of the premixed flame.	14
Fig. 2.2	Schematic of the non-premixed flame combustor described in chapters 4, 5, and 6.	15
Fig. 2.3	OH^* chemiluminescence measurement system used for flame visualization.	18
Fig. 2.4	Schematic of the energy transfer process. Relaxation processes of the emission of photons.	19
Fig. 2.5	OH excitation spectrum; In this study, $\text{Q}_1(6)$ was used for OH PLIF.	20
Fig. 2.6	OH fluorescence spectrum for $\text{Q}_1(6)$.	21
Fig. 2.7	Transmittance of the bandpass filter.	22
Fig. 2.8	OH PLIF laser measurement system for flame visualization.	24
Fig. 2.9	Example of the flame shape according to the intensifier gate value. (a) OH^* chemiluminescence image, obtained by setting the gate to 100 μs . (b) OH PLIF image, obtained by setting the gate to 1 μs .	25
Fig. 2.10	(a) Schematic of the PIV measurement system. (b) Time interval of PIV measurement.	26
Fig. 2.11	The dispersion of particles with different Stokes numbers: (a) Stokes streak lines; (b) Stokes number = 0.1; (c) Stokes number = 1; and (d) Stokes number = 10 [6].	27

Fig. 2.12	Schematic of a typical PIV system from LaVision Company.	28
Fig. 2.13	Schematic of the simultaneous measurement system of OH PLIF and PIV.	30
Fig. 2.14	OH PLIF laser measurement system for flame visualization.	30
Fig. 2.15	(a) 283-nm laser sheet thickness and width. (b) Grating (5 mm × 5 mm) mounted on the nozzle when calibrating the camera's field of view.	31
Fig. 2.16	Voltage regulation to match the magnitude and phase difference between the velocity perturbation of air and fuel.	32
Fig. 2.17	(a) Schematic of the non-premixed flame burner described in Chapter 3, (b) hot-wire anemometry used for acoustic excitation measurement, (c) loudspeaker used for flow perturbation, (d) PMT used for heat release rate measurement.	33
Fig. 2.18	TESTO 350 K measuring NO _x , CO, O ₂ , etc.	34
Fig. 3.1	(a) Schematic diagram of the non-premixed flame burner, (b) the nozzle tip and the flame shape, (c) schematic diagram of the premixed flame burner, (d) the nozzle tip, and the flame shape.	40
Fig. 3.2	Flame luminosity of burner equipped with confinement; (a) non-premixed flame shape according to the increase in fuel/air bulk velocity, (b) premixed flame shape according to the change in equivalence ratio, (c) bulk velocity = 0.8 m/s, (d) bulk velocity = 2.0 m/s and premixed flame (e) $\phi = 0.7$, (f) $\phi = 0.98$.	42
Fig. 3.3	As forcing frequency increases at $u'/\bar{u} = 20\%$, oscillation of the flame surface increases; (a) 80 Hz, (b) 200 Hz, (c) 280 Hz.	44
Fig. 3.4	OH* chemiluminescence images for u'/\bar{u} and phase in the non-premixed flame, (a) 60 Hz, (b) 80 Hz, (c) 240 Hz.	45
Fig. 3.5	Flame height of the non-premixed flame with various u'/\bar{u} (a) $u'/\bar{u}=10\%$, (b) $u'/\bar{u}=20\%$, (c) $u'/\bar{u}=30\%$.	46
Fig. 3.6	OH* chemiluminescence images of the premixed flame according to forcing frequency at $u'/\bar{u} = 20\%$ with 270° . (a) conical-stable flame at 0 Hz, (b) pointed-conical flame at 80 Hz, (c) plateau flame at 120 Hz, (d) plateau-necking flame at 160 Hz, (e) plateau flame at 200 Hz, (f) blunted-necking flame at 240 Hz, (g) plateau-necking flame at 280 Hz.	49
Fig. 3.7	OH* chemiluminescence images with various u'/\bar{u} and phase in the premixed flames, (a) 60 Hz, (b) 80 Hz, (c) 240 Hz.	50

Fig. 3.8	Flame height of the premixed flame with various u'/\bar{u} , (a) 10%, (b) 20%, (c) 30%.	51
Fig. 3.9	Flame deformation process according to flame tip and side shape. (a) 100 Hz at $u'/\bar{u} = 10\%$, (b) 120 Hz at $u'/\bar{u} = 10\%$, (c) 140 Hz at $u'/\bar{u} = 20\%$, (d) 280 Hz at $u'/\bar{u} = 20\%$.	52
Fig. 3.10	Flame structure of the non-premixed (NPX) and premixed flame (PX) through OH^* images, (a) without excitation, (b) excitation frequency at 160 Hz.	56
Fig. 3.11	Gain and phase of the flame transfer function; (a) the non-premixed flame, (b) the premixed flame.	57
Fig. 3.12	The correlation between the flame height perturbation and the forcing frequency, (a) the non-premixed flame, (b) the premixed flame.	59
Fig. 3.13	The gain of the flame transfer function as a function of Strouhal number, (a) non-premixed flame, (b) premixed flame.	61
Fig. 4.1	Schematic diagram of the experimental setup. (a) non-premixed flame combustor. (b) laser system for simultaneous OH-PLIF and PIV measurements.	66
Fig. 4.2	(a) Time sequence of simultaneous OH PLIF/PIV measurements at $f = 80$ Hz and $(u'/\bar{u}) = 50\%$. (b) Overlapping PIV image and OH PLIF image to verify their consistency, the vortical structure obtained by acoustic excitation, and the stoichiometric contour expected to be located on the “rich side” of the OH layer [7].	68
Fig. 4.3	(a) Mapping result of the pinch-off flame conditions and flame dynamic characteristics in terms of the forcing frequency and velocity perturbation intensity (u'/\bar{u}). (b) OH PLIF images at $(u'/\bar{u}) = 30\%$.	71
Fig. 4.4	Flame images from instantaneous OH PLIF measurement at various frequencies and $(u'/\bar{u}) = 30\%$.	72
Fig. 4.5	(a) Flame dynamic characteristics at various (u'/\bar{u}) values and forcing frequency of 80 Hz, which is in the pinch-off range. (b) Flame height at 80 Hz for different (u'/\bar{u}) values.	73
Fig. 4.6	Pinch-off process at 80 Hz and $(u'/\bar{u}) = 50\%$ and deformation of the pinch-off flame by acoustic excitation under four different phases of (a) 45° , (b) 135° , (c) 225° , and (d) 315° .	74
Fig. 4.7	Flame height measured at $(u'/\bar{u}) = 50\%$, showing the characteristic flame behavior at the boundary on both sides of the pinch-off flame region. Points (a)–(d) are within 10 Hz from the boundary.	76
Fig. 4.8	Flame dynamic behavior at the boundary of the pinch-off region in Fig. 4.7 at $(u'/\bar{u}) = 50\%$ and four frequencies: (a) a flickering flame at 30 Hz, (b) a pinch-off flame at 50 Hz, (c) a pinch-off flame at	77

130 Hz, and (d) a wrinkled flame at 150 Hz.

Fig. 4.9	St numbers calculated using the main flame height and the total flame height.	78
Fig. 4.10	Images of nonreacting flow measured by Mie scattering at 80 Hz and $(u'/\bar{u}) = 50\%$. Two pairs of vortices were created with different directions of rotation, and the reverse flow was confirmed.	79
Fig. 4.11	Pinch-off due to the interaction between the flame and vortex at 80 Hz and $(u'/\bar{u}) = 50\%$.	80
Fig. 4.12	Time-dependent data of pinch-off flame. Left: OH PLIF image & strain rate field, center: strain rate, right: axial velocity.	82
Fig. 4.13	Schematic flow patterns of pinch-off flame. Images (a) and (b) illustrate the cases of Fig. 4.11(e) and (f), respectively.	84
Fig. 5.1	(a) Schematic diagram of experimental setup used and (b) shape of fuel/air nozzle.	90
Fig. 5.2	(a) Defining flame height based on main flame and pocket flame of pinch-off flame. (b) Example of image showing net hot product (F_N) excluding space between main flame (F_M) and pocket flame (F_P).	92
Fig. 5.3	Averaged images of OH^* chemiluminescence at different frequencies and $u'/\bar{u} = 30\%$.	94
Fig. 5.4	Averaged flame images for different u'/\bar{u} values and forcing frequencies of: (a) 20, (b) 80, and (c) 280 Hz.	95
Fig. 5.5	Instantaneous flame images at 80 Hz and u'/\bar{u} values of (a) 10%, (b) 30%, and (c) 50%.	95
Fig. 5.6	Changes in height of main flame (F_M) with phase for u'/\bar{u} values of 10–50% and forcing frequency of 80 Hz.	96
Fig. 5.7	Changes in $EINO_x$ and CO concentration with forcing frequency for different u'/\bar{u} values: (a) $EINO_x$ and (b) CO concentration (at 15% O_2).	98
Fig. 5.8	Changes in instantaneous flame image with phase at $u'/\bar{u} = 30\%$ and frequencies of (a) 20, (b) 140, and (c) 260 Hz.	100
Fig. 5.9	Effects of velocity perturbation intensity (u'/\bar{u}) on flame heights (dotted line is flame height without acoustic excitation): (a) $u'/\bar{u} = 10\%$, (b) $u'/\bar{u} = 30\%$, and (c) $u'/\bar{u} = 50\%$.	103
Fig. 5.10	Effects of (a) forcing frequency and (b) Strouhal (St) number on flame residence time (τ_{res}) at various u'/\bar{u} values.	104
Fig. 5.11	Changes in $EINO_x$ with St: (a) $u'/\bar{u} = 10\%$, (b) $u'/\bar{u} = 30\%$, and (c) $u'/\bar{u} = 50\%$.	105
Fig. 5.12	Effect of St on $EINO_x$ normalized with respect to flame residence time (τ_{res}) as analyzed from viewpoints of F_M and F_N .	106

Fig. 6.1	(a) Schematic of the experimental setup; (b) Simultaneous measurement results for acoustic excitation at 80 Hz. Left: vortical structure of PIV raw image; right: OH* image.	112
Fig. 6.2	Pinch-off mapping of fuel (u_F) and air (u_A) bulk velocity at 80 Hz and $u'/\bar{u}=50\%$.	114
Fig. 6.3	OH* OH* images for Case 2 for various u_F at 80 Hz, $u'/\bar{u}=50\%$, when $u_A=1$ m/s constant.	115
Fig. 6.4	OH* images for Case 3 for various u_A at 80 Hz, $u'/\bar{u}=50\%$, when $u_A=1$ m/s constant.	116
Fig. 6.5	Instantaneous simultaneous measurement result of Case 2-1 at 80 Hz, $u'/\bar{u}=50\%$, from left-OH* image of pinch-off, strain rate, and shear stress.	117
Fig. 6.6	Strain rate and shear stress calculated along the yellow dashed line in Fig. 6.5.	118
Fig. 6.7	Instantaneous simultaneous measurement result of Case 2-2 at 80 Hz, $u'/\bar{u}=50\%$, from the left-OH* image of the nonpinch-off, strain rate, and shear stress.	120
Fig. 6.8	Strain rate and shear stress calculated along the yellow dashed line in Fig. 6.7.	121
Fig. 6.9	Instantaneous simultaneous measurement result of Case 3-1 at 80 Hz, $u'/\bar{u}=50\%$, from the left-OH* image of the nonpinch-off, strain rate, and shear stress.	123
Fig. 6.10	Strain rate and shear strength calculated along the yellow dashed line in Fig. 6.9.	124

LIST OF TABLES

Table 1.1	Thermal properties and fundamental combustion characteristics of NH_3 and hydrocarbon fuels. [8]	3
Table 2.1	Formation and destruction of OH radicals.	19
Table 2.2	Summary of high-speed PLIF application research.	23
Table 3.1	Experiment conditions.	41
Table 3.2	Premixed flame categorizes various flame structures caused by acoustic excitation into the shape of the flame side, flame tip, and flame height.	54
Table 4.1	Experimental conditions	69
Table 5.1	Experimental conditions	91
Table 6.1	Experimental conditions	113
Table 6.2	Various fuel (u_F) and air (u_A) bulk velocities	113
Table 6.3	Experimental conditions for analyzing the flame characteristics of pinch-off and non-pinch-off	113

NOMENCLATURE

Alphabet

Re	Reynolds number
d	diameter [mm]
f	frequency [Hz)
h	flame length [mm], [m]
u	bulk velocity [m/s]
u'	velocity perturbation
\bar{u}	average velocity
λ	acoustic amplitude
St	Strouhal number
μ	micro
s	second
u'/ \bar{u}	velocity perturbation intensity
Max.	maximum
Min.	minimum
EINO _x	NO _x emission index
MW	molecular weight

Subscripts

ω	angular frequency
φ	phase difference

Subscripts

c	conical
P	pocket flame
N	net hot product

M	main flame
F	flame
res	flame residence time
F	fuel
A	air

CHAPTER 1

INTRODUCTION

1.1 Background

At the beginning of combustion device development, the focus was on output and mechanical perfection. Most combustion systems adopt a non-premixed flame that is stable and relatively easy to handle. However, the soot problem has emerged, and various studies have been conducted to solve it. The side effects of industrial development have also started to emerge. In particular, as the risks of exhaust emissions like NO_x , CO, sulfur oxides (SO_x), and unburned hydrocarbons (UHC) during operation of the combustion system became known, regulations became more stringent. Many combustion systems have switched from a non-premixed flame to a premixed or partially premixed flame, and lean-burn was widely adopted from rich-burn to reduce exhaust emissions.

Lean-burn is a technology that operates a combustion system in a lean-air state. It has the effect of reducing NO_x emissions by lowering the flame temperature, but has a side effect of combustion instability. To reduce combustion instability and NO_x emissions, the General Electric (GE) Company is developing a twin annular premixing swirler (TAPS) combustor [1,2,9–11] for aviation (Fig. 1.1). In addition, technologies such as integrated gasification combined cycle (IGCC) [12,13], a next-generation eco-friendly coal-fired power plant technology, and oscillating combustion [3,10,14] used in industrial radiant tube burner systems, are proposed (Fig. 1.2).

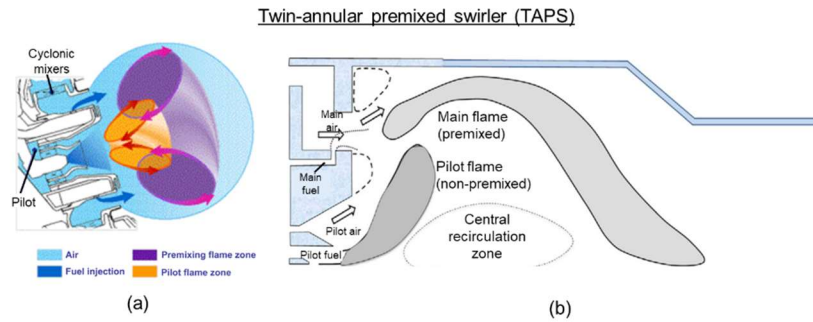


Fig. 1.1 Twin-annular premixed swirler (TAPS) employing a premixed flame as the main flame and a non-premixed flame as the pilot flame; (a) GE's TAPS concept [1], (b) Schematic of the main and pilot flames [2].

Recently, clean fuels (e.g. free-carbon, etc.) like hydrogen (H_2) and ammonia (NH_3) have been in the spotlight as part of energy transition policies [15–18]. In particular, the role of green hydrogen (H_2) produced by water electrolysis is drawing attention as a critical future energy source. Research and development of a micromixer combustor [4,19–21] that solves the flashback problem and reduces NO_x by lowering the overall temperature by distributing flame temperature, using only a clean fuel like H_2 are in progress (Fig. 1.3). In addition, reacting NH_3 , characterized by low heat dissipation per unit mass and high self-ignition temperature, with pulverized coal (Table 1.1), effectively reduces NO_x emissions [8].

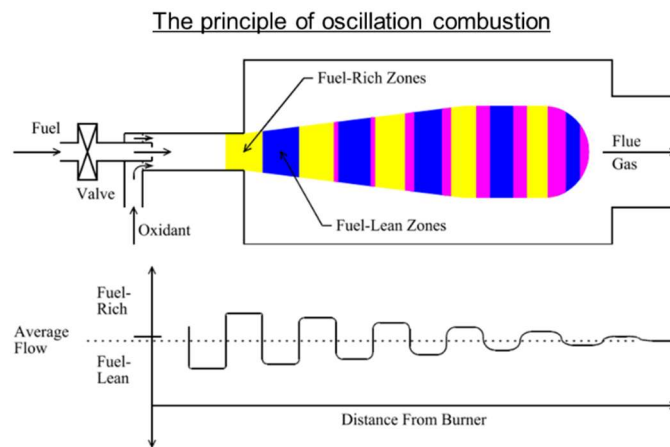


Fig. 1.2 Oscillating combustion concept [3].

Micromixer combustor at Hitachi Research Laboratory

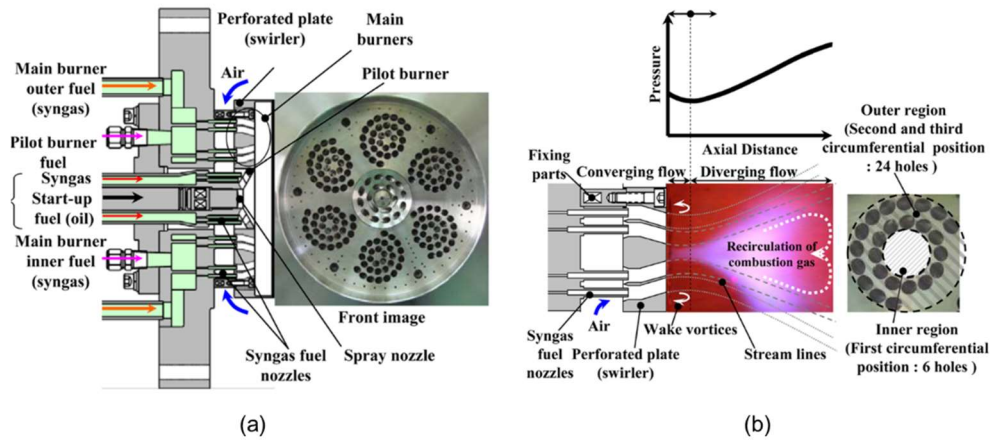


Fig. 1.3 Schematic of the flat multi-cluster injector and its main burner (Hitachi Research Laboratory); schematic of a (a) flat multi-cluster injector and (b) the flat main burner and a typical flame image obtained in preliminary experiments [4].

Table 1.1 Thermal properties and fundamental combustion characteristics of NH_3 and hydrocarbon fuels [8].

	NH_3	H_2	CH_4	C_3H_8
Boiling temperature at 1 atm [$^{\circ}\text{C}$]	-33.4	-253	-161	-42.1
Condensation pressure at 25°C [atm]	9.9	n/a	n/a	9.4
Lower heating value [MJ/kg]	18.6	120	50	46.4
Flammability limit [Equivalence ratio]	0.63~1.4	0.1~7.1	0.5~1.7	0.51~2.5
Adiabatic flame temperature [$^{\circ}\text{C}$]	1800	2110	1950	2000
Maximum laminar burning velocity [m/s]	0.07	2.91	0.37	0.43
Minimum auto ignition temperature [$^{\circ}\text{C}$]	650	520	630	450

Accordingly, research is conducted using H_2 , a clean fuel. The H_2/CH_4 fuel ratios used were 50/50 (Vol.%) and 75/25 (Vol.%), and the final goal was 100% H_2 combustion.

1.2 Combustion instability

Devices that utilize combustion have the risk of combustion instability. A device can be operated by avoiding the instability condition. Moreover, it is possible to install a damping apparatus by predicting instability conditions. Therefore, it is necessary to determine the condition of combustion instability or to install a damping apparatus for avoiding combustion instability. The precise mechanism of combustion instability has not yet been elucidated. Nonetheless, it is known that the presence or absence of combustion instability depends on the interaction among flow perturbation, perturbation of heat release, and perturbation under the acoustic boundary of the combustion chamber. If the above three perturbations form a positive feedback loop, the probability of combustion instability increases. On the other hand, if a negative feedback loop is formed, the probability of combustion instability decreases. Therefore, it is necessary to identify the type of feedback loop constituting the above three factors to understand the combustion instability.

1.3 Flame transfer function (FTF)

Examination of the feedback process of the three factors reveals the relationship between the flow perturbation and the heat release perturbation. Acoustic effects are then added to the result. For example, the relation between flow perturbation and heat release perturbation is expressed by the FTF or the flame description function. In addition, the sound transfer function or Helmholtz solver is used to add acoustic influence.

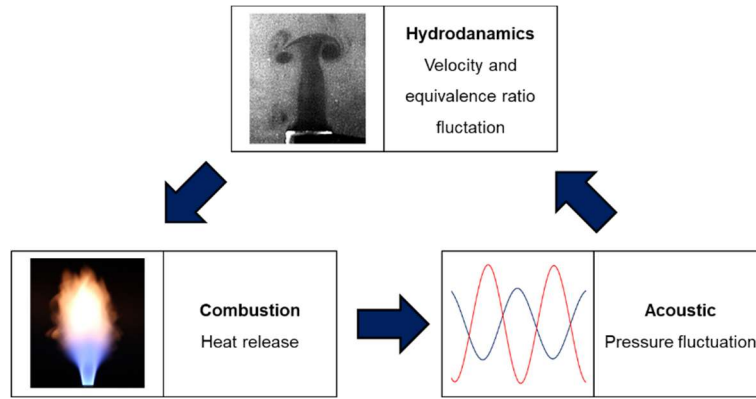


Fig. 1.4 Schematic of the (a) feedback loop for combustion instability [5].

The relationship between flow perturbation and heat release perturbation was evaluated by theoretical methods, computational fluid dynamics (CFD), and experimental methods. The FTF is shown in Eqn. (1-1) as a function that expresses the rate between the heat release perturbation and the velocity perturbation as a function of frequency. Here, the transfer function concept in control engineering is applied to the flame.

$$\text{Flame transfer function} = \frac{q'/\bar{q}}{u'/\bar{u}} = n(\omega)e^{i\theta(\omega)} \quad (1-1)$$

The FTF does not consider the absolute magnitude of the velocity perturbation. Instead, it considers the linear relationship between velocity perturbation and heat release perturbation. On the other hand, the flame description function shown in Eqn. (1-2), which considers the velocity perturbation an additional variable in the FTF, has been studied because of the nonlinear relation between velocity perturbation and heat release perturbation.

$$\text{Flame describing function} = \frac{q'/\bar{q}}{u'/\bar{u}} = n(u', \omega) e^{i\theta(n', \omega)} \quad (1-2)$$

The flame dynamics of premixed flames have been widely studied. For example, Ducrix et al. performed a theoretical and experimental study with acoustic forcing to measure the FTF and the flame surface of a conical flame [22]. Schuller et al. predicted the FTF of premixed laminar conical and V flames using the scalar value, i.e. G, to describe the flame front [23]. Durox et al. experimentally implemented an inverted conical flame, similar to a V flame, to show the FTF. The FTFs for various velocity perturbation magnitudes were obtained because the magnitude of the velocity perturbation influenced the magnitude of the FTF. This indicated that the relationship between the heat release oscillations and velocity perturbations is nonlinear [24]. Kim et al. studied the response to acoustic velocity and equivalence ratio oscillations for partial flames experimentally using the FTF [25]. Bellows et al. studied the FTF saturation mechanisms of a swirl stabilized combustor [26]. Polifke et al. studied the FTF low-frequency limit related to the conservation of mass, energy, and momentum [27]. Kim et al. measured the flame structure and FTF in a premixed model gas turbine combustor. They experimentally determined the relationship between the flame structure and the transfer function [28]. Palies et al. calculated the FTF by G equation modelling for a premixed flame with a swirl and compared it with the experimental results [29].

1.4 Acoustic excitation in non-premixed flame

Another characteristic of acoustic excitation is the enhanced mixing of fuel and air, which affects the pollutants formed during the combustion process. For example, Kim et al. [30] studied the relationship between the resonance frequency and the NO_x concentrations in a non-premixed flame. In all excited cases over a wide frequency range, they observed lower NO_x emissions than in the non-excited cases. In particular, a significant decrease in the NO_x concentrations was observed at the resonance frequency of the flame. These pollutant studies were conducted on laminar flames [31–34] as well as turbulent flames [35–37], considering the effects of increasing pressure [38–40]. The pinch-off flame tip is the main factor contributing to the generation of the pollutants [41], and the residence time of the pocket flame is longer than that of other normal flames. Since the soot growth time increases with increasing residence time of the flame, greater quantities of pollutants are emitted from the pocket flame [42]. Shaddix et al. [43,44] compared the soot volume fraction between a laminar steady non-premixed flame and a pinch-off flame, and found that soot production was four times greater in the latter. Furthermore, a qualitative agreement was verified with computational studies [44], and different sets of experimental results. Overall, soot growth occurs for a longer period in pinch-off flames than in steady flames, and soot production also increases due to the higher temperature maintained in the hot product.

Previously suggested mechanisms of pinch-off include local flame extinction [45,46], phenomena caused by vortex flow [47,48] and the inflow of air. Strawa et al. [45] examined the dynamic characteristics of a jet diffusion flame with increasing pressure during acoustic excitation at 9 Hz. The flame breakup phenomenon was measured by a schlieren technique, and the buoyancy-driven breakup process was followed near the nozzle outlet. In an analytical and numerical study of the flame response oscillation, Tyagi et al. [49] found that pinch-off occurs at a certain frequency and critical amplitude. Unfortunately, their study was limited to low frequencies (below 1 Hz), and a wider frequency range must be considered to identify pinch-off conditions (frequencies and amplitudes). Magina [42] reported that frequency and amplitude are the key parameters that control the pinch-off behavior and performed a theoretical analysis of pinch-off in terms of the axial diffusion effect. Considering cases with or without the axial diffusion effect, it was confirmed that axial diffusion causes pinch-off over a narrower Strouhal number range. Gao et al. [47] studied the

dynamic characteristics of flames excited at 100 Hz by simultaneous OH PLIF and PIV measurements. Pinch-off flames of various amplitudes were confirmed at 100 Hz, and the large vortex structure suggested local pinch-off. However, acoustic excitation was applied only to the fuel supply line, and the fuel jet was accelerated by the influence of the Kelvin-Helmholtz (K-H) instability [30].

1.5 Strain rate and local flame extinction in non-premixed flame

In non-premixed flames, the flame structure is affected by the strain rate [50], and it has been suggested that a higher strain rate changes the flame surface area and thus increases the chemical reaction rate. Acoustic excitation affects the flame length, flame shape, and local flame extinction [51] due to enhanced mixing in the flame, and these physical characteristics can be analyzed in terms of the strain rate. Carrier et al. [50] suggested that the strain rate affects the flame in two ways. First, a high strain rate causes an inflow of fresh air into the flame zone, such that the flame is first cooled and eventually quenched or extinguished. Secondly, a high strain rate extends the flame surface, which increases the area in contact with the flame front as well as the chemical reaction rate. Donbar et al. [52] analyzed the strain rate along the hydrocarbon (CH) reaction layer by simultaneous CH PLIF and PIV measurements in a turbulent non-premixed flame. Various trends were observed, such as large curvatures, cusps, near-extinction, expansion due to entrained air, and an increased flame area due to vortex rollup. Kim et al. [30] performed simultaneous OH PLIF and PIV measurements in turbulent non-premixed flames and observed local flame extinction due to an excessive strain rate in the high strain region. The authors suggest that two factors caused local flame extinction. The first is an increased diffusive influx of fuel by the internal vortex, and the second is air entrainment by the stretching motion of the external vortex. In previous studies [30,52], strain rate analysis was performed in terms of the flame contour derived from instantaneous data. However, the pinch-off behavior is a periodic phenomenon on a non-premixed flame; therefore, a time-resolved study is necessary to elucidate the mechanism. In this study, strain rate analysis was performed with time-course measurements.

1.6 Motivation

In combustion systems such as gas turbines for power generation, gas turbines for aviation, and boilers, the problem of combustion instability must be solved, and low NO_x emission technology is needed as required by stricter regulations in recent years. Research in aviation gas turbines is underway to develop a TAPS combustor to address this problem. The TAPS combustor aims at both stability and low NO_x emission by simultaneously utilizing a premixed flame as the main flame and a non-premixed flame as the pilot flame. The role of the pilot flame (non-premixed flame) in the TAPS combustor is flame stability. Paradoxically, the pilot flame, which is a major contributor to stability, also emits a significant amount of NO_x gases. Therefore, both combustion instability and NO_x emission reduction studies are needed for the pilot flame.

Oscillating combustion used in industrial radiant tube burner systems is a technology in which a constant temperature is maintained in the furnace and NO_x emissions are reduced. Oscillating combustion reduces NO_x by lowering the flame temperature via artificial flame extinction by forcibly controlling a wide range of flow rates from 10% to 90% using a control valve. The process of oscillating combustion is very similar to the pinch-off phenomenon of flame separation.

Based on the discussion above, the combustion system should satisfy both stability and NO_x emission reduction according to environmental regulations. Accordingly, in this study, flame stability and NO_x analysis are performed. Flame stability studies are conducted by flame structure analysis. For this purpose, OH* chemiluminescence, OH PLIF, and PIV measurements are performed. For NO_x emission characteristic analysis, correlation analysis with flame structure is performed using a gas analyzer. In this thesis, the research is conducted on two compositions, where the H₂/CH₄ volume ratios were 50/50 and 75/25. Although 100% H₂ combustion is the final goal, it is important to accumulate flame stability data at fuel composition ratios of 50/50 (v/v %) and 75/25 (v/v %) considering the fast flame propagation speed of H₂. Afterwards, a burner design suitable for 100% H₂ combustion must be designed.

1.7 Objectives

This study has four main objectives. First, the flame response characteristics of non-premixed and premixed flames were compared. In addition, the mechanism of pinch-off, which is a specific flame structure in a non-premixed flame, was experimentally investigated, and correlation analysis between the structure of the pinch-off flame and exhaust emissions (NO_x , CO) was performed. Finally, the role of the shear effect on pinch-off was also discussed.

Chapter 3 describes an introductory study of the TAPS combustor. As mentioned above, the TAPS combustor simultaneously utilizes the main flame and the pilot flame. The response characteristics of the main flame (premixed flame) and the pilot flame (non-premixed flame) were analyzed. The final goal was to study the interaction of the two flames and compare the individual flames. To this end, the burner geometry of premixed and non-premixed flames was designed similarly. The correlation between flame structure and heat-release rate for acoustic excitation was analyzed.

Chapter 4 describes the investigation of the external perturbation because the pilot flame of the TAPS combustor plays an important role in flame stability. Accordingly, analysis of the flame structure, when acoustically excited, was performed on a non-premixed flame. In this study, when fuel and air bulk velocities were equal to 1 m/s in the Burke-Schumann-based flame, mechanism analysis of the pinch-off flame, a specific flame structure, was performed under specific acoustic excitation conditions. For this purpose, simultaneous OH PLIF and PIV measurements were performed, and the process of pinch-off flame at a specific frequency and amplitude was analyzed. No shear effect was assumed because the fuel and the air bulk velocities are the same.

Chapter 5 describes the measurements of exhaust emissions (NO_x , CO) for various excitation frequencies and amplitudes under the same experimental conditions as in Chapter 4. For the correlation analysis between the flame structure and NO_x , the structure of the pinch-off flame was defined, and NO_x emission analysis was performed accordingly.

In chapter 6, the result of the effects of various fuel and air bulk velocities on pinch-off in the presence of shear effects are analyzed and is an extension of Chapter 4.

|

1.8 Outline

Chapter 2 summarizes the burners, measuring equipment, and measurement theory used in the study. Chapter 3 discusses the flame structure and response studies for acoustic excitation of non-premixed and premixed flames. Chapter 4 discusses the mechanism of pinch-off, a local flame extinction phenomenon, in terms of strain rate and vortical structure of the flow field. Chapter 5 defines the structure of a pinch-off flame and discusses NO_x emission characteristics and their correlation. Chapter 6 discusses the correlation between strain rate and shear effect in pinch-off and non-pinch-off. Conclusions and future work are discussed in Chapter 7.

CHAPTER 2

EXPERIMENTAL AND MEASUREMENT SYSTEMS

2.1 Combustor and nozzles

In this study, flame dynamic and response characteristics were analyzed using three types of combustors. Different aspects of the study are discussed in subsequent chapters with slight modifications to the experimental setup. Chapter 3 describes the use of the non-premixed flame and the premixed flame combustor and Chapters 4, 5, and 6 describe the use of the non-premixed flame combustor. The fuel nozzle diameters of the non-premixed flame combustors discussed in Chapters 3, 4, 5, and 6 are all 5 mm, but the geometries were different because the air nozzle diameters were different. However, both flames simulate the Burke-Schumann flame [53]. The premixed flame described in Chapter 3 has a conical structure.

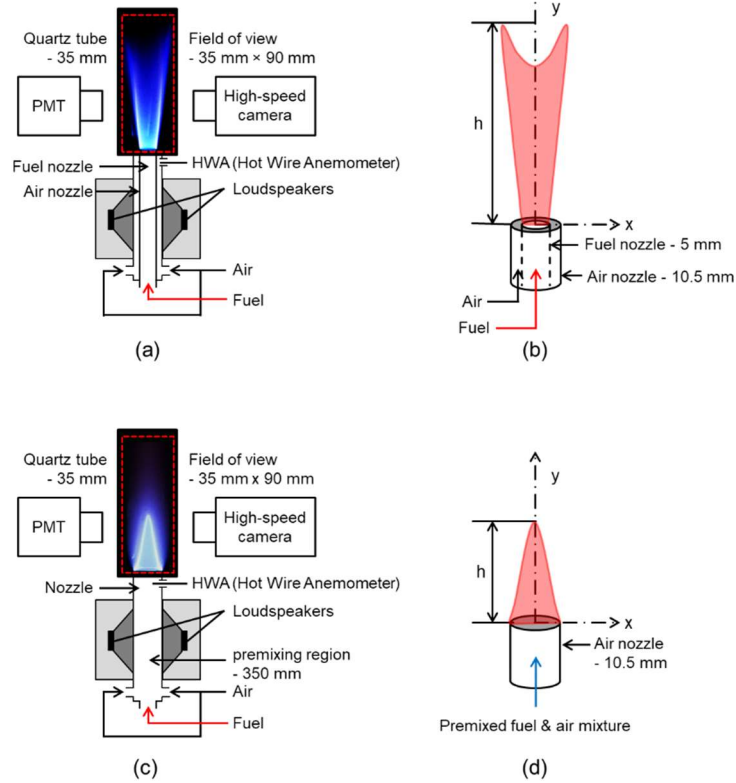


Fig. 2.1. Combustors described in chapter 3: schematics of (a) the non-premixed flame combustor, (b) nozzle tip of the non-premixed flame, (c) the premixed flame combustor, and (d) nozzle tip of the premixed flame.

Figs. 2.1 (a) and (b) show the construction of the combustor and nozzle tip used to analyze the characteristics of the flame response of the non-premixed flame according to the acoustic excitation described in Chapter 3. This system is a combustor of non-premixed flames where fuel and air are supplied separately, and confinement for blocking the inflow of external air was installed to observe the flame response of the supplied fuel/air. The field of view has dimensions of 35 mm \times 90 mm, and the hot wire anemometer (HWA) was mounted 30 mm below the air nozzle. Loudspeakers for flow perturbation were mounted on both sides of the combustor for acoustic excitation. A high-speed camera for measuring flame dynamic behavior according to the flame response of a photomultiplier tube (PMT) for heat-release rate measurement was installed on the side of the confinement. Fig. 2.1 (b) is a schematic showing the nozzle tip and flame structure of the non-premixed flame. The inner diameters of the fuel nozzle and air nozzle are 5 mm and 10.5 mm, respectively. The appearance of the non-premixed flame described in Chapter 3 is a case of the Burke-Schumann flame. Therefore, it is not in the form of a closed-flame tip like a general candle flame, but an opened-flame tip in which the flame tip is spread out.

Fig. 2.1 (c) and (d) show the combustor and nozzle tip used in the analysis of the flame response characteristics of the premixed flame according to the acoustic excitation described in Chapter 3. At the bottom of the combustor, fuel and air are supplied and first mixed in a collision effect. After that, the fuel/air mixture mixed downstream rises and is mixed secondarily. The fuel/air mixture reacts as a conical flame at the nozzle tip. This combustor has the same geometry as the combustor of the non-premixed flame (Fig. 2.1 (a)), but it becomes the premixed flame combustor when the fuel nozzle is removed. Therefore, the combustors can be of the non-premixed flame or premixed flame variety depending on the presence or absence, respectively, of a fuel nozzle. The loudspeaker perturbs the flow when the loudspeakers are mounted on both sides of the combustor. For the non-premixed flame, acoustic excitation was performed on the air nozzle with a higher flow than the fuel nozzle, and the entire flow of the premixed flame, composed of a single nozzle, is perturbed. Accordingly, the flame response behavior is different.

The response behaviors of the non-premixed and premixed flames appear differently

according to flame perturbation by acoustic excitation. For the non-premixed flames, waveform type modulation is projected onto the flame surface, and the number of modulations increases with increasing frequency. Since the entire single nozzle is acoustic excitation, various flame shapes are periodically repeated in the premixed flame. Details on this are covered in Chapter 3.

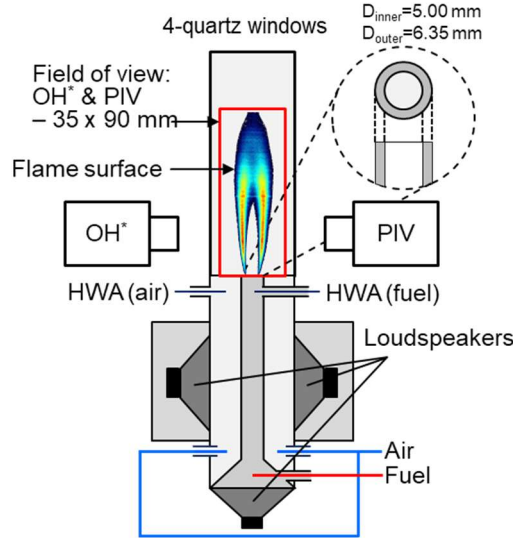


Fig. 2.2. Schematic of the non-premixed flame combustor described in chapters 4, 5, and 6.

Fig. 2.2 shows a schematic of the non-premixed flame combustor used to analyze the mechanism of pinch-off flame and NO_x emissions according to acoustic excitation in described in chapters 4, 5, and 6. This combustor was manufactured for experimental verification [54,55] of analytic research data [56]. Flame response according to acoustic excitation was compared with analytical and experimental data. In this study, the flame cutting phenomenon reported by Kim et al. [54] was defined as a pinch-off flame, i.e. a pocket flame separated from the main flame attached to the nozzle tip. Accordingly, the mechanism of pinch-off flame was analyzed through simultaneous measurement of OH PLIF and PIV. The loudspeakers were equipped with a fuel nozzle and an air nozzle for acoustic excitation of the air and fuel flow. HWA for acquiring acoustic signal data is installed in each flow line and installed at the bottom, 30 mm from the nozzle tip. To measure the flame appearance, OH^* chemiluminescence and OH PLIF measurements were performed, and the field of view was 35 mm \times 90 mm.

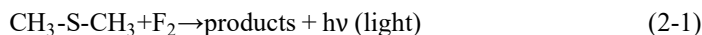
2.2 Flame imaging

In this study, OH^{*} chemiluminescence and OH PLIF measurements were performed to measure the flame structure of non-premixed and premixed flames. OH radicals are widely used as a flame marker. However, OH cannot be indicated directly because OH is distributed over a wide range of the reaction zone and the high-temperature product. Therefore, approximation by stoichiometric contour is required to use OH radical as a flame marker. Steinberg et al. [57] approximated the flame front by using the OH fluorescence signal in the premixed flame. Kaiser et al. [7] confirmed that the stoichiometric contour was located on the rich side of the OH PLIF image. Using the maximum temperature and the peak of the OH PLIF signal by Raman/Rayleigh point measurement in the turbulent non-premixed flame, the flame surface was defined. Accordingly, after acquiring the OH PLIF image, the logic of the previous study was applied to define the flame surface. The definition of the flame surface will be covered in detail later.

2.2.1. Chemiluminescence Spectroscopy

Similar to atomic emission spectroscopy (AES), chemiluminescence uses quantitative optical emission measurements of excited chemical species to determine analyte concentrations; however, unlike AES, chemiluminescence usually involves emission from energized molecules instead of simply excited atoms. The bands of light obtained by this technique emanate from molecular emissions and are therefore broader and more complex than bands originating from atomic spectra. Furthermore, chemiluminescence can occur in either the solution or gas phase, whereas AES is almost strictly a gas-phase phenomenon. Like fluorescence spectroscopy, the strength of chemiluminescence lies in detecting electromagnetic radiation produced in a system with a very low background. The energy necessary to excite the analytes to higher electronic, vibrational, and rotational states does not come from an external light source like a laser or a lamp; therefore, the problem of excitation source scattering is avoided. The major limitation to the detection limits achievable by chemiluminescence involves the dark current of the PMT necessary to detect the analyte light emissions. If the excitation energy for analytes in chemiluminescence does not come from a source lamp or laser, where does it come from? The excitation energy for the analytes

in chemiluminescence is produced by a chemical reaction. An example of this type of reaction is shown below:



In gas-phase chemiluminescence, the light emission (represented as $h\nu$) is produced by the reaction of an analyte (dimethyl sulfide in the above example) and a strongly oxidizing reagent gas such as fluorine (in the example above) or ozone, for instance. The reaction occurs on a time scale such that the production of light is essentially instantaneous; therefore, most analytical systems mix the analyte and the reagent in a small volume chamber directly in front of a PMT. If the analytes are eluted from a gas chromatographic column, then the end of the column is often fed directly into the reaction chamber. Since as much of the energy released by the reaction should be used to excite as many of the analyte molecules as possible, loss of energy via gas-phase collisions is undesirable. Therefore, a final consideration is that the gas pressure in the reaction chamber is maintained at low pressure (~ 1 torr) by a vacuum pump to minimize the effects of collisional deactivation. The ambiguous specification of "products" in the above-mentioned reaction is often necessary because of the nature and complexity of the reaction. In some reactions, the chemiluminescent emitters are relatively well known. The major emitter is electronically and vibrationally excited HF; however, other emitters have been determined whose identities are unknown. These also contribute to the total light detected by the PMT. To the analytical chemist, the ambiguity about the actual products in the reaction is, in this case, not important. The analyst is mainly concerned with the sensitivity (limit of detection) of the instrument, its selectivity (response for an analyte as compared to an interfering compound), and the linear range of response. As described in Chapters 3, 5, and 6, OH* chemiluminescence measurements were conducted to obtain the reaction region. Finally, we could obtain the flame heights based on the OH radical by using a high-speed camera rather than the visible flame height based on the visible mixed emissions by a standard DSLR camera.

Fig. 2.3 shows the OH* chemiluminescence measurement system used in this study. A high-speed camera (LaVision, Highspeedstar 8, maximum resolution 1024×1024 @ 7 kHz) with a Nikon UV 100-mm f/2.8 lens and an OH bandpass filter (LaVision, VZ-image Filter LIF for OH, enhanced, 310 ± 25 nm), an intensifier (LaVision, Highspeed IRO) that amplifies

the OH signal with an intensifier gate of 100 μ s were used to exclude the OH* chemiluminescence signal.

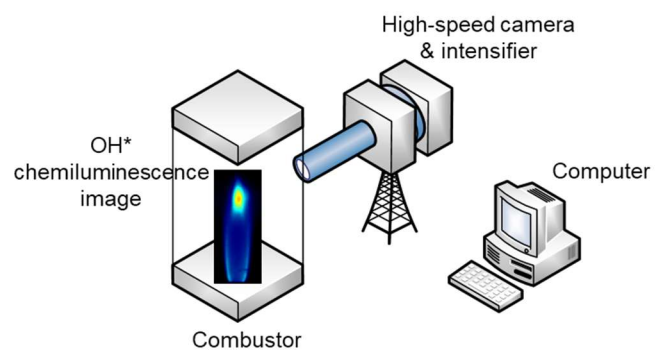


Fig. 2.3 OH* chemiluminescence measurement system used for flame visualization.

2.2.2. OH planar laser induced fluorescence (OH PLIF) measurement

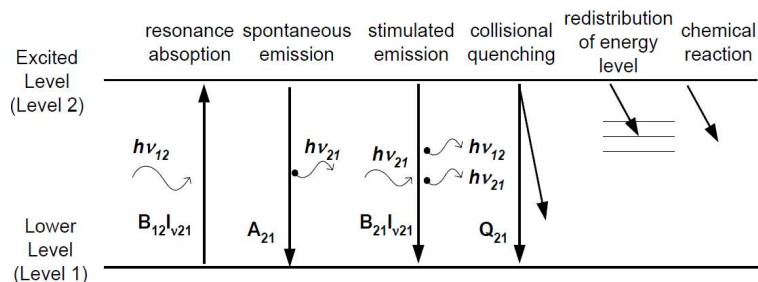


Fig. 2.4 Schematic of the energy transfer process. Relaxation processes of the emission of photons

Laser-induced fluorescence (LIF) is described as the absorption of a photon by a radical, followed by photon emission as the molecules transition from a higher energy state to a lower one. Fig. 2.4 shows the schematic of the energy transfer process. Some of the molecules will relax to the initial state by photoemission. Several relaxation processes are possible, including (a) spontaneous emission, (b) stimulated emission by exterior stimulus, (c) quenching by collision of molecules, (d) redistribution of energy level, and (e) change of molecular component by chemical reaction. However, the rapid or spontaneous emissions of photons are termed LIF. The frequency of the LIF signal can have a different value from that of the inducing laser beam.

Table. 2.1 Formation and destruction of OH radicals.

Fast OH formation by two-body reactions (1-5 ns)	
$\text{H} + \text{O}_2 \leftrightarrow \text{OH} + \text{O}$	
$\text{O} + \text{H}_2 \leftrightarrow \text{OH} + \text{H}$	
$\text{H} + \text{HO}_2 \leftrightarrow \text{OH} + \text{OH}$	
Slow destruction by three-body recombination reactions (-20 μs)	
$\text{H} + \text{OH} + \text{M} \leftrightarrow \text{H}_2\text{O} + \text{M}$	

OH PLIF measurement was used to obtain spatially and temporally resolved images of the reaction zone in various combustors. As described in Table 2.1, the OH radical concentration around the flame increases rapidly (in about 20 μs) and then decomposes slowly (in 1–5 ms)

by a three-body recombination reaction [58]. Thus, near the flame front exists super-equilibrium OH. The OH radical, an intermediate product of the chemical reaction, has a concentration more than ten times that of O or H radicals [59]. Therefore, when absorbing laser light, the OH radical emits a more intensive fluorescence signal than other species. Hence, the fluorescence signal of OH radical is widely used as an indicator of the flame front in reacting flows.

To observe the line positions for transition, we scanned the dye laser and recorded the signal at each step. We intended to use $Q_1(6)$ transition of the $A^2\Sigma^+ \leftarrow X^2\Pi$ ($v' = 1, v'' = 1$) band ($\lambda = 282.94$ nm) for the excitation wavelength and to collect the fluorescence signal from the A-X (1, 0) and (0, 0) bands ($\lambda = 306\text{--}320$ nm). Using a monochromator and PMT, in conjunction with a test flame under a laminar premixed condition, a laser excitation scan was performed over the wavelength range of interest (from $\lambda = 282.5$ nm to $\lambda = 283.5$ nm, with a step size of 0.001 nm). The monochromator was fixed at 315 nm to collect the fluorescence. The signal was multiplied by PMT and recorded through the boxcar averager. At every scanning step, ten pulses of the signal were recorded and averaged. After scanning the dye laser, the OH excitation spectrum can be obtained, as shown in Fig 2.5. Among the peak values of the excitation spectrum, we used $Q_1(6)$ as the excitation wavelength of the OH radical.

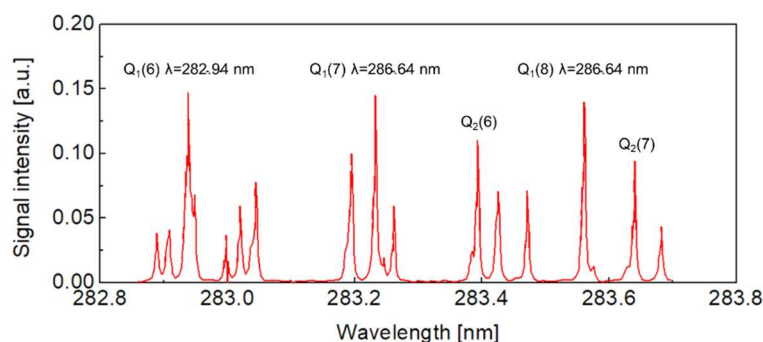


Fig. 2.5 An OH excitation spectrum. In this study, $Q_1(6)$ was used for OH PLIF.

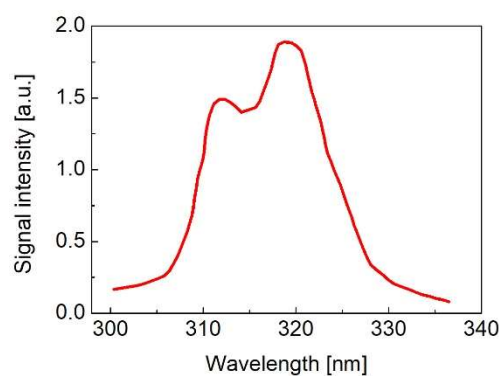


Fig. 2.6 An OH fluorescence spectrum for $Q_1(6)$.

When the $Q_1(6)$ line was detected, the fluorescence spectrum could be obtained by recording the LIF signal at each scanning step of the monochromator. Fig. 2.6 shows an OH fluorescence spectrum for $Q_1(6)$, with the maximum signal intensity found at 320 nm.

2.2.3. OH PLIF system

For OH PLIF, an Nd:YAG pumped dye laser was tuned to Q1(6) transition of the $A2\Sigma^+X2$ ($v' = 1, v'' = 1$) band ($\lambda = 282.94$ nm). The Q1(6) transition line is generally used to measure molecular concentration because it has a strong LIF signal, and the temperature dependency is low. Fluorescence from the A-X (1, 0) and (0, 0) bands ($\lambda = 306\text{--}320$ nm) were collected with a 100-mm/f 2.8 objective UV lens. Because UV light cannot penetrate the common glass, all the lenses should be made from quartz. The region of interest was focused on the intensifier and captured by a CMOS camera of LaVision. Advanced bandpass filters (LaVision, VZ-image Filter LIF for OH, enhanced, 310 ± 25 nm) was used to block scattered signal lights. The transmittance of the filter is shown in Fig. 2.7.

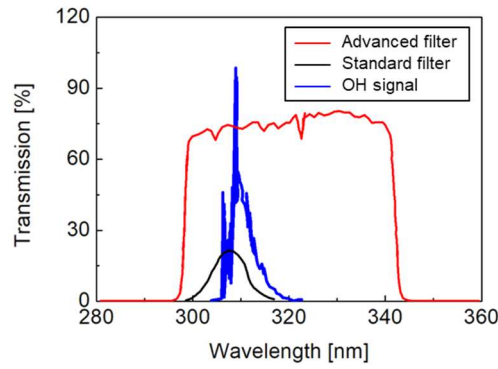


Fig. 2.7 Transmittance of the bandpass filter.

2.2.4. High-speed OH PLIF system

High-speed laser measurement is widely applied in various research fields to find the unknown characteristics of high-frequency phenomena. Many research groups have conducted experimental studies on CH₄/air flames, liquid fuel flames, and the microstructure of the flame. The detailed information about the research is summarized in Table 2.2.

Table. 2.2 Summary of high-speed PLIF application research.

Research group	Year	Author	Contents	Rep. rata
Lund university	2012	P. Petersson	Simultaneous high-speed PIV and OH PLIF measurements [60]	4 kHz
Lund university	2017	Z. Li	Simultaneous burst imaging of dual species [61]	50 kHz
University of Michigan	2009	A.M. Steinberg	Straining and wrinkling process[62]	3 kHz
University of Toronto	2013	A.M. Steinberg	Vortex structure and dynamics in swirl-stabilized combustion [63]	10 kHz
University of Toronto	2015	A.M. Steinberg	Transport of principal strain rates in turbulent premixed flames [64]	10 kHz
Shanghai Jiao Tong University	2019	Y. Gao	Acoustically forced in non-premixed flame [65]	20 kHz
Shanghai Jiao Tong University	2019	Y. Gao	Premixed swirling flame [66]	20 kHz
University of Iowa	2019	J. Zhang	Thermoacoustic instability of hydrogen-methane/air premixed flames [67]	20 kHz
German Aerospace Center (DLR)	2017	M. Severin	High momentum jet flames at elevated pressure [68]	10 kHz
German Aerospace Center (DLR)	2019	W. Meier	Auto-ignition [69]	10 kHz

The OH radical image was obtained using an Nd:YAG laser (Edgewave IS-200-2-L, 532 nm; 11.71 mJ/pulse at 7 kHz) and a dye laser (Sirah, Credo-Dye-LG-24), as described in

Chapter 4. Rhodamine 6G was used as the dye for wavelength tuning (283 nm; 0.4 mJ/pulse at 7 kHz), and a high-speed camera (Highspeedstar 8, maximum resolution 1024×1024 @7 kHz) was used for recording. The OH intensity was increased using an intensifier (Highspeed IRO). The laser was tuned to the $Q_1(6)$ transition of the OH radical near $\lambda = 282.94$ nm. A Nikon UV 100 mm f/2.8 lens and an OH PLIF bandpass filter (LaVision, VZ-image Filter LIF for OH, enhanced, 310 ± 25 nm) were used. The light with a wavelength of 532 nm from a Nd-YAG pump laser was adjusted to 283 nm by passing it through the frequency doubler and a Rhodamine 6G dye cell inside the dye laser. To measure the OH PLIF, it was necessary to monitor OH radicals in the excited state. However, OH* chemiluminescence will also be recorded if the exposure time is too long. An intensifier gate of 1 μ s was used to exclude the OH* chemiluminescence signal and acquire only the OH fluorescence.

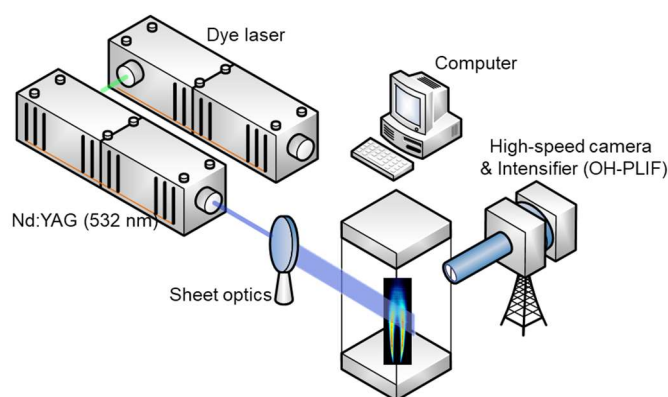


Fig. 2.8 OH PLIF laser measurement system for flame visualization.

Figure 2.9 shows the difference between an OH* chemiluminescence image (a) and an OH PLIF image (b). The gate value of 1 μ s was used in this study. If the gate value of the intensifier is large, the OH* chemiluminescence and OH PLIF signals are measured together. Therefore, when the intensifier gate is exposed for an appropriate amount of time (1 μ s), the OH* chemiluminescence signal can be minimized, and only the OH PLIF signal can be obtained. In addition, the following image shows the difference in flame shape measured by the OH PLIF and OH* chemiluminescence studies in terms of the gate value.

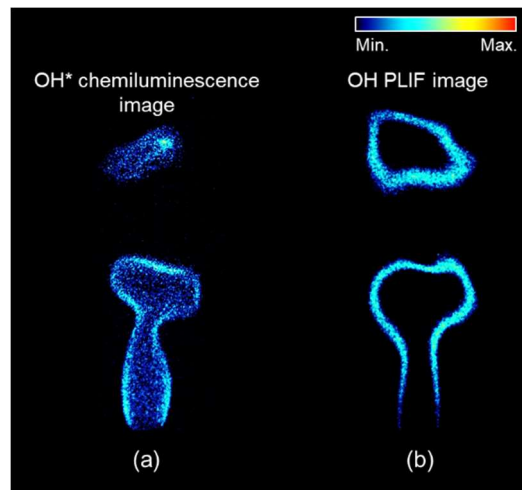


Fig. 2.9 Example of the flame shape according to the intensifier gate value. (a) OH^* chemiluminescence image, obtained by setting the gate to $100\ \mu\text{s}$. (b) OH PLIF image, obtained by setting the gate to $1\ \mu\text{s}$.

2.2.5. Particle image velocimetry (PIV) measurement

The velocity vector fields of a steady-state flow can be obtained using PIV by comparing consecutive images. The experimental setup of the PIV system consists of several subsystems: a double-pulse light source system, a detecting system, and a particle seeding system, as shown in Fig. 2.10 (a). PIV measures the velocity of the particles, instead of the flow itself, by comparing the displacement of each particle image illuminated by the sequential light pulses; therefore, small particles should be seeded in the flow to conduct the PIV measurement.

Fig. 2.10 (a) shows the PIV measurement system used in this study. Velocity field, strain rate, and vorticity were calculated in non-reacting and reacting fields according to acoustic excitation using a 527-nm Nd:YLF laser system. Particles were seeded in the fuel line and airline, and the diameter of the seeding particle was 1 μm . The PIV time interval is 200 μs , as shown in Fig. 2.10 (b).

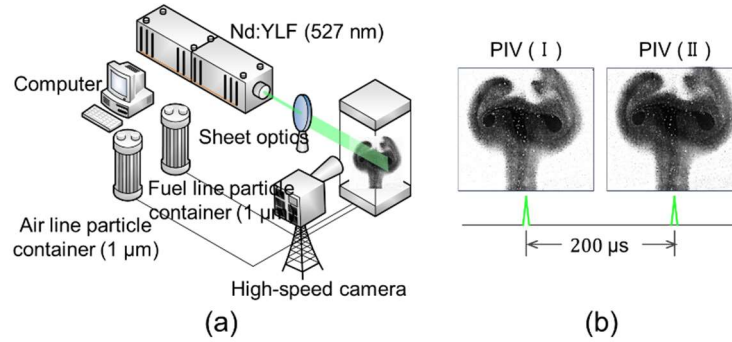


Fig. 2.10 (a) Schematic of the PIV measurement system.
(b) Time interval of PIV measurement.

The size of the particle was considered a Stokes number. The Stokes number is the ratio of the particle's momentum response time to the flow-field time scale:

$$\text{Stokes number} = \frac{\rho_p D_p^2 / 18\mu}{D_0 / U_0} \quad (2-2)$$

By definition, a larger Stokes number represents a larger or heavier particle, and a smaller or

lighter particle has a smaller Stokes number.

- (1) For Stokes number $\ll 1$, the particles will mostly follow the fluid motion acting as a tracer;
- (2) For Stokes number ≈ 1 , the particles centrifuge out of the vortex cores and concentrate on the vortex peripheries; and
- (3) For Stokes number $\gg 1$, the carrier fluid has limited influence on particle motion.

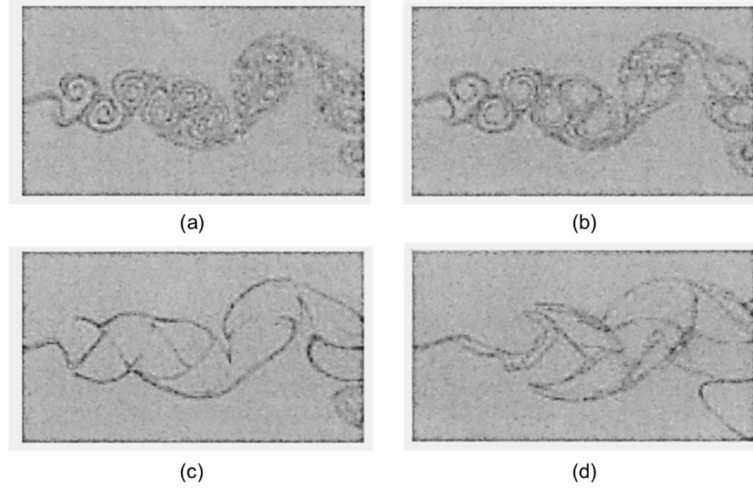


Fig. 2.11 The dispersion of particles with different Stokes numbers: (a) Stokes streak lines; (b) Stokes number = 0.1; (c) Stokes number = 1; and (d) Stokes number = 10 [6].

In this study, a double-pulse neodymium-doped yttrium lithium fluoride (Nd:YLF) laser is used as a light source, and a high-speed CMOS camera is employed to obtain instantaneous particle images at a measurement plane. There are no specific rules for particle seeding systems; however, the size of the particle should be determined by considering whether particles can follow the flow well or not [70]. It is necessary to add tracer particles into the flow in most cases. These particles are illuminated at the measurement plane of the flow twice within a short interval. The scattering or fluorescence signals from particles are recorded on single or sequential frames. The displacement of the particle signals identified by the light pulses is calculated using the evaluation of the PIV.

To calculate the displacement of the particles captured by the CMOS camera, the image must be divided into several grids called interrogation windows. After setting the size of the

interrogation window, one interrogation window of the first images is picked and compared with all the interrogation windows of the second images. The displacement between the interrogation window of the first image and the interrogation window of the second image represents one flow field vector. By conducting this study in all the interrogation windows, whole vectors of flow-field can be obtained. This process is called a correlation.

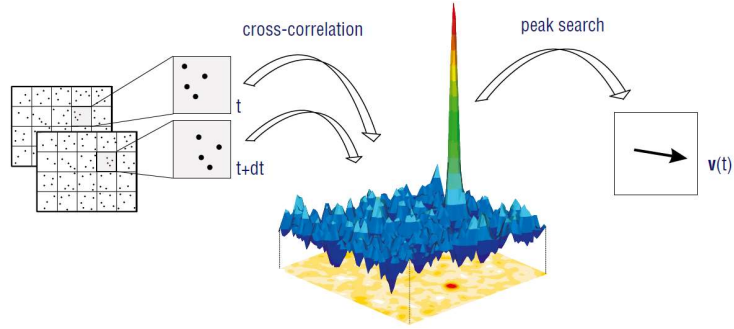


Fig. 2.12 Schematic of a typical PIV system from LaVision Company.

The correlation function is expressed as follows:

$$h(s_x, s_y) = \int_0^\infty \int_0^\infty f(x, y) g(x + s_x, y + s_y) dx dy \quad (2-3)$$

The expression can be simplified by Fourier transformation.

$$F(h) = F^*(f) \times F(g) = F^* \times G \quad (2-4)$$

F and G are Fourier-transformed functions of f and g.

$$h = F^{-1}(F^* \times G) \quad (2-5)$$

Equation (2-3) is the same expression of spatial masking in an image processing technique. Thus, it means that a correlation is a kind of masking concept. According to this concept, correlation is a process to determine the distribution of the similarity by signal distribution in an image plane. Equation (2-5) uses the fast Fourier transform (FFT) algorithm, drastically

reducing the calculation time. An interrogation window of size $2 \times 2 n^2$ should be used because the FFT algorithm is a method that divides even and odd terms. However, the calculation time becomes shorter by $\log_2 N/N$ times compared with the direct Fourier transform (DFT) algorithm.

A correlation method is classified into auto-correlation and cross-correlation. Mathematically, autocorrelation is the case where $f(x; y) = g(x; y)$, as in Eq. (2-4), and cross-correlation is the case where $f(x; y) \neq g(x; y)$. Experimentally, auto-correlation is used for the case where the first image at $t = t_1$ and the second image at $t = t_2$ are recorded in one frame (called a single frame/double exposure mode), and cross-correlation is used for the case where the first image at $t = t_1$ and the second image at $t = t_2$ are recorded in separate frames (called a double frame/single exposure mode). Compared with an auto-correlation method, a cross-correlation method has the following merits:

1. Directional ambiguity problems can be avoided easily.
2. The algorithm is simple because there is only one peak resulting from correlation.
3. The dynamic range is relatively large.

However, satisfying hardware requirements for cross-correlation was challenging. Especially, a time interval was a problem because the device, which satisfied both high-resolution conditions and short time intervals (microsecond), was costly. Nowadays, it has become relatively inexpensive and popular. Thus, most PIV systems use a cross-correlation method.

In this study, the PIV system was used Mie scattering in chapter 4. The setup for flow-field analysis consisted of a Nd:YLF laser (Photonics Industries DM, 527 nm; 2.7 mJ/pulse @3.5 kHz), a high-speed camera (Highspeedstar 8, maximum resolution 1024×1024 @7 kHz), a NIKKOR AF MICRO 105 mm f/2.8 lens, and a 527-nm bandpass filter (LaVision, VZ-image Filter 527 ± 10 nm). The resolution of the PIV image was 1.11×10^{-1} mm/pixel. Particles of zirconium oxide (ZrO_2 , 1 μm diameter, 99.5% on metals basis excluding Hf, Hf <100 ppm) were used in the air and fuel line containers.

2.2.6. Simultaneous measurement of PIV and OH PLIF system

In Chapter 4 of this study, the mechanism of the pinch-off flame is elucidated based on flame structure and velocity field analysis using simultaneous PIV and OH PLIF measurements. The simultaneous measurement system is shown in Fig. 2.13. The simultaneous laser beam of OH PLIF and PIV was irradiated with the test section using a dichroic mirror that reflected 283-nm light and allowed 527-nm to pass through. The irradiated laser beams are acquired by using high-speed cameras located on both sides of the combustor. The angle between the laser beam and the camera is 90° .

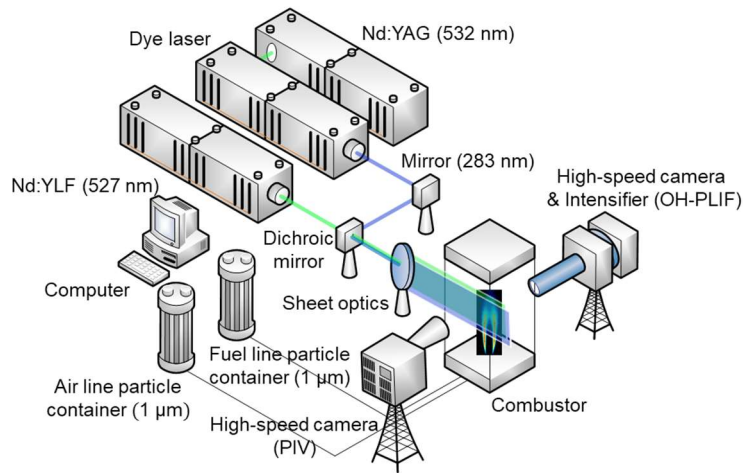


Fig. 2.13. Schematic of the simultaneous measurement system of OH PLIF and PIV.

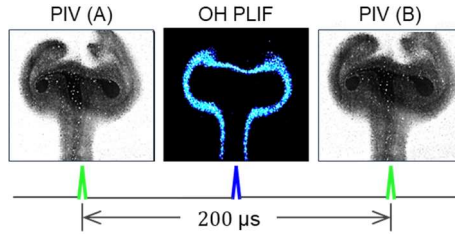


Fig. 2.14 OH PLIF laser measurement system for flame visualization.

Fig. 2.14 shows the laser sequence and simultaneous measurements from the OH PLIF and PIV laser systems. PIV images A and B, which were obtained using a dual pulsed laser, have a time interval of $200 \mu\text{s}$, and the laser shot for OH PLIF measurement was irradiated between

the two PIV shots.

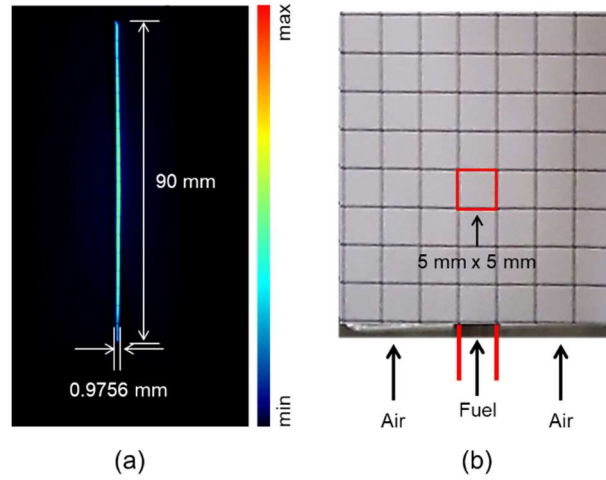


Fig. 2.15 (a) 283-nm laser sheet thickness and width.

(b) Grating ($5\text{ mm} \times 5\text{ mm}$) mounted on the nozzle when calibrating the camera's field of view.

The OH PLIF laser thickness are shown in Fig. 2.15 (a). The thickness of the laser beam is 0.9756 mm and based on sheet optics, it can be controlled manually to the minimum value by trial and error. Fig. 2.15 (b) is a grating panel with each grid of dimensions $5\text{ mm} \times 5\text{ mm}$ to calibrate the field of view of both cameras. Since the focal length of the lens used for simultaneous measurement is different, the distance at which the camera is to be positioned is also different. Therefore, it is necessary to calibrate the field of view (Fig. 2.15 (b)) to appear as an object of the same size at different locations. For calibration, after mounting the grating panel (Fig. 2.15 (b)) on the nozzle tip, the focal length of each lens was calculated to determine the distance between the grating panel and the sensors of the cameras.

2.3 Flame Transfer Function (FTF)

The FTF represents the heat-release rate, which is the dynamic response of the flame fluctuation by flow perturbation. It is defined as the ratio of heat release rate and velocity fluctuation rate and is expressed in expression (2-6) below:

$$F(\omega) = \frac{q'/Q_0}{u'/U_0} = G(\omega)e^{i\phi(\omega)} \quad (2-6)$$

$G(\omega)$ in equation (2-6) is the gain of the FTF and represents the response intensity, $\phi(\omega)$ is the phase difference, and the real part is the natural frequency. The imaginary part is the growth rate of the initial instability factor, which is amplified when it is negative.

The velocity is measured using an HWA located at the exact position of the air and fuel supply lines. The heat release is measured using the PMT with a bandpass filter (LaVision, VZ-image Filter LIF for OH, enhanced, 310 ± 25 nm), allowing the OH radical to pass through. Heat release measurements were performed by a Hamamatsu PMT with WG305 and UG11 filters to measure the intensity of the OH* chemiluminescence. The velocity perturbation was measured by the MiniCTA of Dantec Dynamics on the fuel and air nozzles. The voltage measurement for the velocity and heat release signal was performed using a National Instruments CompactDAQ. The device for applying a voltage to the loudspeaker was a function generator from Yokogawa (FG420). The velocity and heat release rate are measured simultaneously using a data acquisition board with a sampling rate of 10 kHz.

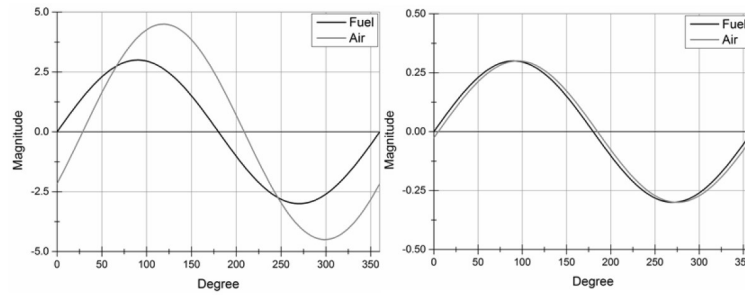


Fig. 2.16 Voltage regulation to match the magnitude and phase difference between the velocity perturbation of air and fuel.

Loudspeakers were used to generate velocity perturbations in air and fuel. Two loudspeakers were installed on the left- and the right-hand sides of the air pipe, and one loudspeaker was attached to the bottom of the fuel pipe. To simulate the Burke–Schumann flame [53] structure, the velocity and air velocity fluctuations of the air and fuel had to be equal in magnitude and phase. Thus, the trial-and-error method was used to control the voltage applied to the loudspeakers. The magnitude and phase difference between air and fuel velocity perturbation via this voltage regulation were lower than 0.03 m/s and 10° , respectively, as shown in Fig. 2.17. Therefore, the velocity perturbation is almost independent of the forcing frequency.

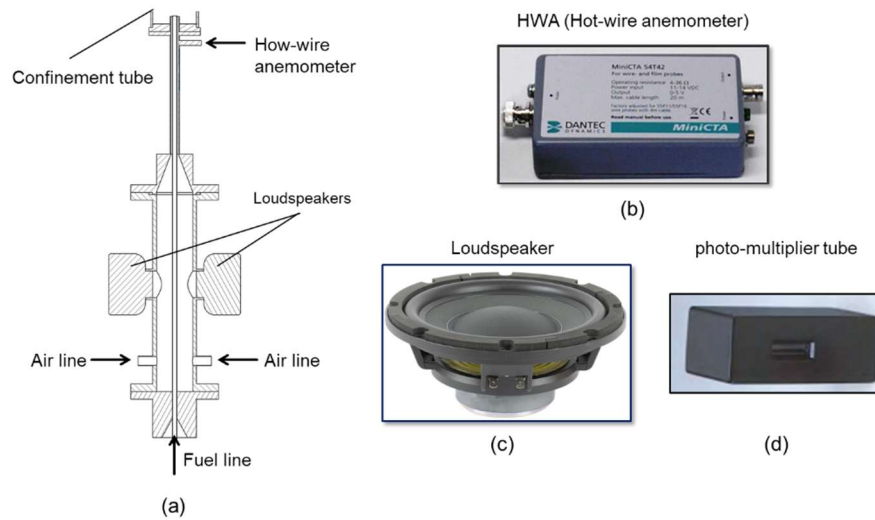


Fig. 2.17 (a) Schematic of the non-premixed flame burner described in Chapter 3, (b) hot-wire anemometry used for acoustic excitation measurement, (c) loudspeaker used for flow perturbation, (d) PMT used for heat release rate measurement.

Fig. 2.17 shows the equipment used for FTF analysis. Fig. 2.17 (a) shows the burner of the non-premixed flame in described in Chapter 3, with loudspeakers mounted on both sides. As noted above, the HWA is mounted 30 mm below the nozzle tip and acquires acoustic excitation data. The PMT is mounted near the quartz tube for configuration to obtain data.

2.4 NO_x measurement system

It has been reported that 4–5 times more soot formation [43,44] is discharged from the flame tip when separated by acoustic excitation, and NO_x concentrations decrease in the flame excitation with increasing resonance frequency [30]. The mechanism of the pinch-off flame that separates the flame is analyzed in Chapter 4, and the NO_x formation in such a flame is analyzed in Chapter 5. A TESTO 350 K gas analyzer was used to study NO_x concentrations. NO_x and CO sensor resolutions were 0.1 ppm and 1 ppm, respectively. The gas analyzer's probe is set where the combustion product is thoroughly mixed and is installed at a distance of more than twice the flame height from the nozzle tip [71]. NO_x measurement data was acquired once per second, and the data measured for more than 60 s in one experimental case were averaged.

The measured NO_x concentrations, χ NO_x (in ppm), were converted to an EINO_x value, which is a conventional parameter defined by the total amount of NO_x (in grams) produced when 1 kg of fuel is burned [72]. For H₂ and CO syngas jet flame, EINO_x is determined using:

$$\text{EINO}_x = 0.001 \left(\frac{\text{MW}_{\text{NO}_2}}{\text{MW}_{\text{fuel}}} \right) \chi_{\text{NO}_x} \frac{1}{2} \left(1 + \frac{4.76}{\phi_G} \right) \quad (2-7)$$



Fig. 2.18. TESTO 350 K measuring NO_x, CO, O₂, etc.

CHAPTER 3

COMPARISON OF FLAME RESPONSE CHARACTERISTICS BETWEEN NON-PREMIXED FLAMES AND PREMIXED FLAMES OF UNDER ACOUSTIC EXCITATION

3.1 Objectives

The importance of combustion instability research came to the fore in the development of rocket engines in the 1930s [73–75]. This instability phenomenon is known to occur in most combustion systems, such as gas turbines for aviation, power generation, boilers, and rocket engines. In the field of liquid rocket engines, it was confirmed that the atomization process between the fuel and oxidizer contributed to stability, and combustion instability was solved by structural changes such as injector shape change and baffle installation. In addition, various types of injectors have been used to solve the high-frequency combustion instability problem [76,77].

In the gas turbine field, studies involving self-excited combustion instability of liquid spray flames [78–80] and early detection research [81–84] of combustion were conducted. Also research to predict and prevent instability factors [26,85–88] at the design stage is actively underway. As mentioned above, combustion instability is divided into prediction and control, and it is vital to study the factors that cause combustion instability for prediction. Combustion instability factors are acoustic perturbation, heat-release perturbation, and velocity perturbation (or equivalence ratio perturbation). The intensity is amplified by positive feedback coupling in which these three factors affect other factors, resulting in periodic vibration. This instability can lead to blade damage, damage to burners, and the destruction of the combustion system.

The flame transfer function (FTF) is a tool that can effectively predict combustion instability [22,89–95], which is defined as the ratio of velocity perturbation to heat release perturbation. Varoquie et al. [96] studied the flame transfer response (n - τ model) according to acoustic excitation in a turbulent non-premixed flame. Large-eddy simulations (LES) and experimental data were compared, and the matching results suggested that FTF could be used as a useful tool to predict unstable phenomena. Durox et al. [24,97] studied the response

characteristics of the flames (conical, CSCF, “M,” “V”) with various geometries. It was confirmed that the perturbation intensity was locally independent of the FTF gain of the conical flame. Schuller et al. [23] studied the prediction of the FTF of a conical flame and V-flame. They performed comparisons of experimental, analytical, and numerical studies, finding that the response according to the acoustic excitation depended on the flame angle and mean velocity direction and that the reduced frequency and angle between the flame and the mean flow direction are independent parameters. The conical flames are due to the behavior of the low-pass filter and do not react sensitively to the velocity perturbation intensity.

The mixer concept of the twin annular premixing swirler (TAPS) combustor [1,9,98], an aviation gas turbine, uses a premixed flame as the main flame and a non-premixed flame as the pilot fuel for flame stability and NO_x reduction. Li et al. [11,99] conducted a study on the interactions between a pilot flame and V-shaped main flame according to flame perturbation to study the combustion instability of a gas turbine and analyzed the flame dynamic characteristics by simultaneously disturbing the pilot flame and the main flame. It was confirmed that the response of the pilot flame was a significant factor that increased the intensity of the flame and affected the stability of the main flame. Next, Sung et al. [100] studied the dynamic characteristics of a non-premixed flame and a premixed flame in a counterflow. It was confirmed that the premixed flame had a weak sensitivity to oscillation. Still, the non-premixed flame had varying sensitivity, and the amplitude response decreased as the excitation frequency increased. Finally, Durox et al. [101] studied gravity acceleration according to the geometry of the diffusion and premixed flames. The correlation between flame height, forcing frequency, and gravitational acceleration was derived by analyzing the flame response characteristics according to the acoustic excitation.

This study is a fundamental study on a combustion system that utilizes both non-premixed and premixed flames for specific reasons, such as the TAPS combustor of an aviation gas turbine. It is clear that the stability of non-premixed flame is superior to that of premixed flame. Accordingly, this study verifies flame stability by comparing two flames under similar combustor geometry and experimental conditions. This research has various applications such as in prediction and control techniques involving combustion instability frequency in TAPS combustors using two flame types. Therefore, in this study, the flame dynamic characteristics for the two flame types, the flame structure changes according to acoustic

excitation, the response characteristics of each flame type through FTF were confirmed, and the correlation between the flame structure and heat release was analyzed through flame height perturbation.

3.2 Experimental setup and methodology

Figures 3.1 (a) and (d) show the design of burners used to conduct a comparative study of the flame response characteristics of non-premixed and premixed flames. Figure 3.1(a) shows a non-premixed flame burner composed of an inner fuel nozzle and an outer air nozzle, and the inner diameters of the fuel nozzle and the air nozzle are 5 mm and 10.5 mm, respectively. Fuel and air were supplied from the bottom of the burner, and a flame surface was formed along the stoichiometric mixture fraction at the nozzle tip. The detailed shapes of the non-premixed flame and nozzle tip are shown in Fig. 3.1(b). The fuel/air gas started to mix at the bottom of the burner in the premixed flame, and the mixing action continued downstream along the premixing region. The mixed fuel/air reacted with a premixed flame of conical shape at the nozzle tip. The inner nozzle diameter of the burner is 10.5 mm.

Acoustic excitation is supplied with loudspeakers mounted on the side of the burner as a source, and the perturbation path is different depending on the burner type. For example, the non-premixed flame burner supplied the acoustic excitation source with a relatively higher flow to the airflow. On the other hand, the premixed flame burner provided acoustic excitation to the entire pipe because it was a single nozzle. A photomultiplier tube (PMT) with a sampling rate of 10 kHz was used for the flame transfer function (FTF) analysis, and the heat release rate was measured using a PMT equipped with an OH bandpass filter (LaVision, VZ-image Filter LIF for OH, enhanced, 310 ± 25 nm) to measure OH* emissions. Acoustic excitation signals were acquired using a hotwire anemometer (HWA), mounted 30 mm below the combustor nozzle tip. Forcing frequency was conducted in the range of 40–300 Hz at intervals of 20 Hz. The velocity perturbation intensity (u'/\bar{u}) was tested at 10% intervals in the range of 10 %–30%, and the velocity perturbation intensity was defined as the ratio of the average velocity (\bar{u}) and velocity perturbation (u) as the normalized intensity of the acoustic amplitude (λ).

To block the inflow of external air, circular quartz with a diameter of 35 mm was mounted on the top of the burner, and the flame structure was analyzed. To observe the flame structure, a high-speed camera (Highspeedstar 8, maximum resolution 1024×1024 @ 7 kHz) capable of photographing at 7 kHz @ 1024×1024 and an intensifier that amplifies the OH signal (Highspeed IRO) were used. Thus, the field of view is “35 mm \times 90 mm”, as shown in Fig. 3.1. A Nikon UV 100 mm f/2.8 lens and OH bandpass filter (LaVision, VZ-image Filter LIF

for OH, enhanced, 310 ± 25 nm) were used for the lens and filter used for measurement. To obtain OH* emissions sufficiently, an intensifier gate was set to 100 μ s.

OH is widely used as a flame marker. However, OH is generated not only in the reaction zone but also in the high-temperature product. The OH distributed over a wide area does not directly represent the flame surface. Therefore, many researchers have attempted to use OH as a flame surface. Steinberg et al. [102] used instantaneous flame surface tomography to determine the flame front in a premixed flame. They selected the flame front by comparing the positive profile curvature with the edge, which is the threshold of the gradient of the OH signal. Kaiser et al. [7] confirmed that the maximum temperature and stoichiometric contour coincided with the non-premixed flame and approximated the position of the stoichiometric contour from the OH-PLIF image. By matching the OH-PLIF images with the temperature field images, the rich-side edges of the OH structure were approximated with a stoichiometric contour. This study estimated the stoichiometric contour position through previous studies using images acquired through OH* chemiluminescence measurements. The stoichiometric contour of the non-premixed flame was assumed to be formed along the position where the OH intensity was strong, and the flame surface of the non-premixed flame was defined as the outer contour of the OH* chemiluminescence image. The flame front of the premixed flame was defined as the outer contour of the OH* chemiluminescence image.

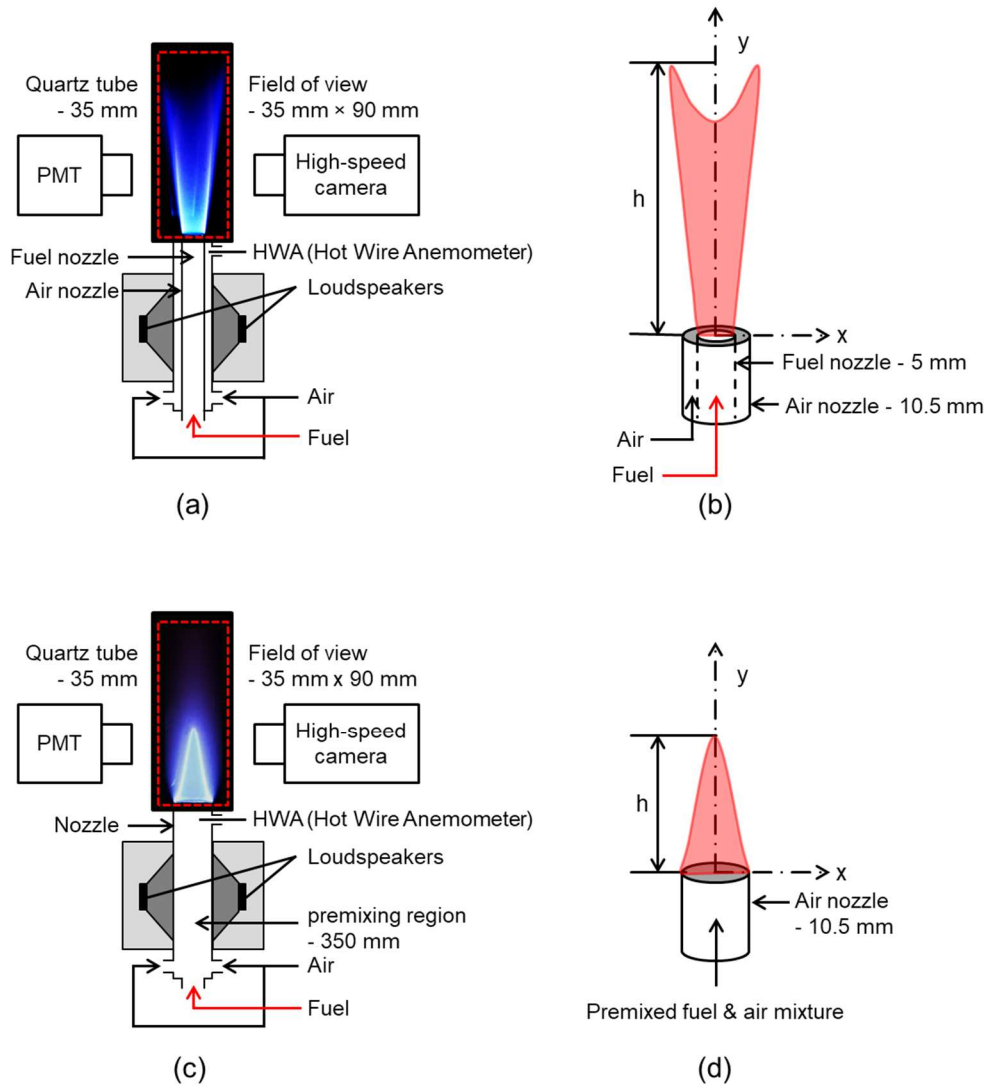


Fig. 3.1 (a) Schematic diagram of the non-premixed flame burner, (b) the nozzle tip and the flame shape, (c) schematic diagram of the premixed flame burner, (d) the nozzle tip, and the flame shape.

The experimental conditions used in this study are listed in Table 3.1. A mixed fuel of CH_4 and H_2 mixed at a volume ratio of 50/50% was used as the fuel, and the air was used as the oxidizer. The final goal of this study is pure hydrogen combustion (100% H_2). Therefore, after accumulating combustion stability data at a volume ratio of 50/50% of CH_4/H_2 , a study

on the increase of the H₂ volume ratio is conducted. The fuel/air bulk velocity of the non-premixed flame is laminar, supplying 2 m/s each. The premixed flame was tested at an equivalence ratio (ϕ) of 0.98, and the fuel/air mixture velocity was 2.4 m/s. For a comparison study of the dynamic behavior of the two flames, an experiment was performed on the premixed flame in near stoichiometry. As the flame surface is formed in the stoichiometric contour [59] of the non-premixed flame, the combustion conditions of the two flames were matched insofar as possible by the near stoichiometry ($\phi=0.98$) for the premixed flame. The forcing frequency is 40-300 Hz with an interval of 20 Hz, and the velocity perturbation intensity (u'/\bar{u}) is 10-30% with an interval of 10%.

Table 3.1 Experiment conditions.

Parameter		Conditions
Fuel composition		CH ₄ H ₂ =50/50% (%Vol)
Oxidizer		Air
Excitation frequency		40-300 Hz (20 Hz interval)
Velocity perturbation intensity (u'/\bar{u})		10, 20, 30%
Non-premixed flame	Fuel/air velocity	2 m/s each
	Fuel mass flow rate	CH ₄ /H ₂ =0.98/0.98 slpm
	Air mass flow rate	11.40 slpm
Premixed flame	Fuel/air mixture velocity	2.4 m/s
	Equivalence ratio (ϕ)	0.98

3.3 Flame appearance comparison between the non-premixed flame and the premixed flame

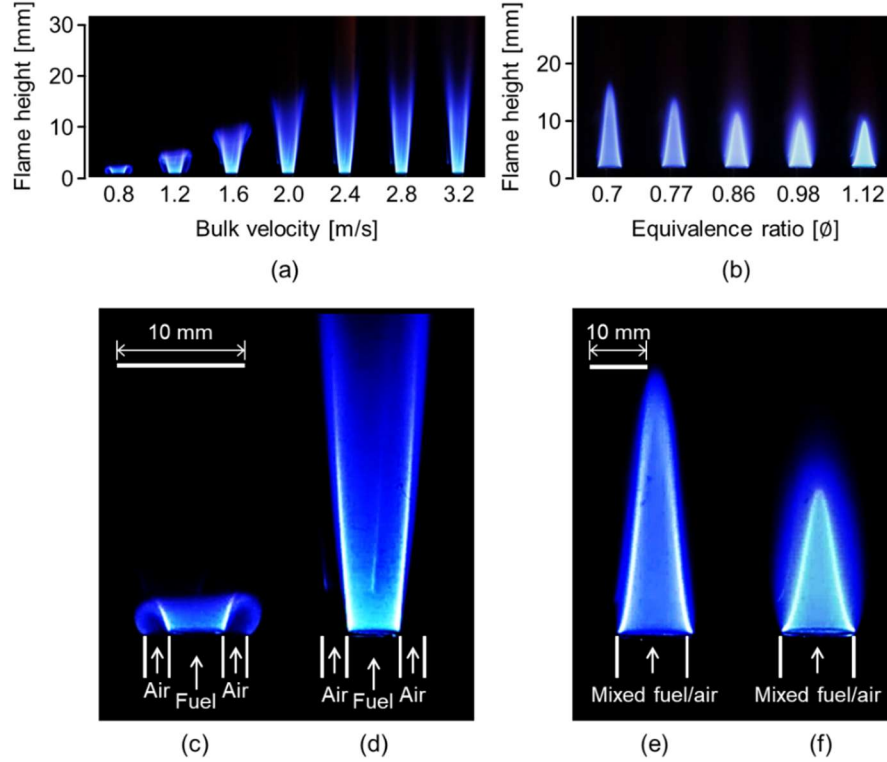


Fig. 3.2 Flame luminosity of burner equipped with confinement; (a) non-premixed flame shape according to the increase in fuel/air bulk velocity, (b) premixed flame shape according to the change in equivalence ratio, (c) bulk velocity = 0.8 m/s, (d) bulk velocity = 2.0 m/s and premixed flame (e) $\phi = 0.7$, (f) $\phi = 0.98$.

Figure 3.2 shows the flame luminosity when confinement was installed to block the inflow of external air. Flame measurement was measured with a DSLR camera (Canon EOS 7D, 24-70 mm f/2.8 lens) with an exposure time of 5 s. The non-premixed flames in Fig. 3.2(a) are the shapes of the flames under the same fuel/air bulk velocity. 0.8 m/s was a flat flame shape, and the flame was attached along the air nozzle. This phenomenon corresponds to the under-ventilated case of the Burke-Schumann flame [53]. The reason these flames were generated is straightforward. It appears when the outside air is completely blocked, and the environment in which limited fuel and air have to react. Due to insufficient oxidizer, a reverse flow motion

appears in which fuel gas injected from the fuel nozzle is attached to the rim of the air nozzle along with a small amount of air supplied from the air nozzle. Overall, it is an open flame tip under all velocity conditions because the air is insufficient, and the flame height increases as the air velocity increases. It appears when the external air is completely shut off, and limited fuel and air are required to react. Due to insufficient oxidizer, a reverse flow motion appears in which fuel gas injected from the fuel nozzle is attached to the rim of the air nozzle along with a small amount of air supplied from the air nozzle. The reverse motion of the flame can be observed locally, even at 1.2-1.6 m/s. Overall, it is an open flame tip in all velocity conditions because the air is insufficient, and the flame height increases as the air velocity increases. The flame height is maximum at 2.4 m/s and then does not increase further with increasing bulk velocity. In conclusion, the non-premixed flame in this study is an open flame tip under all flow conditions, which is an under-ventilated flame shape of the Burke-Schumann flame.

Figure 3.2(b) shows premixed flames with a conical flame shape. As the equivalence ratio (ϕ) increased, the flame height decreased, and the luminescence intensity increased. In this study, a non-premixed flame of 2.0 m/s and a premixed flame with an equivalence ratio of 0.98 was selected to compare the response characteristics of the two flames.

Figure 3.2 (c)-(f) shows a representative case of Fig. 3.2 (a)-(b) comparing flame structures of non-premixed and premixed flames. Figure 3.2 (c) and (d) show the appearance of a non-premixed flame with bulk velocities of 0.8 m/s and 2.0 m/s, respectively. At a bulk velocity of 2.0 m/s, a non-premixed flame has the shape of a jet flame, but a flat-shape flame of 0.8 m/s is characterized by reverse motion along the air nozzle. As mentioned, the reverse motion is a flame shape that appears due to insufficient air supplied when the external air is not introduced by confinement and corresponds to the under-ventilated case of the Burke-Schumann flame and a plateau-shaped flame [103].

All premixed flames had a conical flame shape, but the flame structures differed according to the equivalence ratio. For example, $\phi=0.7$ (Fig. 3.2 (e)) has a pointed-conical flame shape and is higher than $\phi=0.98$ (Fig. 3.2 (f)). This is because $\phi=0.98$ has a relatively shorter flame length than $\phi=0.7$, so all premixed fuel/air mixtures must react in a narrow section.

3.4 Flame dynamic characteristics under acoustic excitation of non-premixed flame

OH* chemiluminescence measurements were performed to compare the flame structure in response to the forcing frequency. Figure 3.3 shows the results measured in the forcing frequency range of 80-280 Hz when the velocity perturbation intensity (u'/\bar{u}) is 20%. Zero Hz without forcing is the case of a Burke-Schumann flame [103] with an open flame tip shape. It was confirmed that the oscillation is projected differently on the flame surface as the forcing frequency increases. For example, one undulation was projected onto the flame surface at 80 Hz, but three undulations were projected at 280 Hz. Therefore, it was confirmed that the representative flame dynamic characteristics caused by acoustic excitation in non-premixed flames were the movement of the flame surface.

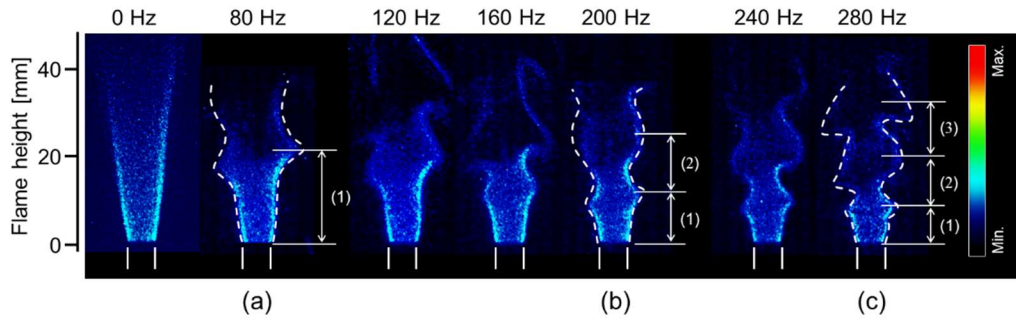


Fig. 3.3 As forcing frequency increases at $u'/\bar{u} = 20\%$, oscillation of the flame surface increases; (a) 80 Hz, (b) 200 Hz, (c) 280 Hz.

Figure 3.3(a)-(c) shows the flame surface oscillations according to the forcing frequency. The motion of the flame surface oscillation in this study is similar to the V-shape [24] and non-premixed flame of Burke-Schumann case [104]. Ahn et al., [104] observed the modulation shape of the flame deformed as the frequency increases, and the reason for creating the modulation of the flame surface is the behavior of the vortical structure formed inside the flame by acoustic excitation. The modulation characteristics of this flame surface were also confirmed in this study. Figure 3.3(a) shows that a single modulation was projected on the flame surface at 80 Hz, which was a relatively low frequency; however, as the frequency increased, the number of modulations increased, and it was confirmed that three

modulations appeared on the surface at 280 Hz(Fig. 3.3(c)). Accordingly, it was confirmed that the acoustic ($f=c/\lambda$) properties, which are the relationship between frequency (f) and wavelength (λ), appeared on the flame surface, and only the flame surface change appeared as the frequency increased.

Figure 3.4(a)-(c) shows the OH^* images according to phase at three forcing frequencies of 60, 80, and 240 Hz with three u'/\bar{u} . At u'/\bar{u} of 10%, the flame structure, and flame height changes are not noticeable at all three frequencies, but at u'/\bar{u} of 30%, the difference in the flame height due to the oscillation can be observed. It is a growing phase in which the flame height increases linearly from 90° to 180° , but the difference can be confirmed by the rapid decrease in the flame height at 270° . Therefore, it was confirmed that the magnitude of the flame height change increased as u'/\bar{u} increased. The factor that determines the flame height is fuel/air mixing. Therefore, as u'/\bar{u} increases, the mixing intensity of fuel/air increases, but the flame height decreases[35]. Therefore, it was confirmed that u'/\bar{u} is a parameter that affects the height of the non-premixed flame.

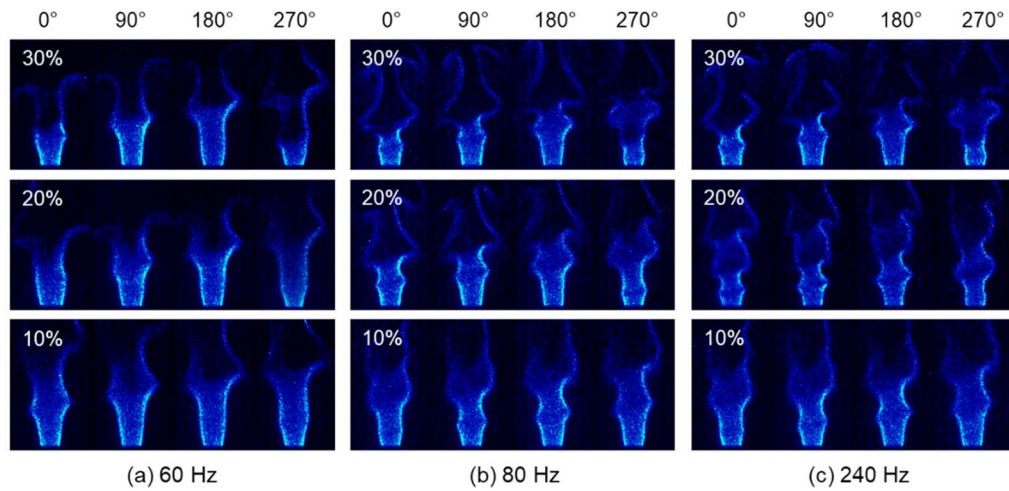
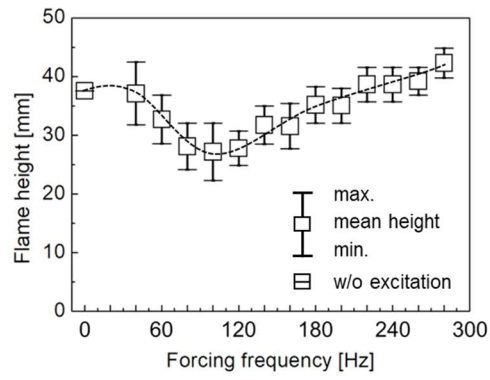
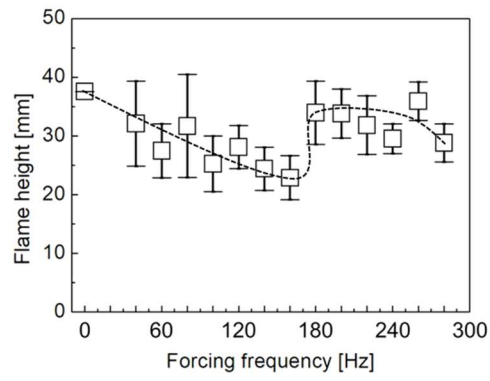


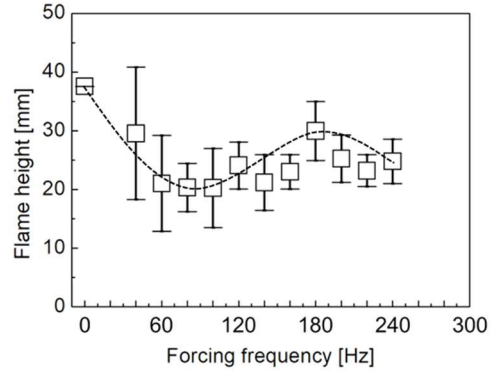
Fig. 3.4 OH^* chemiluminescence images for u'/\bar{u} and phase in the non-premixed flame, (a) 60 Hz, (b) 80 Hz, (c) 240 Hz.



(a)



(b)



(c)

Fig. 3.5 Flame height of the non-premixed flame with various u'/\bar{u}
(a) $u'/\bar{u}=10\%$, (b) $u'/\bar{u}=20\%$, (c) $u'/\bar{u}=30\%$.

Figure 3.5 shows the height of the non-premixed flame according to various u'/\bar{u} . First, flame height was calculated using OH^* chemiluminescence images. Fifty images per phase superimposed the acquired images, and a threshold value of 80% of the maximum intensity was selected to distinguish the maximum flame height of the overlapped images. Then, the maximum and minimum flame heights were calculated according to the phase. The flame perturbation magnitude can represent the difference between the maximum and minimum flame heights. This is shown in the 'box chart' in Fig. 3.5.

In Fig. 3.5(a) of 10% u'/\bar{u} , flame fluctuation maintains a certain interval even if the forcing frequency increases. However, at u'/\bar{u} of 20 and 30%, the magnitude of flame fluctuation in the local forcing frequency range increases. In particular, the magnitude is significant in the low-frequency range, and the magnitude maintains a specific interval as the forcing frequency increases. Therefore, it was confirmed that the flame fluctuation increased at low frequencies and u'/\bar{u} of 20% or more.

According to the overall forcing frequency, the flame height tends to decrease as u'/\bar{u} increases. 10% of u' is divided into sections showing a lower flame height section (40-160 Hz) than the stable flame height without acoustic excitation and high section (180-280 Hz), but 20% and 30% u' both represent heights lower than the stable flame height. Also, a u'/\bar{u} of 30% rather than 20% indicates a lower flame height in the overall forcing frequency range. Therefore, it was confirmed again that u'/\bar{u} is a significant parameter that has a major influence on the flame height and that the flame response is large in a relatively low-frequency range.

3.5 Flame dynamic characteristics under acoustic excitation of premixed flame

OH* chemiluminescence measurements were performed to compare the flame structure in response to the forcing frequency. Figure 3.6 shows the results measured in the forcing frequency range of 80-280 Hz when the velocity perturbation intensity (u'/\bar{u}) is 20%. The flame shape of a premixed flame without excitation is conical. The flame dynamic motion by perturbation is characterized by an oscillation motion that dances up and down. As with non-premixed flames, acoustic properties such as the projection of modulation onto the flame surface are not observed with premixed flames.

The characteristics of the dynamic behavior of the premixed flame by acoustic excitation are the flame tip and side shape. Unlike the non-premixed flame, an open-flame tip is a closed-flame tip in all forcing frequency ranges. The form of the flame side appears differently depending on the flame tip and is defined by categorizing it. For this, edge detection was performed along the periphery of the OH* image to distinguish the outline of the flame front. The flame shape was divided into five types according to the flame tip and side [105]:

- (a) Conically stable flame: A non-excitation stable flame.
- (b) Pointed-conical flame: The flame height is longer than that of a conical-stable flame, and the flame tip is pointed.
- (c), (e) Plateau flame: flame shape with a flame tip angle of nearly 180°.
- (d) and (g) plateau-necking flame: the flame tip angle is almost 180°, and the flame shape is concave in the middle.
- (f) Blunted-necking flame: The flame tip is blunt, and the flame is concave.

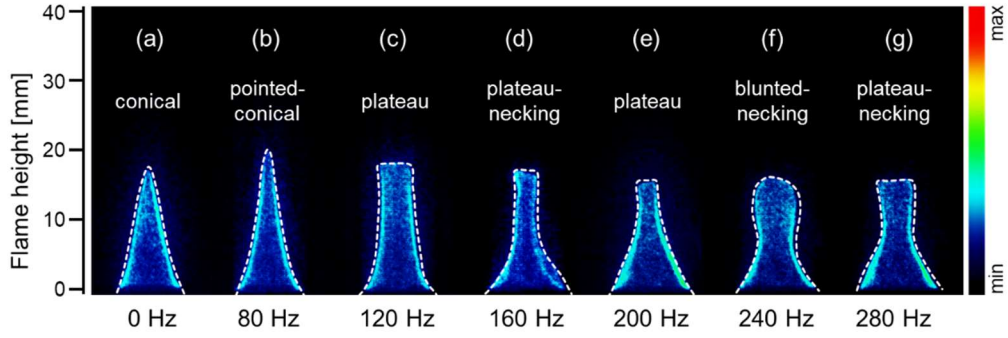


Fig.3.6 OH* chemiluminescence images of the premixed flame according to forcing frequency at $u'/\bar{u} = 20\%$ with 270° .

(a) conical-stable flame at 0 Hz, (b) pointed-conical flame at 80 Hz, (c) plateau flame at 120 Hz, (d) plateau-necking flame at 160 Hz, (e) plateau flame at 200 Hz, (f) blunted-necking flame at 240 Hz, (g) plateau-necking flame at 280 Hz.

Figure 3.7(a)-(c) shows the dynamic characteristics according to phase at forcing frequencies of 60, 80, and 240 Hz with three u'/\bar{u} . At a u'/\bar{u} of 10% for all three frequencies, the change in flame height is not noticeable depending on the phase. However, the flame height change is evident when u'/\bar{u} is 30%. At 60 Hz, a u'/\bar{u} of 20-30% is the growing phase in which the flame height increases linearly from 0 to 180° , and 180 - 270° is the shrink phase in which the flame shortens. Therefore, the difference between the maximum height and the minimum height of the flame is more significant at a 30% u'/\bar{u} than at 20%. It can be confirmed that the flame height characteristics are similar even at 80 and 240 Hz. Therefore, u'/\bar{u} can infer the magnitude and proportional tendency of the flame height fluctuation.

The flame tip has a sharp acute angle at low forcing frequencies, but as the frequency increases, the flame tip tends to change to a blunt obtuse angle. For example, a flame tip of 60 Hz showed an overall pointed-flame tip. On the other hand, 80 and 240 Hz offer a pointed-flame tip only at u'/\bar{u} of 10%, and the change in the flame tip angle varied between 20% and 30%. Furthermore, at 30% u'/\bar{u} of 240 Hz, show pinch-off [106], a phenomenon in which the flame tip is separated appears, and it has been reported that this phenomenon increases the soot occurrence [43,44]. Pinch-off flames also appear at different forcing frequencies. At some forcing frequencies, it occurs even at 20% u'/\bar{u} , however, most occur at u'/\bar{u} 30% or higher. Ahn et al. [104] presented the conditions for the occurrence of pinch-

off for the forcing frequency and u'/\bar{u} . In conclusion, it was confirmed that the representative flame dynamic characteristics by acoustic excitation in the premixed flame are the oscillation movement of the flame and the change in the flame tip and side. Therefore, it was confirmed that the non-premixed flame and premixed flame had different flame dynamic characteristics according to the acoustic excitation.

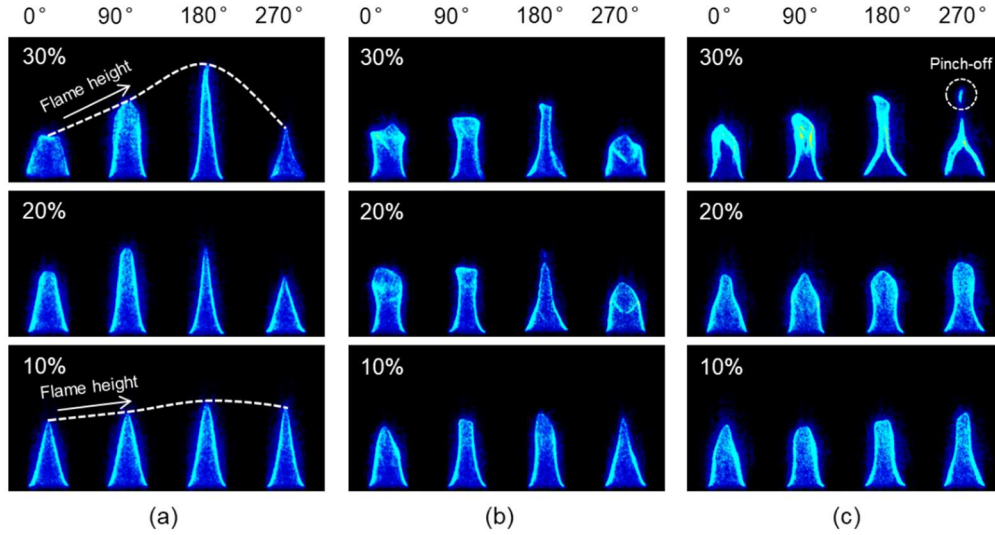
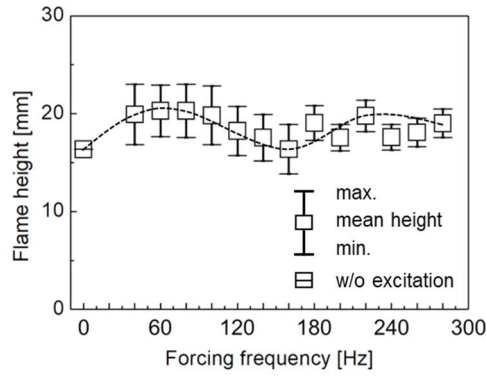
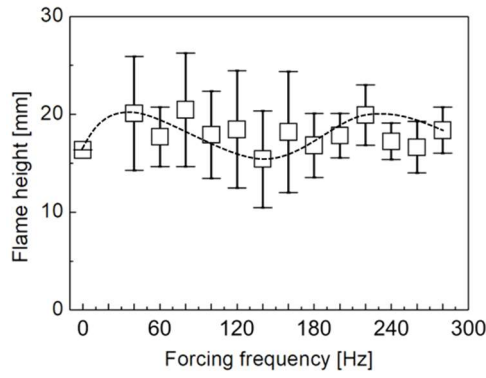


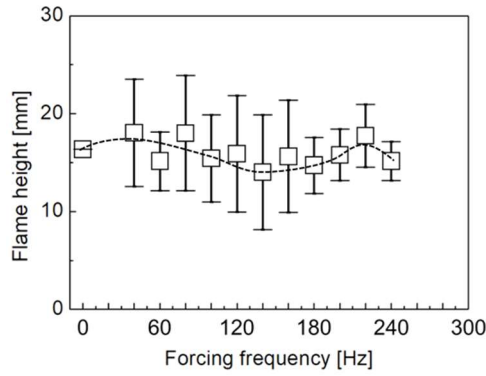
Fig. 3.7 OH* chemiluminescence images with various u'/\bar{u} and phase in the premixed flames, (a) 60 Hz, (b) 80 Hz, (c) 240 Hz.



(a)



(b)



(c)

Fig. 3.8 Flame height of the premixed flame with various u'/\bar{u} , (a) 10%, (b) 20%, (c) 30%.

Figure 3.8 shows the forcing frequency and the flame height according to u'/\bar{u} . Flame height was calculated using the same method as for non-premixed flame. At u'/\bar{u} of 10%

and 20%, it was confirmed that the height was higher than the stable flame height, which is non-excitation, and it was slightly decreased at 30%. In the low-frequency region, the magnitude of min-max of the flame height was relatively large, but as the frequency increased, the magnitude of the min-max decreased. These tendencies are all present in u'/\bar{u} of 10%–30%. In particular, at u'/\bar{u} of 20–30%, low frequencies below 160 Hz show large fluctuations, and the fluctuation magnitude decreases as the frequency increases. Therefore, in the low-frequency range, the flame fluctuation was significant owing to the strong flame response. Still, a weak flame response and small flame fluctuation tendency were confirmed as the forcing frequency increased. In non-premixed flames, external disturbances enhance fuel/air mixing and reduce flame length [107]. Therefore, while the overall average flame length decreases with the increase of u'/\bar{u} , since the premixed flame is a mixed fuel/air, it indicates that the average flame length does not change significantly with the increase of u'/\bar{u} even with external disturbance.

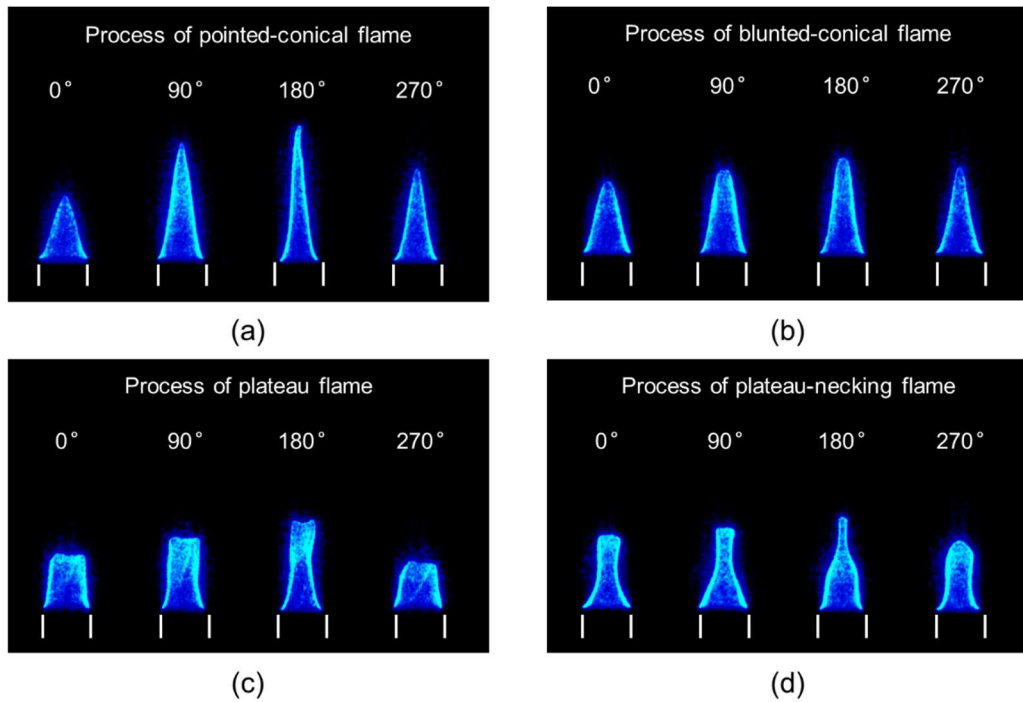


Fig. 3.9 Flame deformation process according to flame tip and side shape.
(a) 100 Hz at $u'/\bar{u} = 10\%$, (b) 120 Hz at $u'/\bar{u} = 10\%$, (c) 140 Hz at $u'/\bar{u} = 20\%$, (d) 280 Hz at $u'/\bar{u} = 20\%$.

Figure 3.9 shows four flame deformation processes. Figure 3.9(a) shows the process of blunted-conical flame. The tip is blunter than the conical-stable flame, and the flame height is slightly increased. In general, the flame tip is blunt in all phases, and the flame stretch is not large depending on the phase.

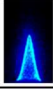
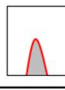
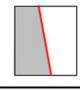
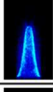
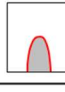
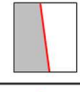
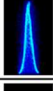
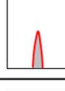
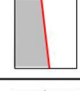
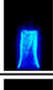

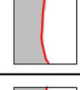
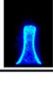

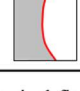
Figure 3.9(b) shows the process of a pointed-conical flame. It is characterized by a sharper flame tip than a conical-stable flame and a longer stretch depending on the phase. The magnitude of the min-max flame height of the flame is large. It shrinks the most at 0° and stretches the most at 180° .

Figure 3.9(c) shows the process of the plateau flame. It is characterized by a flame geometry that is different from a general conical flame. The flame tip has a flat shape and a lower flame height than a conically stable flame. At 0 - 180° , the flame grows and stretches, the sides' form becomes concave, and the width of the flame tip narrows. At 270° , the flame was compressed, and the width of the flame tip widened. Therefore, if the flame height increases, the width of the tip becomes narrow, and if the flame height becomes shorter, the width becomes wider.

Figure 3.9(d) shows the process of plateau-necking flame. The flame tip is flat, and the middle of the flame side has a concave-convex periodically repeating shape. The flame side concave at 0° becomes convex at 180° and concave again at 270° to become a blunted-flame tip. When the flame side was concave, the flame tip was flat, and when the flame side was convex, it became a blunted-flame tip.

Table 3.2 defines the flame shape according to the flame tip, side, and flame height. The representative image that best expresses the structural characteristics of the premixed flame was selected, and a name was defined for each flame structure. During acoustic excitation, various flame structures appear with respect to the forcing frequency. Gotoda et al. [103] determined the shape of the flame structure to be conical, oscillating, and plateau flame using a flame curvature at the tip. Cuquel et al [108] performed FTF analysis on the flame base and front motion. Therefore, flame motion analysis plays an important role in heat-release analysis.

Table 3.2 premixed flame categorizes various flame structures caused by acoustic excitation into the shape of the flame side, flame tip, and flame height.

shape of flame tip		shape of flame side	flame height	graphical illustration of flames	
				flame tip	flame side
Conical-stable		criterion (conical)	criterion ($h_{c.f.}$)		
Blunted-conical (100 Hz)		\approx conical	$h_{c.f.} <$		
Pointed-conical (120 Hz)		\approx conical	$h_{c.f.} <$		
Plateau (140 Hz)		conceve	$> h_{c.f.}$		
Plateau-necking (280 Hz)		conceve	$> h_{c.f.}$		

$h_{c.f.} = h_{\text{conical flame}}$

A conical-stable flame is a condition with no acoustic excitation and is the standard flame for the flame structure. A blunted-conical flame (100 Hz) has a blunt flame tip and a flame height that is slightly higher than that of a stable flame. A pointed-conical flame (120 Hz) has a pointed flame tip and a height longer than a stable flame. A plateau flame (140 Hz) has a concave flame side, flat flame tip, and lower flame height than a stable flame. A plateau-necking flame (280 Hz) has a concave flame side, a narrower flame tip width than a plateau flame, and a lower flame height than a stable flame. Both the plateau and the plateau-necking flame side are concave, and the flame tip is flat, and it can be seen that there is a correlation between the flame side and the flame tip. In this study, the tendency of a specific flame structure to appear at a specific frequency was confirmed, and various structures were identified as the frequency increased.

3.6 Comparison of the flame response characteristics between non-premixed and premixed flames

Figure 3.10 shows the OH* images to compare the flame structures of the non-premixed and the premixed flames. The left side of each image is a non-premixed flame (NPX), and the right side is a premixed flame (PX). Figure 3.10 (a) shows stable flames of 0 Hz without acoustic excitation, and Fig. 3.10(b) shows the flame excitation with a forcing frequency of 160 Hz. The stable non-premixed flame has the shape of a jet flame and an open flame tip, and the stable premixed flame has the shape of a conical flame and has a closed flame tip. The most significant difference between the two flames was the appearance of the flame tip. This difference is due to the difference in the fuel and air supply methods or flame type.

The two flames have a difference in flame dynamic motion due to acoustic excitation. Confinement determines the flame's appearance and motion. When the external air is blocked by confinement, the shape of a non-premixed flame is an open flame tip at all velocity conditions, but without confinement, the form of a non-premixed flame is the same as that of a candle flame. In other words, the flame shape was determined by the amount of air. However, for premixed flames, the flame shape does not change appreciably according to the confinement. This is because the chemical reaction was caused by the mixed fuel/air mixture.

The second factor that determines the flame appearance motion is the difference in acoustic excitation. The burner of the premixed flame supplies acoustic excitation to the entire nozzle because of the single nozzle. Still, the burner of the non-premixed flame consists of a fuel nozzle and an air nozzle, and in this study, acoustic excitation is supplied only to the air nozzle. In a non-premixed flame, a vortical structure is generated in the flow field by perturbing the airflow. Accordingly, oscillation [24] appears on the flame surface, and helical motion [109] occurs along the surface. On the other hand, the entire flame shows an up-down dancing motion in the premixed flame due to the periodic reverse-forward cycle [110,111]

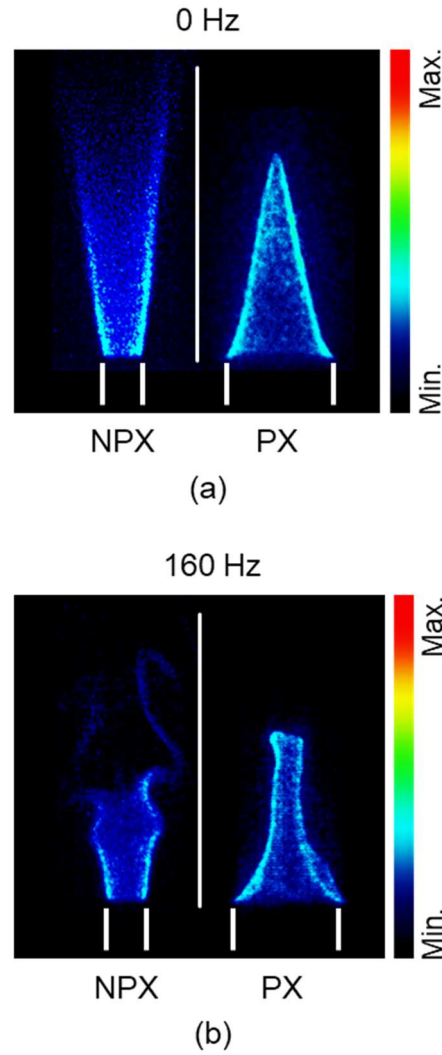


Fig. 3.10 Flame structure of the non-premixed (NPX) and premixed flame (PX) through OH^* images, (a) without excitation, (b) excitation frequency at 160 Hz.

It was confirmed that the flame dynamic characteristics of the non-premixed flame and premixed flame differed according to the acoustic excitation. To approach this more quantitatively, the flame transfer function (FTF) was calculated by measuring the heat emission perturbation. FTF is defined as the ratio of heat release rate fluctuation to velocity fluctuation and is expressed as Equation (3-1) below.

$$F(\omega) = \frac{q'/\dot{Q}_0}{u'/U_0} = G(\omega)e^{i\phi(\omega)} \quad (3-1)$$

$G(\omega)$ in equation (3-1) is the gain of the flame transfer function and represents the response intensity, $\phi(\omega)$ is the phase difference, and the real part is the natural frequency. The imaginary part is the growth rate of the initial instability factor, and the instability is amplified when it is negative.

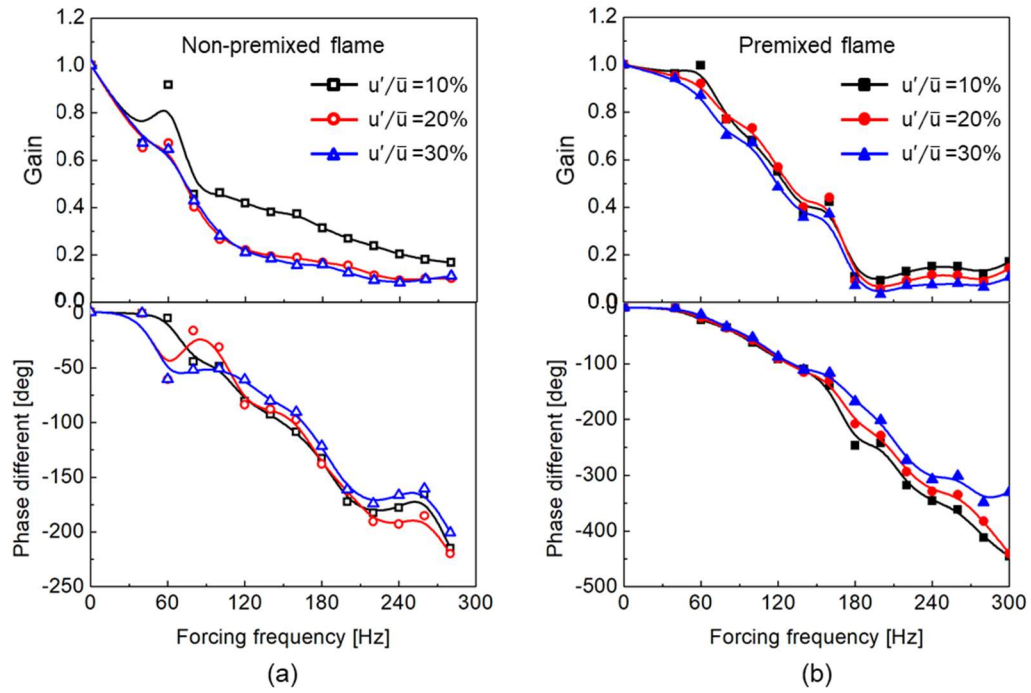


Fig. 3.11 Gain and phase of the flame transfer function;
(a) the non-premixed flame, (b) the premixed flame.

Figure 3.11(a) shows the result of the FTF (gain and phase) of the non-premixed flame. The forcing frequency was in the range of 0-280 Hz, and u'/\bar{u} was a hotwire anemometer, and the heat release rate was measured using the PMT. When u'/\bar{u} is 10%, the gain has a local maximum at 60 Hz and another recovery at 80 Hz, and at a forcing frequency of 100 Hz or higher, the gain decreases with values larger than u'/\bar{u} of 20% and 30%. Also, u'/\bar{u}

of 20 and 30% has the same gain value in most forcing frequency ranges. As such, it was confirmed that the flame transfer function of the premixed flame exhibits different nonlinear characteristics of 10% and 20, 30% of u'/\bar{u} , that is, the heat release rate according to a given u'/\bar{u} is different. The phase difference was defined as the time difference between the velocity perturbation and heat release fluctuation. In this study, the phase difference according to u'/\bar{u} is not prominent, and although there is a locally small peak, it is generally a linear slope. The phase difference is the largest at u'/\bar{u} of 60 Hz, and this characteristic is the same as the gain. The local peak appearing at 60 Hz is presumed to be a phenomenon that occurs because the flame fluctuation is not large at 10% of u'/\bar{u} , but is large at 20% and 30%. Therefore, it is necessary to analyze the magnitude of flame height perturbation according to the forcing frequency and u'/\bar{u} .

Figure 3.11(b) shows the result of the gain and phase of the premixed flame. This shows a tendency different from that of a non-premixed flame. The perturbation of heat emission according to u'/\bar{u} is a constant linear characteristic. It is the behavior of a low-pass filter [23] that decreases up to 180 Hz and converges to a constant value after 180 Hz. Therefore, at a forcing frequency of 180 Hz or higher, it can be predicted that the flame is stable regardless of u'/\bar{u} , and the results that do not react sensitively are presented in the results [23,24,97]. In the phase difference, all u'/\bar{u} have the same value up to 160 Hz, but from 180 Hz to every u'/\bar{u} , a constant value difference is shown, and the phase decreases. This trend is similar to that of the gain.

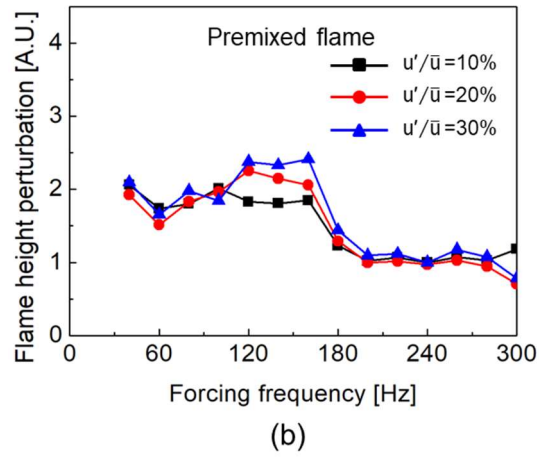
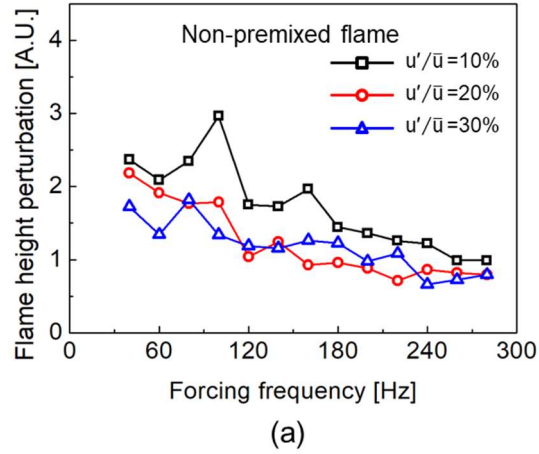


Fig. 3.12 The correlation between the flame height perturbation and the forcing frequency, (a) the non-premixed flame, (b) the premixed flame.

Figure 3.12 shows the results of the flame height perturbation of the non-premixed flame and premixed flame. The FTF calculation was applied to calculate the ratio of flame height perturbation and u'/\bar{u} , and the formula is as follows:

$$\text{Flame Height Perturbation} = \frac{h'/\bar{h}}{u'/\bar{u}} \quad (3-2)$$

h' is the magnitude of the flame height fluctuation according to the acoustic excitation, and \bar{h} is the mean flame height. u' and \bar{u} are the same as those previously mentioned. As another

parameter that can judge the flame dynamic characteristics of two flame types, the trend of heat-release rate is analyzed by analyzing the flame height perturbation according to the forcing frequency and u'/\bar{u} .

Figure 3.12(a) shows the result of the flame height perturbation of the non-premixed flame. It tends to decrease overall, among which 10% of u'/\bar{u} shows a high value, but 20 and 30% of u'/\bar{u} have similar values. Therefore, the characteristics categorized according to u'/\bar{u} are the overall results of non-premixed flames, the non-premixed flame showed nonlinear characteristics, and it was confirmed that the tendency of the heat-release rate (Fig. 3.11 (a)) and flame height perturbation (Fig. 3.12(a)) was similar.

Figure 3.12(b) shows the result of the flame height perturbation of the premixed flame. It tends to decrease overall, but u'/\bar{u} of 20% and 30% increases at 120 Hz and recovers again at 160 Hz. Except for 120-160 Hz, the other forcing frequencies show the same flame height perturbation value according to u'/\bar{u} . Therefore, it was confirmed that the premixed flame had a linear characteristic as a whole, except for the range of the forcing frequency, and it was similar to the tendency of the heat-release rate (Fig. 3.11(b)) and flame height perturbation (Fig. 3.12(b)). As the characteristics of flame height perturbation according to acoustic excitation are similar to the results of the heat-release rate, it suggests the possibility of using it as a parameter that can simply show the characteristics of the heat-release rate.

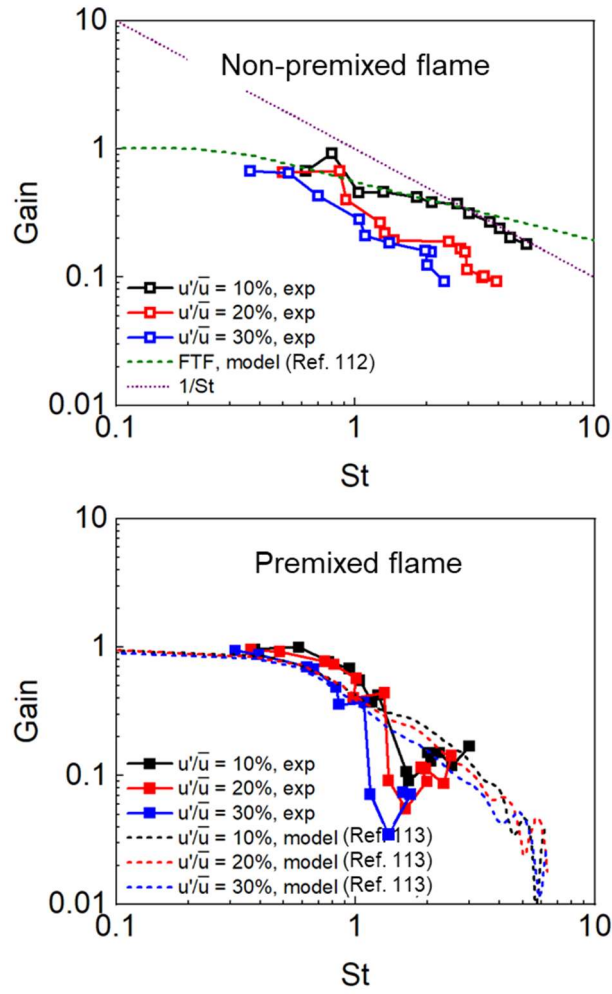


Fig. 3.13 The gain of the flame transfer function as a function of Strouhal number, (a) non-premixed flame, (b) premixed flame

Figure 3.13 shows the gain of the flame transfer function for both the non-premixed and premixed flames. These gain values are described as a function of the Strouhal number for comparison with the results from the model [112,113]. The Strouhal number (St number) is defined as $St = fh/u$, where f is the forcing frequency, h is the mean flame height, and u is the mean bulk velocity.

In the non-premixed flame, the Peclet number consists of mass diffusivity, input mean velocity (average velocity during one period), fuel nozzle diameter of 10, and stoichiometric

mixture fraction of 0.06 in the modeling study. However, 86 of the Peclet number and 0.053 of the stoichiometric mixture fraction were used in this study. Therefore, the effect of the Peclet number difference can affect the heat-release behavior. According to [112] the critical Strouhal number that changes the proportional relation from $\sim 1/St^{0.5}$ to $\sim 1/St$, decreases as the Peclet number increases. Therefore, the Strouhal number range in this study belongs to the proportional relationship of $\sim 1/St^{0.5}$ with 10 of the Peclet number in the analytical result.

The experimental result of 10% u'/\bar{u} matches the modeling result up to 3 of three Strouhal numbers. However, the proportional relationship changes to $\sim 1/St$ at Strouhal numbers higher than 3. This phenomenon occurred because the Peclet number in this study was higher than that of the modeling result. The 20% and 30% of u'/\bar{u} also show a relationship of $\sim 1/St$. Therefore, the nonlinear effect depends not only on the magnitude of the gain but also on the critical Strouhal number. Similar to the Peclet number effect [112], the critical Strouhal number decreases as the velocity perturbation increases.

In terms of the premixed flame, nonlinear behavior is observed in the modeling. As increasing u'/\bar{u} , the gain of the flame transfer function decreases as same as the experimental result. However, there is a significant difference in the gain when the Strouhal number is higher than 1. Although a rapid decrease and recovery of the gain magnitude can be found in both results, a significant gain drop occurs at a much lower Strouhal number in the experiments. This can be caused by parameters that are not included in the Strouhal number, such as the laminar flame speed and burner geometry. In addition, the unusual flame shape such as the plateau or necking shown in Fig. 3.6 can affect the local curvature related to the flame speed, $S_L = S_L^0(1 - Lk)$ where S_L is the flame speed, S_L^0 is the laminar flame speed, k is the local flame curvature, and L is the Markstein length [113]. However, the analytical results can help predict the heat release oscillations at frequencies higher than 300 Hz, which is the maximum frequency of this study.

CHAPTER 4

PINCH-OFF PROCESS OF BURKE-SCHUMANN FLAME UNDER ACOUSTIC EXCITATION

4.1 Objectives

Acoustic excitation is used in a variety of applications such as pollutant reduction [114–116] and flame stabilization [117–119]. It is also a common tool for studying combustion instability [73,94,112,120], which is known to be caused by the interaction of heat release perturbation, equivalence ratio perturbation, and acoustic excitation perturbation. Various excitation devices (e.g., loudspeakers and rotating disks) have been employed to perturb the flow and generate arbitrary unstable states in the combustor. In contrast, in non-premixed flames with dynamic characteristics, such as flame surface fluctuation, vortex shedding, flickering flame, and reverse flow behaviors have been reported.

Another characteristic of acoustic excitation is an enhanced mixing of fuel and air, which affects the pollutants formed during the combustion process. For example, Kim et al. [30] studied the relationship between the resonance frequency and the NO_x concentration in a non-premixed flame. In all excited cases over a wide frequency range, they observed a lower NO_x emission than in the non-excited cases. In particular, a significant decrease in the NO_x concentration was observed in the resonance frequency of the flame. These pollutant studies were conducted not only in laminar flames [31–34] but also in turbulent flames [35–37], and upon considering the effects of increasing pressure [38–40]. The pinch-off flame tip is the main factor contributing to the generation of the pollutant [41], and the residence time of the pocket flame separated from the main flame is longer than that of other normal flames. Since the soot growth time increases with increasing residence time of the flame, greater quantities of pollutants are emitted from the pocket flame [42]. Shaddix et al. [43,44] compared the soot volume fraction between a laminar steady-non-premixed flame and a pinch-off flame, and found that soot production was four times greater in the latter. Furthermore, a qualitative agreement was verified with computational studies [44], as well as between different sets of experimental results. Overall, soot growth occurs for a longer period in pinch-off flames compared to in steady flames, and that soot production also

increases due to the higher temperature maintained in the hot product.

Previously suggested mechanisms of pinch-off include local flame extinction [45,46], phenomenon caused by vortex flow [47,48], and the inflow of air. Strawa et al. [45] examined the dynamic characteristics of jet diffusion flame with increasing pressure during acoustic excitation at 9 Hz. The flame breakup phenomenon was measured by schlieren, and the buoyancy-driven breakup process was followed near the nozzle outlet. In their analytical and numerical study of the flame response oscillation, Tyagi et al. [49] suggested that pinch-off occurs at a certain frequency and critical amplitude. Unfortunately, that study was limited to low frequencies (below 1 Hz), and a wider frequency range needs to be considered to identify the conditions (frequencies and amplitudes) of pinch-off. Magina [42] reported that frequency and amplitude are the key parameters that control the pinch-off behavior and performed a theoretical analysis of pinch-off according to the axial diffusion effect. After considering cases with/without the axial diffusion effect, it was confirmed that axial diffusion causes pinch-off over a narrower Strouhal number range. Gao et al. [47] studied the dynamic characteristics of flames excited at 100 Hz through simultaneous OH planar laser-induced fluorescence (PLIF) and particle image velocimetry (PIV) measurements. Pinch-off flame of various amplitudes was confirmed at 100 Hz, and local pinch-off was suggested by the large vortex structure. However, acoustic excitation was applied only to the fuel supply line, and the fuel jet was accelerated by the influence of the Kelvin-Helmholtz (K-H) instability [30] under acoustic excitation.

In non-premixed flames, the flame structure is affected by the strain rate [50], and it has been suggested that a higher strain rate changes the flame surface area and increases the chemical reaction rate. Acoustic excitation affects the flame length, flame shape, and local flame extinction [51] due to enhanced mixing in the flame, and these physical characteristics can be analyzed in terms of the strain rate. Carrier et al. [50] suggested that the strain rate affects the flame in two ways. First, a high strain rate causes inflow of fresh air into the flame zone, and so the flame is first cooled and eventually quenched or extinguished. Secondly, a high strain rate extends the flame surface, which in turn increases the area in contact with the flame front as well as the chemical reaction rate. Donbar et al. [52] analyzed the strain rate along the CH reaction layer through simultaneous measurement of CH PLIF and PIV in a turbulent non-premixed flame. Various trends were observed, such as large curvatures, cusps, near-extinction, expansion due to entrained air, and increase in flame area due to vortex rollup.

Kim et al. [30] performed simultaneous measurement of OH PLIF/PIV in turbulent non-premixed flames, and observed local flame extinction due to excessive strain rate in the high strain region. The authors suggested that local flame extinction is caused by two factors. The first is an increased diffusive influx of fuel by the internal vortex, and the second is air entrainment by the stretching motion of the external vortex. In previous studies [30,52], strain rate analysis was performed with regard to the flame contour derived from instantaneous data. However, the pinch-off behavior is a periodic phenomenon on a non-premixed flame, and so a time-resolved study is necessary to determine the mechanism. In this current investigation, strain rate analysis is performed with time-course measurements.

The specific aims of this study are analyzing and understanding the mechanism of pinch-off through examination of the flame response and the vortex-flame interactions in a laminar non-premixed flame (Burke-Schumann flame [51,121]) under acoustic excitation. The range of pinch-off in terms of forcing frequency and velocity perturbation intensity (u'/\bar{u}) is confirmed, and the characteristics of the Strouhal number according to the flame height definition in the pinch-off flame region are identified. In addition, different trends are identified for the main flame height and the total flame height (i.e., with pocket) according to the velocity perturbation intensity. Furthermore, the vortical structure is measured in the nonreacting flow, the effects of the vortex flow and the reverse flow in the pinch-off flame in the reacting flow are investigated, and time-resolved strain rate and axial velocity analyses are performed.

4.2 Experimental setup and methodology

Pinch-off in a non-premixed flame by acoustic excitation was examined in a Burke-Schumann flame [51]-based combustor (Fig. 4.1(a)). The diameter of the fuel nozzle was 5 mm, the diameter of the air feeding line was 50 mm, and the interior of the combustor was a square column with a cross section of 50 mm \times 50 mm. All sides of the combustor windows were equipped with quartz to block external air. Acoustic excitation through loudspeakers (Woofer, 8 inch, 100 W) and amplifier allowed us to independently control the forcing frequency (Hz) and the velocity perturbation intensity (u'/\bar{u}). This (u'/\bar{u}) is the ratio of the axial velocity perturbation (u') to the average velocity (\bar{u}), and it is defined as the normalized intensity of the acoustic amplitude (λ). The signals for the air and fuel were monitored through hot wire anemometer (HWAs). The HWAs were mounted on the fuel feeding line and the air feeding line, both at 30 mm below the nozzle tip to minimize phase error according to the 'mounting height'. The same forcing frequency was simultaneously applied to the fuel/air feeding lines. The phases of fuel and air were adjusted within 5° (in-phase) to perform the experiment.

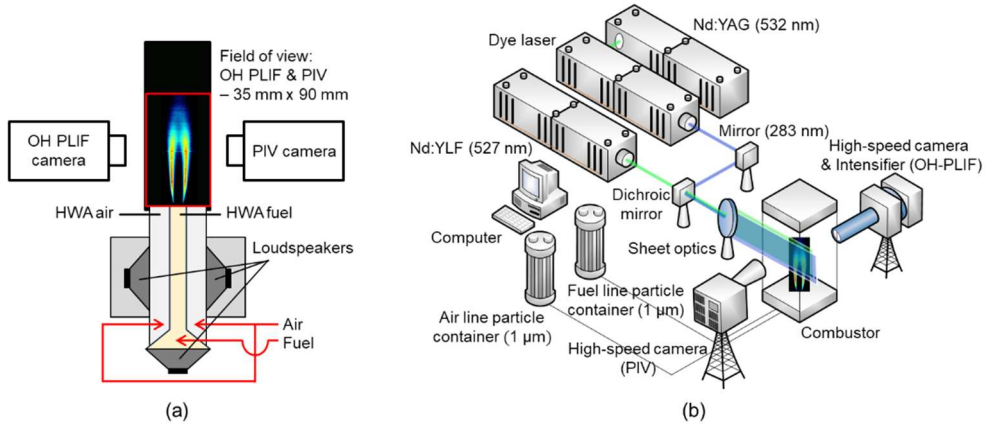


Fig. 4.1 Schematic diagram of the experimental setup. (a) non-premixed flame combustor. (b) laser system for simultaneous OH-PLIF and PIV measurements.

OH PLIF and PIV measurements were performed to analyze the flame dynamics and flow field under acoustic excitation (Fig. 4.2(a)). The repetition rate of the laser measurement was 2,500 Hz, and the field of view was 35 mm \times 90 mm, as shown in Fig. 4.1(a). The OH radical was imaged using an Nd:YAG laser (Edgewave IS-200-2-L, 532 nm; 11.71 mJ/pulse at 7

kHz) and a dye laser (Sirah, Credo-Dye-LG-24). Rhodamine 6G was used as the dye for wavelength tuning (283 nm; 0.4 mJ/pulse at 7 kHz), and a high-speed camera (Highspeedstar 8, maximum resolution 1024×1024 @7 kHz) was used for recording. The OH intensity was amplified using an intensifier (Highspeed IRO). The laser was tuned to the Q₁(6) transition of OH radical near $\lambda = 282.94$ nm. A Nikon UV 100 mm f/2.8 lens and an OH PLIF bandpass filter (LaVision, VZ-image Filter LIF for OH, enhanced, 310±25 nm) were also used. The light of 532 nm wavelength irradiated from a Nd-YAG pump laser was adjusted to 283 nm by passing through the frequency doubler and Rhodamine 6G dye cell inside the dye laser. To measure the OH PLIF, it was necessary to monitor OH radicals in the excited state. However, OH* chemiluminescence will also be recorded if the exposure time is too long. To acquire only the OH fluorescence, an intensifier gate of 1 μ s was used to exclude the OH* chemiluminescence signal.

The setup for flow field analysis consisted of an Nd:YLF laser (Photonics Industries DM, 527 nm; 2.7 mJ/pulse @3.5 kHz), a high-speed camera (Highspeedstar 8, maximum resolution 1024×1024 @7 kHz), a NIKKOR AF MICRO 105 mm f/2.8 lens, and a 527 nm bandpass filter (LaVision, VZ-image Filter 527±10 nm). As shown in Fig. 4.2, the time interval for simultaneous measurement of the OH PLIF and PIV was 200 μ s, and the resolution of the PIV image was 1.11×10^{-1} mm/pixel. LaVision's DaVis version 8.3 was used for post-processing in the velocity field analysis. The first-pass passed 5 with an interrogation window size of 32×32 pixels and an overlap of 75%, while the second-pass passed 4 with an interrogation window size of 24×24 pixels and an overlap of 75%. Fast Fourier transform (FFT)-based cross-correlation was also carried out. Particles of zirconium oxide (ZrO₂, 1 μ m diameter, 99.5% on metals basis excluding Hf, Hf <100 ppm) were used in the air and fuel line containers.

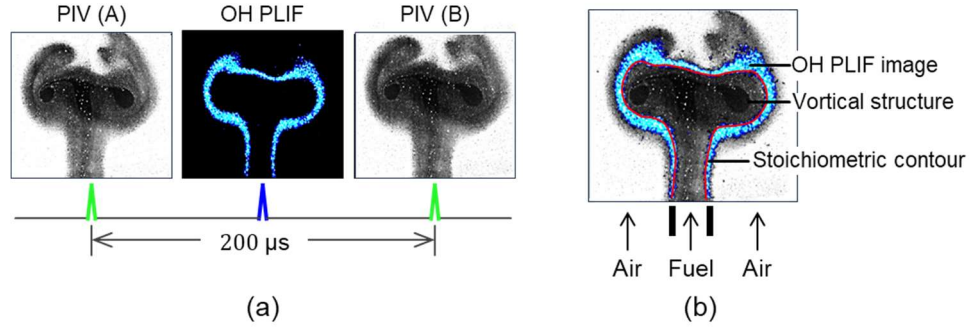


Fig. 4.2 (a) Time sequence of simultaneous OH PLIF/PIV measurements at $f = 80$ Hz and $(u'/\bar{u}) = 50\%$. (b) Overlapping PIV image and OH PLIF image to verify their consistency, the vortical structure obtained by acoustic excitation, and the stoichiometric contour expected to be located on the “rich side” of the OH layer [7].

Figure 4.2(a) shows the laser sequence and simultaneous measurements from the OH PLIF and PIV laser systems. PIV images A and B, which were obtained using a dual pulsed laser, have a time interval of $200 \mu\text{s}$, and the laser shot for OH PLIF measurement was irradiated between the two PIV shots.

OH radical is widely used as a flame marker because of its advantage of high signal level at low pulse laser. However, OH does not directly indicate the flame surface because OH is generated not only in the reaction zone but also in a wide distribution up to high temperature products. As an attempt to identify OH on the flame surface or front, Steinberg et al. [102] used the gradient of the OH fluorescence signal to identify the flame front at premixed flame. Kaiser et al. [7] confirmed that the maximum temperature and stoichiometric contours coincide in the non-premixed flame and that the peaks of the OH and OH LIF signals are located on the lean side of the reaction zone. It was confirmed that the rich side of the OH structure and the maximum temperature were almost the same, and the rich side of the OH structure was indicated by the flame front. Based on this, Boyette et al. [122] reported a study to define the flame front in the rich side of the OH layer at high pressure. Similar to the previous study, in this study we can assume that the stoichiometric contour is located on the “rich side” of the OH layer. Therefore, the flame surface is defined as the rich side of the OH layer. Edge detection was performed using a gradient-based Canny algorithm with a phase-averaged OH PLIF image to approximate the flame surface contour at the OH layer. To distinguish the reaction zone, the threshold value was set to 80% of the maximum intensity.

Table 4.1 Experimental conditions.

parameter	Condition
Fuel composition	H ₂ /CH ₄ -75/25% (0.89/0.3 slpm)
Oxidizer	Air (214 slpm)
Fuel velocity	1.0 m/s (Re=98.79)
Air velocity	1.0 m/s (Re=1456.6)
Forcing frequency	0-300 Hz
Velocity perturbation intensity (u'/\bar{u})	0-50%
Velocity perturbation intensity (u'/\bar{u}) of Pinch-off flame	80 Hz, 50%
PIV seeding particle	ZrO ₂ (d=1 μ m)

The experimental conditions of this study are listed in Table. 4.1. Acoustic excitation was performed in the frequency range of 0-300 Hz at 10 Hz intervals, and the velocity perturbation intensity (u'/\bar{u}) was within 0-50% at 5% intervals. Initially, experiments were conducted at various frequencies to analyze the global characteristics. Subsequently, the pinch-off mechanism was analyzed under the specific conditions of 80 Hz forcing frequency and (u'/\bar{u}) = 50%. The mixed fuel consisted of 25 vol.% methane (CH₄) and 75 vol.% hydrogen (H₂), and air was used as the oxidizer. The proportion of hydrogen in the fuel was higher than that of methane in order to stabilize the flame during acoustic excitation. The fuel and air were both supplied at a bulk velocity of 1 m/s, since the same bulk velocity helps minimize the effect of shear between air and fuel at the boundary layers and allows us to focus on the flow oscillation (supplied by the loudspeaker) as a dominant influence on the flow disturbance. When the fuel and air have different velocities, K-H instability due to the two boundary layers affects the flow, and an outer vortex [30] can be created. As mentioned in the Introduction, the occurrence of a pinch-off flame depends on the excitation frequency and amplitude [49], in addition to the flow within the vortex structure [47]. In this study, we utilized the following conditions to systematically examine the pinch-off flame phenomenon:

(a) Simultaneous excitation of the fuel/air feeding lines. When only one line is excited, there is a difference in the velocity at the boundary layer due to a change in medium velocity. Thus, K-H instability occurs [30]. To minimize the effect of K-H instability, we used simultaneous

excitation of the fuel/air feeding lines.

(b) Identical excitation frequency and velocity perturbation intensity for the fuel and the air, which were achieved through independent control of the fuel and the air. Even at the same excitation frequency, different velocity perturbation intensities can induce the K-H instability due to the velocity difference.

(c) Experiments were performed when the phase difference between the fuel and the air was within 5° to minimize any flow changes caused by destructive interference from the phase difference. The phases were also controlled individually for the fuel and the air.

4.3 Flame response characteristics under various excitation frequencies

This study aims to measure the OH PLIF images under flow oscillation and to map the parameter range of pinch-off flame. Pinch-off is a local flame extinction phenomenon, in which the flame is separated under specific acoustic excitation conditions into a 'main flame' attached to the nozzle tip and a separate 'pocket flame' [46,49] Tyagi et al. [49] suggested that pinch-off flame occurs at an appropriate excitation frequency and amplitude, although they only examined a limited frequency range of below 1 Hz. In this study, the conditions for pinch-off flame were mapped in a much wider frequency range (0–300 Hz in 10-Hz intervals) and $(u'/\bar{u}) = 0\text{--}50\%$ in 5% intervals.

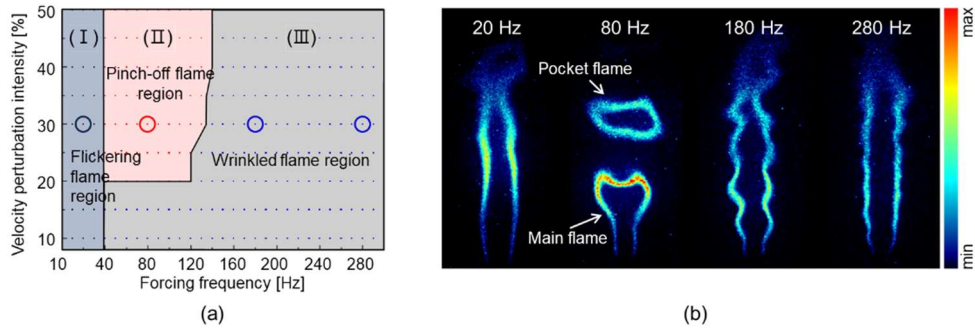


Fig. 4.3 (a) Mapping result of the pinch-off flame conditions and flame dynamic characteristics in terms of the forcing frequency and velocity perturbation intensity (u'/\bar{u}).
(b) OH PLIF images at $(u'/\bar{u}) = 30\%$.

In Fig. 4.3, the flame dynamics is classified into three types ((I)–(III)) depending on the forcing frequency and the velocity perturbation intensity (u'/\bar{u}) during acoustic excitation. Representative OH PLIF images in Fig. 4.3(b) were obtained under the conditions marked by large dots in Fig. 4.3(a). According to the Richardson number [123], momentum-dominant flames occur in this study when the velocity perturbation intensity is 20% or more. Region (III), which is the wrinkled flame region, is distributed at low velocity perturbation intensity (u'/\bar{u}) within 40–120 Hz, and over the entire region at forcing frequency >120 Hz. In this region, several periods of undulation are projected onto the flame, which can be clearly observed at 180 Hz in Fig. 4.3(b). However, as the frequency increases further, the periods of undulation almost disappear because the flame response becomes insignificant at high

excitation frequencies.

In region (I), flickering flames appear in the low frequency range of 10–30 Hz. These flames show no pinch-off and are strongly perturbed in the axial direction. Pinch-off does not occur in this region even when the value of (u'/\bar{u}) increases, because the perturbation caused a large flame response. However, when the fuel bulk velocity and the flame height increased, pinch-off was confirmed at 10–30 Hz.

As mentioned above, region (II) is the pinch-off flame region, where the critical frequency and velocity perturbation intensity at the point of flame separation were clarified in this study. During pinch-off, the flame is separated into the 'main flame' and the 'pocket flame' [46,49], as shown by the image on the right-hand side of Fig. 4.3 (frequency: 80 Hz). Pinch-off mainly occurs in the frequency range of 40–120 Hz, and also at higher velocity perturbation intensities when the frequency is >120 Hz.

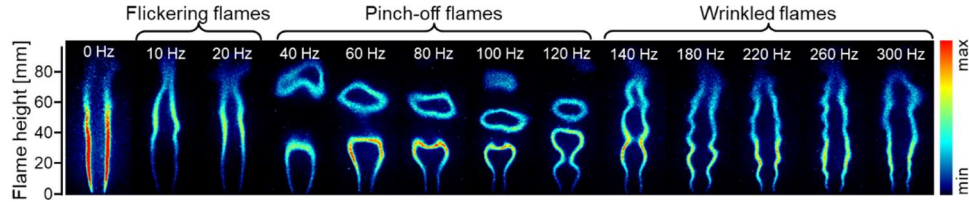


Fig. 4.4 Flame images from instantaneous OH PLIF measurement at various frequencies and $(u'/\bar{u}) = 30\%$.

Based on the map of Fig. 4.3, flame responses were measured at various excitation frequencies and $(u'/\bar{u}) = 30\%$ through OH PLIF images and shown in Fig. 4.4. At 0 Hz (steady state without flow fluctuation), the flame tip was not closed. The reason for such a shape is that the fuel is completely burned and the OH concentration at the tip is low, hence the shape of the Burke-Schumann flame appears [121]. Pinch-off flame occurs in the frequency range of 40–120 Hz. As the frequency increases, the distance between the main flame and the detached pocket flame decreases. When this distance becomes zero, the flame is no longer pinched-off. For example, the main flame-pocket flame distance was the narrowest at 120 Hz, and the narrowest flame was observed at 140 Hz.

4.4 Flame response characteristics of pinch-off process at 80 Hz

Instantaneous OH PLIF measurements were performed to observe the flame dynamic characteristics at various (u'/\bar{u}) values when the excitation frequency was fixed at 80 Hz. The images in Fig. 4.5(a) were obtained under the conditions where pinch-off occurs. The information therein is quantitatively expressed in Fig. 4.5(b) by the flame height, which was calculated as the phase average using 50 images per phase. The flame height was measured based on the flame surface previously defined as the rich side of the OH structure. Two different flame heights can be defined. The main flame height is the distance between the nozzle tip and the main flame tip, whereas the total flame height includes the pocket flame. The distance between the top of the main flame and the bottom of the pocket flame is defined as the main flame-pocket flame distance.

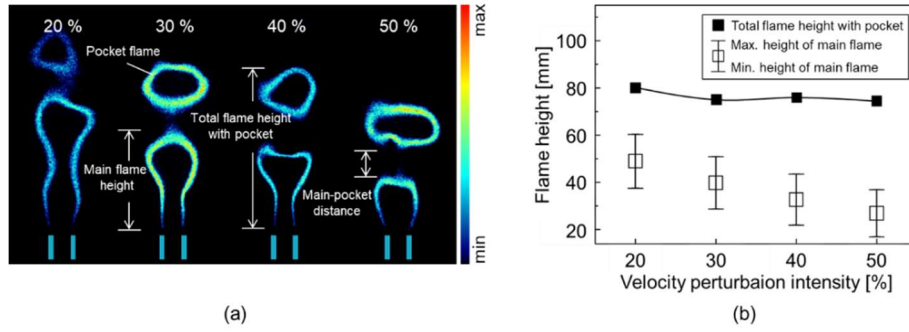


Fig. 4.5 (a) Flame dynamic characteristics at various (u'/\bar{u}) values and forcing frequency of 80 Hz, which is in the pinch-off range. (b) Flame height at 80 Hz for different (u'/\bar{u}) values.

In the range of $(u'/\bar{u}) = 20\text{--}50\%$, where the pinch-off flame appears, the main flame height decreases linearly with increasing (u'/\bar{u}) due to the fact that the mixing intensity is increased by acoustic excitation. As a result, the flame surface area is increased by acoustic excitation, which increases the mixing of fuel and air to produce more intense chemical reactions. On the other hand, the total flame height (i.e., including the pocket flame) is constant when (u'/\bar{u}) increases. It seems that the change in flame height on the mixing intensity only affects the main flame. This is because the change in the main flame height according to (u'/\bar{u}) is remarkable. At $(u'/\bar{u}) = 20\%$, the average main flame height is 50 mm, while at $(u'/\bar{u}) = 50\%$ it is ~ 30 mm. On the other hand, the total flame height is constant at ~ 80 mm. Therefore, we

confirmed that mixing influenced the flame height locally due to the different tendencies of the two flame heights. Overall, the mixing positions where the flame is separated are located close to the nozzle upon increasing (u'/\bar{u}) , while the height of the pocket flame remains constant.

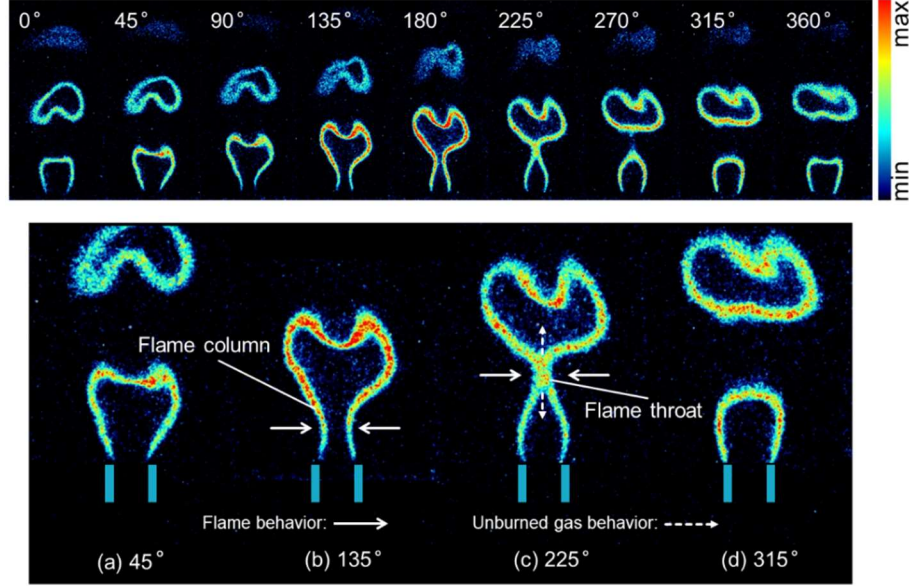


Fig. 4.6 Pinch-off process at 80 Hz and $(u'/\bar{u}) = 50\%$ and deformation of the pinch-off flame by acoustic excitation under four different phases of (a) 45°, (b) 135°, (c) 225°, and (d) 315°.

Figure 4.6 displays a pinch-off flame during one cycle under an 80 Hz forcing frequency and $(u'/\bar{u}) = 50\%$. The total flame height increases linearly during this cycle, and pinch-off occurs when the two flame columns become deformed at specific positions. The deformation process takes place at 135–225°, and beyond 270° the main flame and pocket flame can be clearly distinguished. The distance between the main flame and the pocket flame remains relatively constant. It should be noted that other reactive pockets remain above the newly detached pocket in Fig. 4.6, and these multiple hot pockets are expected to increase pollutant production and discharge.

To analyze the relationship between flame deformation and pinch-off flame under acoustic excitation, data at the four phases in Fig. 4.6 ((a) 45°, (b) 135°, (c) 225°, and (d) 315°) were extracted together with the corresponding flame behavior. The flame column displays

deformation beyond 135° , and the flame throat is formed at 225° prior to becoming completely separated at 315° . Of particular note is the flame behavior at 225° . More specifically, the separation process of the pinch-off flame throat exhibits compression-expansion characteristics. Compression takes place on both sides beyond 225° , while the top and bottom of the flame exhibit expansion. A negative flow behavior, known as the reverse flow [39], has also been reported in axial flows due to the suction phase of the acoustic excitation. This phenomenon suggests that ambient air is also entrained inside the nozzle. Indeed, a similar reverse flow was observed herein, and its effect can be seen in the behavior of flame throat separation.

4.5 Flame response characteristics at pinch-off boundary

The frequency-dependent flame height and the flame response characteristics at the boundary of the pinch-off region were further analyzed. Instantaneous OH PLIF measurements were carried out at $(u'/\bar{u}) = 50\%$ and forcing frequency of 0–300 Hz in 10-Hz intervals. In the pinch-off region, the two defined flame heights (main flame height and total flame height) display different trends with regard to frequency as shown in Fig. 4.7, wherein the fluctuation caused by acoustic excitation is expressed in a box chart. More specifically, large fluctuations occur in the range of 10–30 Hz, while almost no fluctuation exists above 150 Hz. This is due to the different flame responses, since the dynamic characteristics over 150 Hz cause waveforms to form in the OH PLIF image.

The two definitions of flame height are introduced here to clearly distinguish the flame height in the pinch-off flame region. Although the detached pocket is not part of the main flame, we wish to provide accurate and fundamental data regarding the flame residence time as potentially useful information. Upon increasing the frequency, the main flame height tends to decrease, while the total flame height remains constant despite the enhanced mixing by the forcing frequency and (u'/\bar{u}) . For the main flame, its height decrease is dramatic but limited to the pinch-off region. The total flame height is not significantly affected by the frequency or by (u'/\bar{u}) under the current experimental conditions.

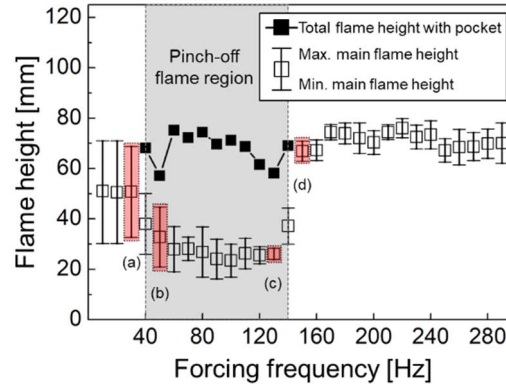


Fig. 4.7 Flame height measured at $(u'/\bar{u}) = 50\%$, showing the characteristic flame behavior at the boundary on both sides of the pinch-off flame region. Points (a)–(d) are within 10 Hz from the boundary.

Figure 4.8 shows the flame dynamic characteristics at the transition point from non-pinch-

off to pinch-off at the low-frequency boundary (40 Hz) and the high-frequency boundary (140 Hz). The flames in parts (a) and (b) exhibit great fluctuation in the axial direction. On the other hand, the fluctuations in parts (c) and (d) are not particularly noticeable, although fluctuation waves are visible in the OH PLIF image. Although these flames are in the same pinch-off region, those at 50 and 130 Hz behave very differently. At 50 Hz, pinch-off appears as a type of fluctuation behavior in the axial direction, while at 130 Hz two fluctuation waves are formed on the flame surface, and the main flame-pocket flame distance is narrow compared to that at 50 Hz. It can therefore be inferred that the flame responds to the acoustic wavelength, since it seems to project the waveform onto the flame surface. Moreover, the long wavelengths at low frequencies do not generate waveforms, and the flame surface motion appears like random flickering. In contrast, a high frequency causes the flame surface to generate clear waveforms.

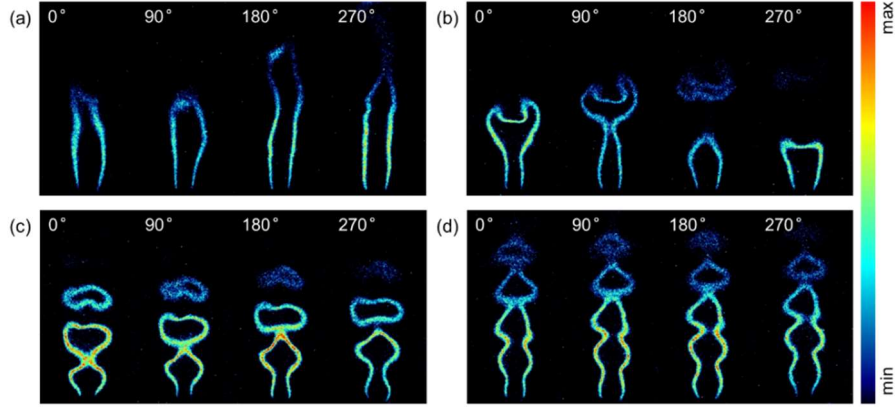


Fig. 4.8 Flame dynamic behavior at the boundary of the pinch-off region in Fig. 4.7 at $(u'/\bar{u}) = 50\%$ and four frequencies: (a) a flickering flame at 30 Hz, (b) a pinch-off flame at 50 Hz, (c) a pinch-off flame at 130 Hz, and (d) a wrinkled flame at 150 Hz.

The two different definitions of the flame height correspond to different Strouhal numbers, which are defined as follows:

$$St = f \cdot l/u \quad (4-1)$$

where u is the bulk velocity [m/s], f is the forcing frequency [1/s], and l is the considered flame height [m]. In the pinch-off region of 40–120 Hz, the St number shows different characteristics from those observed at other frequencies. Figure 4.9 plots the calculated St using the two flame heights. The St number defined using the total flame height shows a linear relationship to the frequency, whereas that defined using the main flame height displays nonlinear characteristics in the pinch-off region. These results indicate that the use of both sets of flame height data and their corresponding St numbers is essential for analyzing the residence times of pollutants in the pinch-off flame.

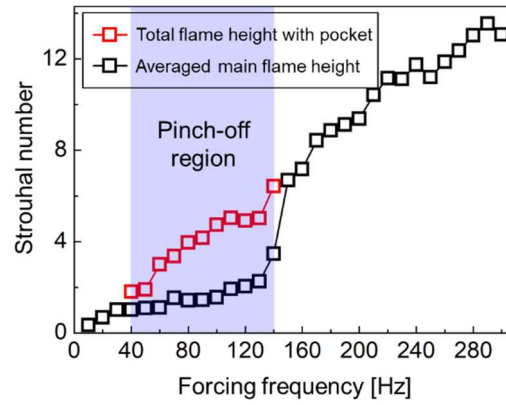


Fig. 4.9 St numbers calculated using the main flame height and the total flame height.

4.6 Vortex-flame interaction and strain rate analysis for the pinch-off mechanism

To analyze the pinch-off mechanism, simultaneous measurements of OH PLIF and PIV measurements were carried out at a specific frequency and velocity perturbation intensity. We first analyzed the formation of vortex and reverse flow through flow oscillation measurement in a nonreacting flow by Mie scattering, and then we studied the correlation between the vortex and pinch-off flame in the reacting flow. Subsequently, to understand local physical phenomena during the pinch-off process, the strain rate for the change in flame surface and the reverse flow caused by flow oscillation were analyzed in the reacting flow. The Mie scattering and simultaneous measurements of OH PLIF/PIV were all conducted at a repetition rate of 2,500 Hz.

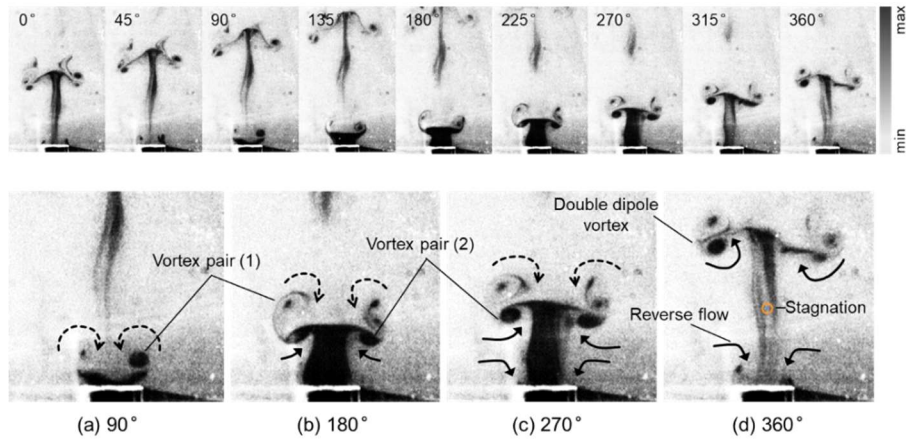


Fig. 4.10 Images of nonreacting flow measured by Mie scattering at 80 Hz and $(u'/\bar{u}) = 50\%$. Two pairs of vortices were created with different directions of rotation, and the reverse flow was confirmed.

In the nonreacting flow without chemical reaction, we examined how oscillation affects the flow (whether the effect is related to the pinch-off or not) and the vortex generation process without expansion by combustion. Mie scattering was measured at a repetition rate of 2,500 Hz under a forcing frequency of 80 Hz and $(u'/\bar{u}) = 50\%$. As shown in Fig. 4.10, two pairs of vortices (double dipole vortex) were created by acoustic excitation. The first vortex pair (1) was formed at the nozzle tip (0°), the second vortex pair (2) was created at

180–270°, and the two pairs coexisted at 270–360°. Bryant et al. [124] studied the formation of a double dipole vortex in tidal flow, and presented vortex formation by flow into the nozzle. Lakshminarasimhan et al. [110,111] examined the reverse flow into nozzle under acoustic excitation and confirmed it through acetone PLIF measurement. In the present study, a reverse flow due to acoustic excitation was also observed, and the generation of a vortex by this effect was confirmed. Vortex pair (1) was created by two steps of inflow and outflow. When the flow pointed into the nozzle, friction force from the inner wall of the nozzle created this vortex through the outflow. This inflow can be confirmed by a lower density (black area) in the fuel column at 360°. When there was no reverse flow, the fuel density should keep constant, such as the case at 180°. At 270°, in addition to the decreased density when the inflow started, the diameter of fuel column also decreased compared to the case at 180°. After that, the density decreased significantly at 360°. Lakshminarasimhan et al. [111] suggested the existence of a stagnation point between $1*D$ and $2*D$ (D : nozzle diameter), and confirmed that the reverse flow and rising airflow due to the vortical structure exist simultaneously. The current study also showed that the reverse flow and rising airflow due to the vortical structure at the $1*D$ – $2*D$ position affect the fuel density. This result is similar to the flame behavior in Fig. 4.6(c), where the flame throat is divided into the main flame and pocket flame. Through Mie scattering measurement, we confirmed the formation of vortical structure and flow characteristics in nonreacting flow due to reverse flow.

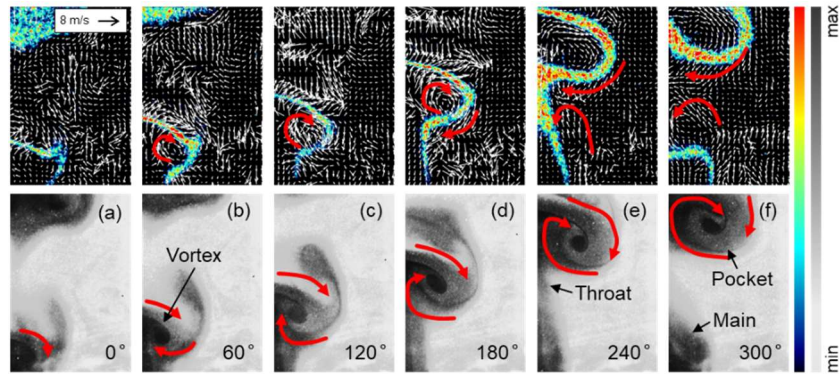


Fig. 4.11 Pinch-off due to the interaction between the flame and vortex at 80 Hz and $(u'/\bar{u}) = 50\%$.

In the reacting flow, characteristics of vortex flow and vortex-flame interaction were

analyzed using simultaneous measurement of OH PLIF/PIV at a repetition rate of 2,500 Hz under the same experimental conditions as in Fig. 4.10. The top row in Fig. 4.11 displays OH PLIF images with overlapping vector fields, and the bottom row displays the raw PIV images in grayscale. Because Fig. 4.10 depicts the nonreacting flow, it contains no effects such as gas expansion and buoyancy by combustion, while these effects are displayed in Fig. 4.11. In Fig. 4.11, the location and volume of the vortical structure match those of the OH PLIF images, confirming their consistency. Similar to the nonreacting flow of Fig. 4.10, vortical structure due to acoustic excitation was also observed in Fig. 4.11. The vortex generated at 0° rotates clockwise and stretches in the axial direction. When the continuously rotating vortex structure reaches a certain height, a flame throat emerges in the flame column (240°), and the main and pocket flames are completely separated at 300° . Lakshminarasimhan et al. [111] showed that there is a flow in the negative axial direction due to the suction phase that flows into the nozzle during acoustic excitation. Likewise, this study shows an effect of reverse flow where the flow is in the negative axial direction. The effect of this reverse flow is also seen in the flame throat of Fig. 4.6(c), Fig. 4.10 (nonreacting flow), and also Fig. 4.11 (reacting flow). Through Mie scattering and simultaneous measurement of OH PLIF, it was found that the pinch-off is physically caused by the interaction of the reverse flow and the vortical structure. In other words, the flame throat is formed by interaction between rotational motion of the vortical structure that causes entrainment of air and reverse flow in the negative axial direction, and such interaction further plays a major role in separating the flame.

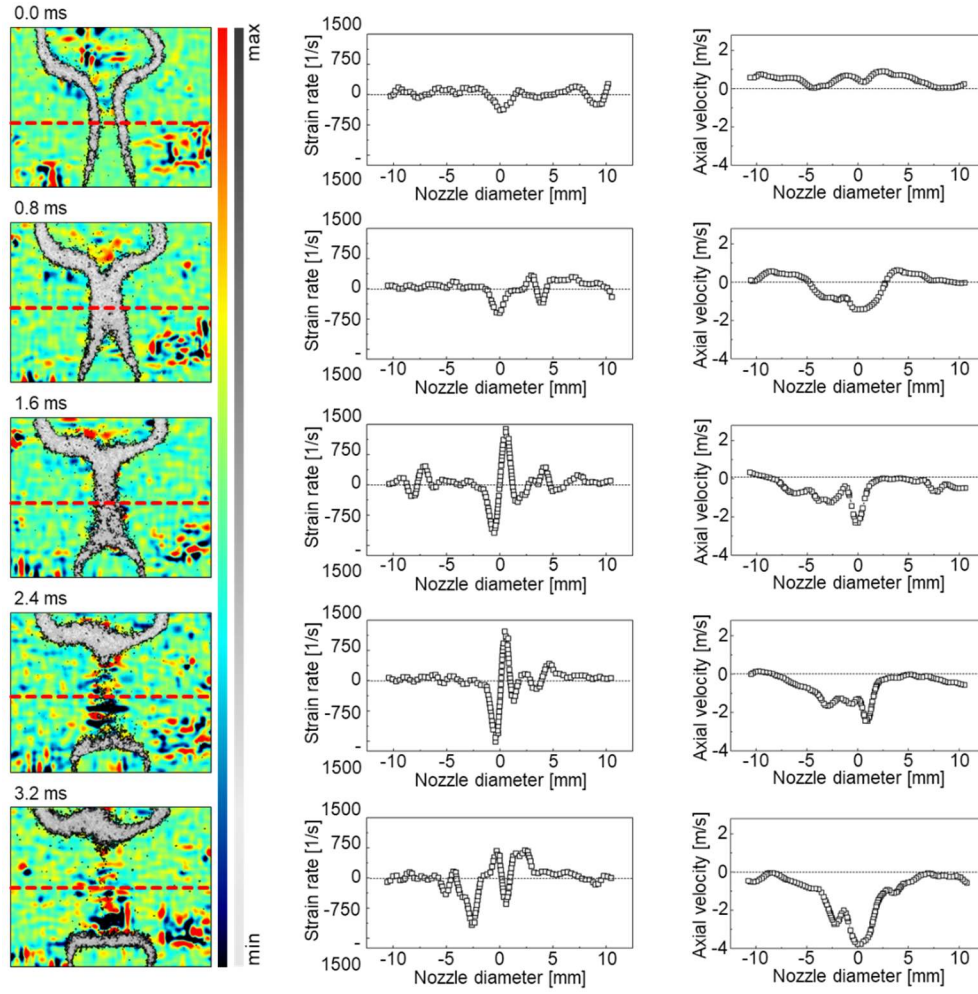


Fig. 4.12 Time-dependent data of pinch-off flame. Left: OH PLIF image & strain rate field, center: strain rate, right: axial velocity.

The pinch-off was then examined from a more fundamental viewpoint by calculating the strain rate $K = \frac{1}{2} \left(\frac{\partial u}{\partial y} + \frac{\partial v}{\partial x} \right)$ [50,52], which causes deformation of the flame structure and an axial velocity due to the reverse flow. Although previous studies [33] analyzed the correlation between the local flame extinction and a high strain rate, to understand the relationship between the strain rate and pinch-off, we herein calculated the strain rate in the region where the flame became separated. Figure 4.12 is the result of simultaneous measurements of OH PLIF and PIV at a repetition rate of 2,500 Hz, where the time interval between data points is

0.8 ms. Images on the left side of the figure consist of overlapping strain rate field (in color) and the OH PLIF image (in grayscale). The central plots display the strain rates [$1/s$], while plots on the right side show the axial velocity [m/s] measured at the red line indicated in the corresponding image on the left. At 0.0 ms, the flame is not pinched-off; and no significant features were observed in the flame deformation, the behavior of the flame columns, or the strain rate. Even at 0.8 ms, when two flame columns are deformed into a single flame throat, the strain rate fluctuates but does not take on a large value. However, the strain rate reaches a maximum value (1500 s^{-1}) at 1.6 ms, at which point the flame columns begin to form a single throat prior to their perfect separation. The strain rate gradually decreases after 2.4 ms when the flame is completely separated, but a remaining large strain rate (1300 s^{-1}) continuously affects the vicinity of the flame. Kim et al. [30] suggested that local flame extinction occurs at excessively high strain rates in non-premixed flames. In addition, Law et al. [125] reported an extinction stretch rate of 1800 s^{-1} under CH_4 /air conditions, while Katta et al. [126] suggested a strain rate of 1700 s^{-1} under H_2 /air conditions. Furthermore, Jarpala et al. [127] observed that the non-premixed swirl flame strain rate was 1200 s^{-1} under methane/air conditions, and Wang et al. [128] confirmed an extinction strain rate of 600 s^{-1} under a laminar flame of syngas-methane blends. In this study, the strain rate at the occurrence of local extinction in CH_4/H_2 mixture was measured, and flame separation was confirmed at $1300\text{--}1500\text{ s}^{-1}$. This range is comparable to the strain rates suggested by the other studies. The separation of the flame throat is caused by the high strain rate.

Reverse flow analysis was performed indirectly through the dynamic characteristics of the OH PLIF images in Fig. 4.6. The dipole vortex structure and reverse flow characteristics under flow oscillation in nonreacting flow were analyzed through Fig. 4.10. In addition, simultaneous measurement of OH PLIF/PIV confirmed the interaction of vortex-reverse flow in the reacting flow, as shown in Fig. 4.11. Overall, the reverse flow in pinch-off was confirmed and studied from various perspectives. For a more quantitative analysis, the axial velocity was calculated along the red dotted lines in the left figures of Fig. 4.12. Depending on the periodicity, the measured velocity was positive in the phase with elongated flame, and negative when the flame was pinched off. Therefore, at 0.0 ms the velocity changed from positive to negative, and afterwards the axial velocity was negative due to the reverse flow effect. Concurrent to the flame throat at 0.8–1.6 ms, a negative velocity due to reverse flow also appeared and exerted its effect up to 3.2 ms when the flame was separated. As a result,

the reverse flow affected the pinch-off flame and played an important role in main flame formation, while air entrainment by the vortical structure is critical in pocket flame formation.

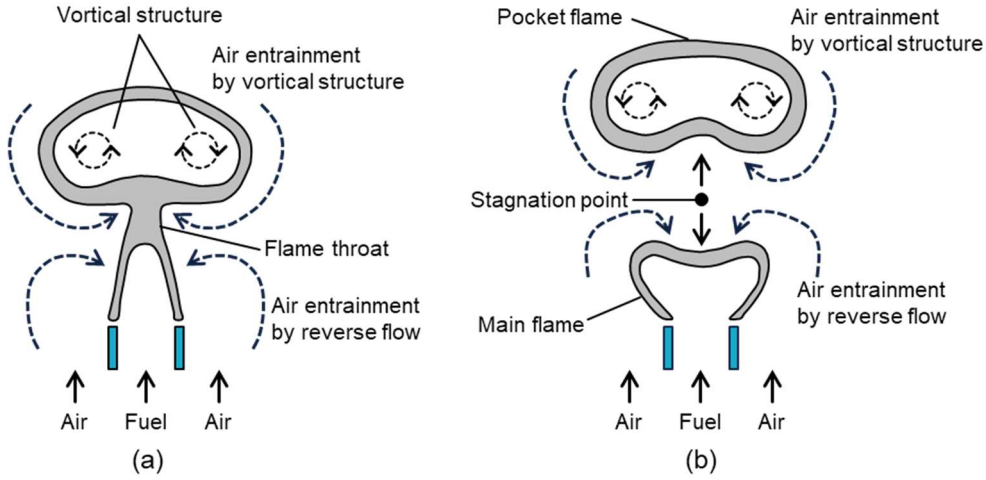


Fig. 4.13 Schematic flow patterns of pinch-off flame. Images (a) and (b) illustrate the cases of Fig. 4.11(e) and (f), respectively.

Pinch-off occurs when the following two situations are simultaneously satisfied to cut the flame: air entrainment by vortex flow and flame deformation by interaction between entrainment and the suction from reverse flow. The corresponding flow patterns are depicted in Fig. 4.13. Figure 4.13(a) shows the flame throat just before pinch-off for case (e) in Fig. 4.11. The rotating vortical structure created inside the flame affected the air flow that was supplied coaxially, and the air was entrained to the center line where the fuel was located to form the flame throat. At the same time, there was entrainment of surrounding air due to reverse flow at the bottom of the flame, which also causes air to flow into the fuel area. An inflow of air was confirmed to occur at the same time, causing a flame throat to form. Figure 4.13(b) shows the case with the pocket flame separated from the main flame, and the flow pattern under acoustic excitation indicates the interaction of entrained air flow by the vortical structure and reverse flow near the stagnation point [111], which exists between $1*D$ and $2*D$. The entrainment of surrounding air by the reverse flow was in the negative axial direction, and the entrainment of surrounding air by the vortical structure was in the positive axial direction. The pinch-off flame has confirmed the interaction of the two flows in different

directions. The occurrence of pinch-off requires simultaneous existence of vortical structure and air entrainment by reverse flow. These flows act around the stagnation point with different roles. Air entrainment by the vortical structure affects the pocket flame generation, and air entrainment by reverse flow has a dominant effect on the shape of the main flame. In conclusion, it was confirmed that the pinch-off is correlated with these two flows.

CHAPTER 5

NOX EMISSION CHARACTERISTICS OF PINCH-OFF FLAME UNDER ACOUSTIC EXCITATION

5.1 Objectives

As air pollution becomes an increasingly important environmental problem owing to increased greenhouse gas emissions, emission regulations are becoming stricter. Accordingly, in various manufacturing areas, such as the aircraft industry [129–132], power plants [133–135] and the shipping [136–138] and automobile industries [139–141], efforts are being made to reduce the exhaust emissions of combustion systems by using hydrogen (H_2) as the fuel, as it does not emit carbon. As part of these efforts, the twin annular premixing swirler (TAPS) combustor [1,98] has been developed for use in aviation gas turbines. This combustor uses a mixer that is based on a premixed flame as the main flame and a non-premixed flame as the pilot flame. This is to both ensure flame stability and reduce emissions. Li et al. [11,99] studied the interactions between the pilot flame and a V-shaped main flame under acoustic excitation conditions. An analysis of the dynamic flame structure was performed for the two flames under acoustic excitation; the results obtained using an analytical model were in agreement with those of experimental measurements. It was confirmed that the dynamic pilot flame–main flame interactions are amplified by the vortex formed under certain acoustic excitation conditions. In addition, it was suggested that the primary effect of the excitation conditions on the total flame response is the related to the dynamics of the pilot flame and the effect of the velocity field of the burned side. Therefore, it is important to study the flame dynamics of non-premixed flames, as they have a determining effect on flame stability in TAPS combustors.

In the case of non-premixed flames, fuel/air mixing is enhanced by acoustic excitation, which affects the flame height and NO_x emissions. Odelabroy et al. [142] studied the NO_x emission characteristics of a non-premixed liquid-fueled burner under external pulsations. They observed a 15% reduction in the NO_x emissions at a specific frequency. The mixing effect is the most important factor for reducing the NO_x emissions, and it was confirmed that mixing by pulsation shortens the flame height. Therefore, the flame height and flame

residence time (τ_{res}) are correlated, and the NO_x emissions are reduced owing to the lowering of the maximum temperature. Chao et al. [143] reported that low-frequency flame flickering and the use of coaxial air are effective in reducing the NO_x emissions of laminar non-premixed flames. In addition, by using the expression for the EINO_x scaling of turbulent non-premixed flames with laminar non-premixed flames, it was confirmed that the two types of flames exhibit different characteristics. Hence, an EINO_x equation suitable for laminar flames was proposed. Oh et al. [143] confirmed that the height of non-premixed flames is reduced by acoustic excitation and reported that the flame height and NO_x emissions were reduced at the resonant frequency. This is because the flame temperature is lowered as the degree of fuel/air mixing is increased by acoustic forcing, resulting in a reduction in the NO_x emissions. Kim et al. [107] confirmed the effects of changes in the flame structure and reported a decrease in the NO_x concentration at the resonant frequency. In addition, they also confirmed that the increase in the flame surface area because of acoustic excitation increases the degree of air entrainment, resulting in a decrease in the flame height and NO_x emissions. Several studies on the reduction of the NO_x emissions of non-premixed flames have suggested that increasing the intensity of acoustic excitation increases the degree of fuel/air mixing, which, in turn, reduces the flame height and NO_x emissions. Therefore, in this study, we analyzed the correlation between the intensity of acoustic excitation and NO_x emissions.

A pinch-off flame is a flame that gets separated when subjected to acoustic excitation (i.e., to certain forcing frequency and amplitude conditions). It is a pocket hot product that is separated from the main flame, which remains attached to the nozzle tip. To analyze the pinch-off phenomenon, Carpio et al. [144] and Tyagi et al. [49] performed numerical and analytical studies. Ahn et al. [104] mapped the increasing forcing frequency and amplitude to determine when pinch-off occurred in a Burke–Schumann flame, which is one type of non-premixed flame [53], and elucidated the pinch-off mechanism by simultaneous OH planar laser induced fluorescence and particle image velocimetry measurements. The pinch-off phenomenon affects not only the combustion stability but also the exhaust emissions. Shaddix et al. [43] reported a pinch-off phenomenon wherein the tip of the flame was separated from a non-premixed flame. They also reported that the soot growth level was higher by a factor of four or more compared with that for a steady flame. The residence time has been used as a parameter to determine the soot volume fraction, and it was reported that the flame residence time (τ_{res}) increases with the flame tip size and that soot production

increases at higher temperatures. These results were confirmed through experimental measurements and computational studies [44].

In this study, an exhaust emission analysis of the pinch-off flame, which is a special flame structure in which the flame is separated, was performed. While there have been several studies on soot formation in pinch-off flames, the NO_x and CO emissions of these flames have not been studied extensively. Therefore, OH^* chemiluminescence measurements were performed to analyze the effects of acoustic excitation on the flame structure, and the structure of the pinch-off flame was analyzed to determine parameters such as the flame residence time (τ_{res}) and EINO_x .

5.2 Experimental setup and methodology

A schematic diagram of the experimental apparatus used in this study is shown in Fig. 5.1. Figure 5.1(a) shows the experimental device used for the non-premixed flame; the fuel was supplied from the central nozzle (inner nozzle diameter = 5 mm), and the oxidizer was supplied from the coaxial air nozzle (inner nozzle diameter = 50 mm). Loudspeakers for acoustic excitation were installed in the air and fuel supply lines, and perturbations were delivered, simultaneously, through the supply lines via the loudspeakers. Bulk velocity and loudspeaker acoustic data were acquired by installing hot wire anemometers (HWAs) 30 mm from the tips of the fuel and air nozzles. The OH* chemiluminescence measurements were performed using a high-speed camera capable of measuring at 7,000 Hz at a maximum resolution of 1028×1028 to analyze the changes in the flame structure in response to the acoustic excitation. A high-speed camera (HighSpeedStar 8, maximum resolution of 1024×1024 at 7 kHz) equipped with an intensifier (HighSpeed IRO) to amplify the OH signal intensity, a Nikon UV 100 mm f/2.8 lens, and an OH band pass filter (LaVision, VZ-image Filter LIF for OH, enhanced, 310 ± 25 nm) were used for imaging during the measurements. The exposure time was 0.32 ms, and the field of view was 35×90 mm, as shown in Fig. 5.1.

The exhaust gases such as NO_x , CO, and O_2 were measured using a TESTO 350 K gas analyzer. The stainless-steel sampling probe was positioned at a location more than 10 times higher than the flame height [145]. This location was downstream and at the point where chemical equilibrium was reached. The gas analyzer was calibrated using 99.99% nitrogen, and sampling was performed once per second. The average data measured for 2 min were used.

The exhaust gas concentration was converted to a 15% O_2 composition using the following equation [146]:

$$\text{ppm}_{\text{corr}} @ 15 \text{ O}_2 = \text{ppm}_{\text{meas}} \left[\frac{20.95 - \text{O}_{2,\text{basis}}}{20.95 - \text{O}_{2,\text{meas}}} \right] \quad (5-1)$$

where $\text{ppm}_{\text{corr}} @ 15 \text{ O}_2$ is 15% O_2 (standard O_2 basis) converted into pollutant emission concentration (ppmv), ppm_{meas} is measured pollutant emission concentration (ppmv), $\text{O}_{2,\text{meas}}$ is the measured O_2 concentration (vol%, dry basis), and $\text{O}_{2,\text{basis}}$ is the standard O_2 basis (Vol%, dry basis; Eq. (5-1) assumes that standard air is 20.95% O_2 by volume).

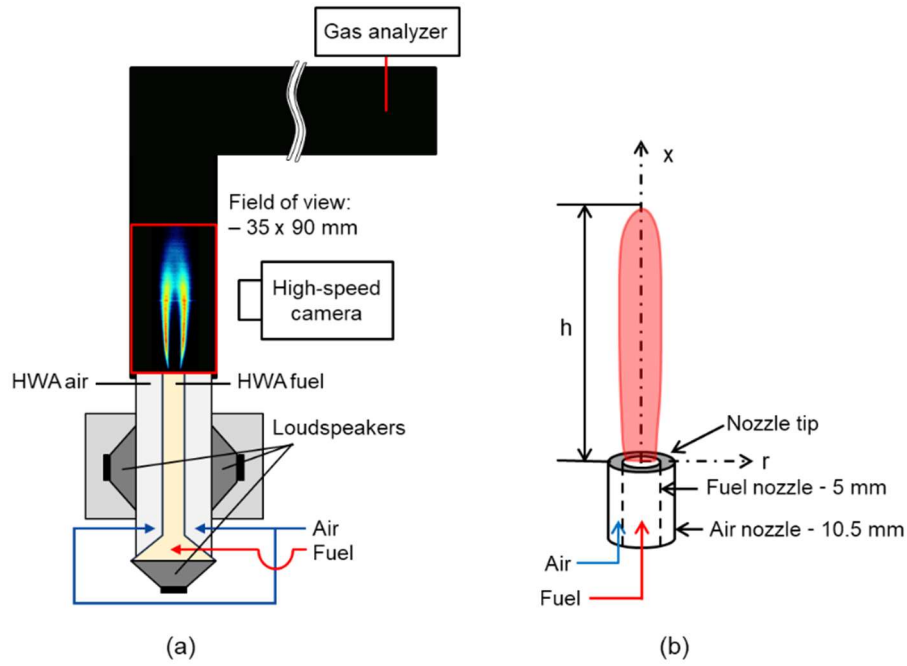


Fig. 5.1 (a) Schematic diagram of experimental setup used and (b) shape of fuel/air nozzle.

The experimental conditions used are listed in Table 5.1. The fuel used consisted of methane (CH_4) and hydrogen (H_2), which were mixed in a volume ratio of 25%/75%, and air was used as the oxidizing agent. The fuel and air bulk velocity was 1 m/s under the same Burke–Schumann flame [121]. The fuel and air nozzles were excited simultaneously, and the frequency was increased in increments of 20 Hz over the range of 0–300 Hz. The velocity perturbation intensity (u'/\bar{u}), which is the ratio of the velocity perturbation (u') to the average velocity (\bar{u}), was used to control the magnitude of perturbation of the flow; it was increased in intervals of 5% over the range of 5–50%. The magnitude of the velocity perturbation was determined using the software LabVIEW and the HWAs attached near the fuel and air nozzles. The acquired signals were adjusted using a function generator (Yokogawa, FG400), and the measurements were performed when the phase difference between the two signals (acoustic data for the fuel and air) was less than 5° .

Table 5.1. Experimental conditions

Parameter	Value
Fuel composition [%Vol]	H ₂ /CH ₄ - 25/75
Oxidizer	Air
Fuel & air bulk velocity [m/s]	1
Forcing frequency [Hz]	0–300 (20 Hz steps)
Velocity perturbation intensity (u'/\bar{u})	0–50% (5% steps)
Adiabatic flame temperature	2380 K

Figure 5.2 shows a unique non-premixed flame structure called a pinch-off flame, which occurs under acoustic conditions of 80 Hz and $u'/\bar{u} = 50\%$. In this study, the structure of the pinch-off flame was used to analyze the correlation between the flame height and the NO_x emission characteristics. Therefore, the flame attached to the nozzle tip was defined as the main flame (F_M), and the separated flame was defined as the pocket flame (F_P). The height of the F_M was defined as that from the tip of the nozzle to the tip of the main flame. The height of the F_P was defined as the height of the detached hot product. The height from the nozzle tip to the top of the pocket flame was defined as the total flame height with a pocket (F_T). While analyzing the correlation between the flame height and the NO_x emissions, the F_T flame, including the space between the main flame and the pocket flame, was not considered. Because NO_x is formed in high-temperature flames, it was assumed that the empty space between the main flame and the pocket flame does not have a significant effect on NO_x formation. Therefore, in this study, for the investigated forcing frequency range for pinch-off flames, the net hot product (F_N) excluding the space between the F_M and F_P flames was defined and used to analyze the correlation between the flame height and the NO_x emissions. Figure 5.2(b) shows an image that defines the F_N flame. While defining the F_N flame, the phase with the maximum flame height was selected. In addition, the nonpinch-off flame, that is, the flame that was not separated, was also included in the F_N flame.

The OH group is used widely as a flame marker owing to its advantages such as its high signal intensity. However, the OH region cannot directly represent the flame surface because OH is distributed over a wide area, that is, not only in the reaction zone but also in the high-temperature products. Accordingly, several researchers [7,102] have proposed methods for

representing the OH region as the flame surface or front. In this study, the flame surface was defined by adopting a method from one of the aforementioned studies. The OH region was distinguished based on the gradient of the acquired OH* chemiluminescence image, and the outermost contour was approximated using the stoichiometry contour, which was defined as the flame surface. The approximate stoichiometry contour locations are shown in Fig. 5.2.

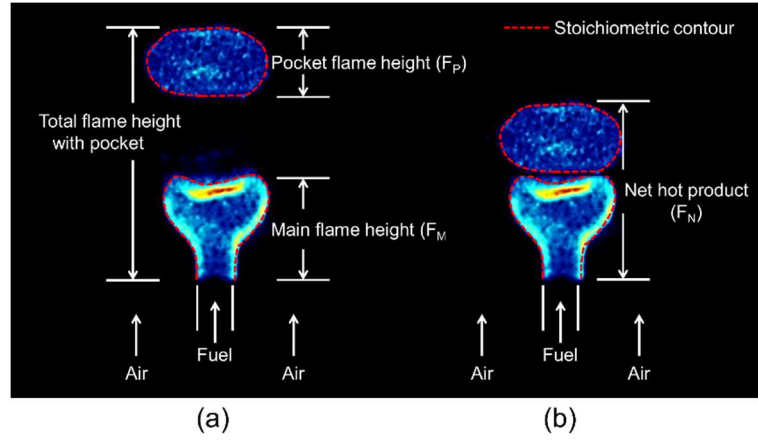


Fig. 5.2 (a) Defining flame height based on main flame and pocket flame of pinch-off flame.
 (b) Example of image showing net hot product (F_N) excluding space between main flame (F_M) and pocket flame (F_P).

5.3 Global appearance characteristics of non-premixed flame under acoustic excitation

Figure 5.3 shows the results of an experiment wherein different forcing frequencies were used to acoustically excite the flame when the velocity perturbation intensity (u'/\bar{u}) was 30%. This was done with the aim of analyzing the height and structural characteristics of the flame. The images shown are the averages of 500 images obtained during the OH* chemiluminescence measurements for flame visualization. The overall flame height characteristics were as follows: the excitation frequency range of 20–200 Hz resulted in a lower flame height compared with that at 0 Hz (i.e., without excitation). In addition, the flame height increased at frequencies higher than 240 Hz. It has been reported that the flame height is determined by the excitation frequency and u'/\bar{u} [147]. In addition, for non-premixed flames, as the fuel/air mixing intensity is increased, the flame height decreases. Figure 5.3 shows that the fuel/air mixing intensity reduced with an increase in the forcing frequency for a constant u'/\bar{u} . As a result, the flame height also increased [37,111]. Specifically, the flame height increased starting at forcing frequencies of 120 Hz and higher, reaching a height greater than 0 Hz from 280 Hz and on.

At 0 Hz (i.e., without excitation), a relatively large and wide OH* region was observed at the nozzle and the end of the flame. It is known that the OH signal intensity is proportional to the amount of heat released [148,149]. A high-intensity OH* signal (red dashed box) was observed at the end of the flame, even at 240 and 280 Hz. At 20 Hz, a high-intensity OH* signal was observed at the middle of the flame, probably owing to the compression of the flame by the acoustic excitation. A detailed analysis of this phenomenon is shown in Fig. 5.8(a). In conclusion, it was confirmed that the amount of heat released was higher at the forcing frequencies of 0, 240, and 280 Hz than at the other forcing frequencies; this was true both for the flame end and the middle of the flame at 20 Hz. This, in turn, resulted in increased NO_x emissions at these frequencies.

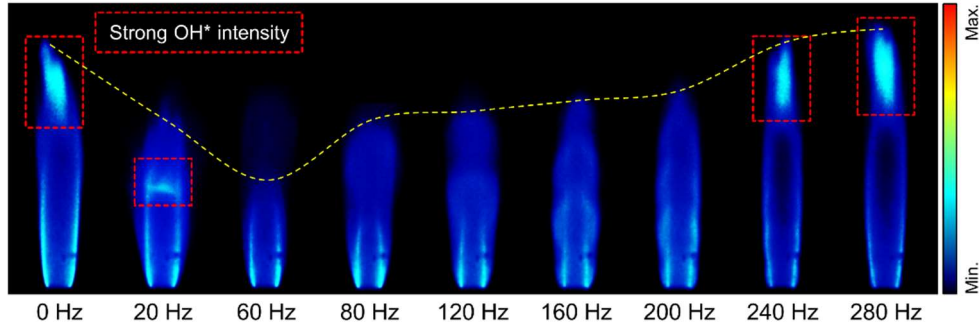


Fig. 5.3 Averaged images of OH* chemiluminescence at different frequencies and $u'/\bar{u} = 30\%$.

As shown in Fig. 5.4, three excitation frequencies (20, 80, and 280 Hz) were used to confirm the trend in flame height with respect to increases in u'/\bar{u} . We selected these three frequencies based on the results of pinch-off mapping performed in previous studies [51,104]; the three forcing frequencies represent the flickering, pinch-off, and wrinkled flame regions, respectively. For all three excitation frequencies, the flame height tended to decrease with increasing u'/\bar{u} . This trend is highlighted with a red dashed line along the flame tip. This result can be ascribed to the fact that the vortex generated by the acoustic excitation gets closer to the nozzle tip as u'/\bar{u} is increased, resulting in an increase in the degree of mixing of the fuel/air mixture [147].

Figure 5.4(a) shows that the changes in the flame height were not large up to u'/\bar{u} values of 20%. However, the flame height decreased rapidly from $u'/\bar{u} = 30\%$ onward. This trend is also shown in Fig. 5.4(b). However, in Fig. 5.4(c), the trend in the flame height as u'/\bar{u} is increased is different. Specifically, the decrease in the flame height is gradual up to $u'/\bar{u} = 30\%$. It then decreases sharply from $u'/\bar{u} = 40\%$ onward. In addition, a wrinkled flame was observed at $u'/\bar{u} = 50\%$. In Fig. 5.4(c), the flame height decreases gradually because the flame response to the acoustic excitation results in a low-pass filter effect, and the low fuel/air mixing intensity leads to a gradual decrease in the flame height. In addition, at a high forcing frequency (240 Hz and higher), a similar trend was observed (see Fig. 5.4(c)). Thus, the correlation between the flame height and the forcing frequency decreased with the increase in u'/\bar{u} . In addition, it was confirmed that the decrease in the flame height is gradual at high forcing frequencies.

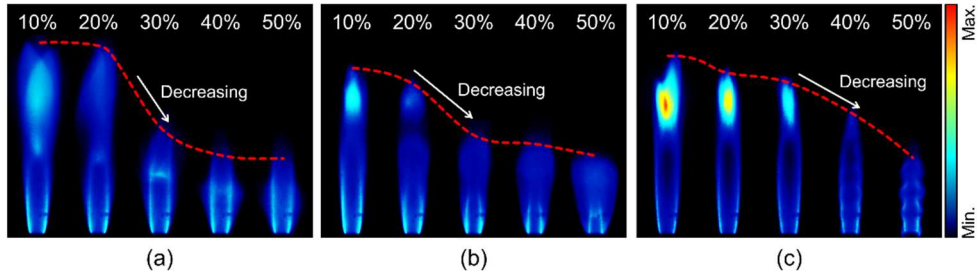


Fig. 5.4 Averaged flame images for different u'/\bar{u} values and forcing frequencies of: (a) 20, (b) 80, and (c) 280 Hz.

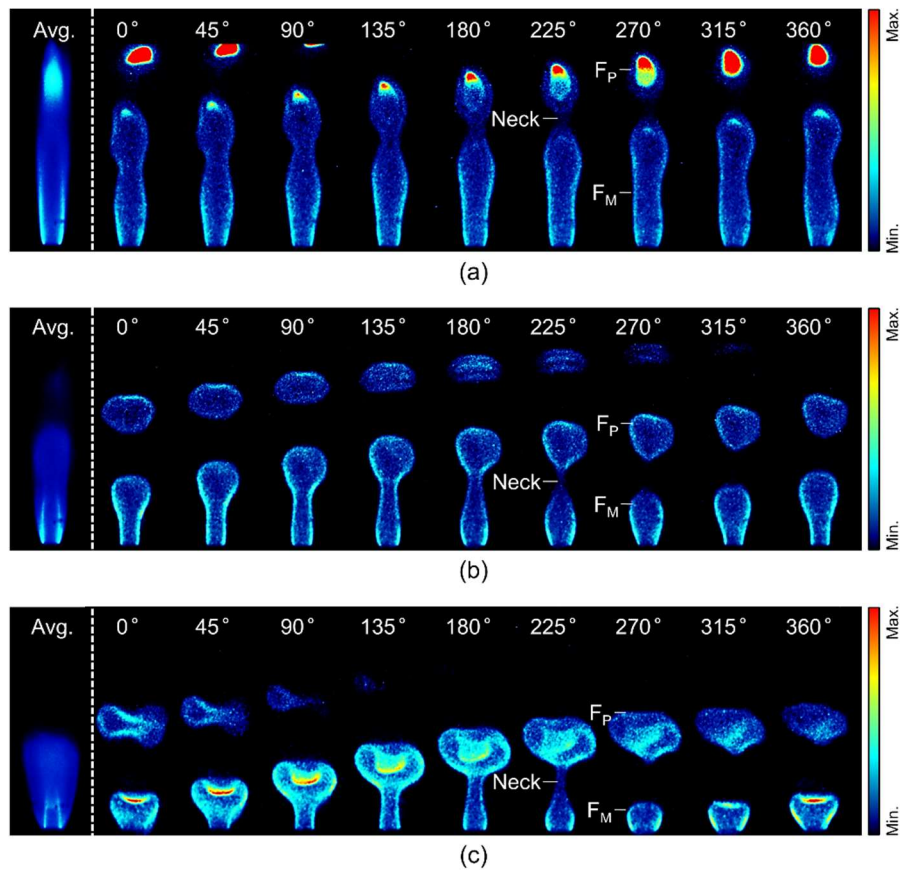


Fig. 5.5 Instantaneous flame images at 80 Hz and u'/\bar{u} values of (a) 10%, (b) 30%, and (c) 50%.

Figure 5.5 shows instantaneous images of the flame in Fig. 5.4 (b) at 80 Hz to highlight

the flame deformation process at a specific acoustic excitation frequency. At 80 Hz, the pinch-off phenomenon, wherein the flame is separated, is observed. The underlying mechanism for this phenomenon, which depends on the forcing frequency and u'/\bar{u} , has been suggested in a previous study [104]. The flame separation process can be described as follows. At 225° (see Fig. 5.5), the flame neck becomes narrow, and at 270° , the flame gets divided into the main flame (F_M) and the pocket flame (F_P) and is pinched off. We had previously analyzed the location where the flame gets divided [104] and had found that this location moves closer to the nozzle tip (upstream) as u'/\bar{u} is increased. At $u'/\bar{u} = 10\%$, pinch-off occurs at the top of the flame while at $u'/\bar{u} = 50\%$, it occurs near the nozzle tip, that is, near the lower part of the flame. This is because the vortex generated by the acoustic excitation moves closer to the nozzle tip (i.e., upstream) [147] as u'/\bar{u} is increased. Therefore, the position of the pinch-off, that is, the position where the flame is cut (see Fig. 5.5) moves closer to the nozzle tip as u'/\bar{u} is increased.

The changes in the position of the pinch-off with increases in u'/\bar{u} can be described as follows: at $u'/\bar{u} = 10\%$, pinch-off occurs but it does not significantly affect the flame behavior. However, at $u'/\bar{u} = 30\%$, the flame neck becomes prominent, and a circular F_P flame is observed. Moreover, even at $u'/\bar{u} = 50\%$, the flame neck is prominent, and the F_P flame is compressed in the vertical direction. The changes in the shape of the F_P flame are caused by the forward and backward flow in the vertical direction because of the acoustic excitation [104] while the flame is compressed by the flow in the backward direction.

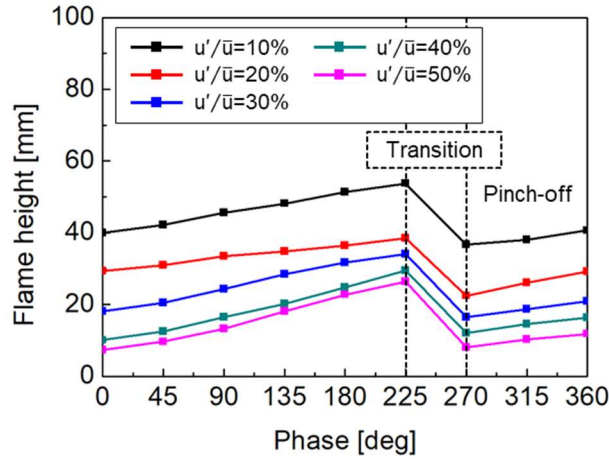


Fig. 5.6 Changes in height of main flame (F_M) with phase for u'/\bar{u} values of 10–50% and

forcing frequency of 80 Hz.

Figure 5.6 shows the flame height for the u'/\bar{u} values given in Fig. 5.5; these are shown to allow for a comparison of the differences in the heights of the nonpinch-off and pinch-off flames. Only the F_M flame attached to the nozzle tip was considered. After obtaining the OH* chemiluminescence images, the average image corresponding to each phase was used, and the flame height was calculated by setting the threshold value to 80% of the maximum intensity to distinguish the reaction zone [104].

The overall flame height tends to decrease as u'/\bar{u} is increased. In addition, the maximum flame height was observed at 225° and the minimum flame height at 270°. Pinch-off occurs over the phase range of 225–270°. At 225°, which is the phase just before pinch-off, the flame neck is the narrowest, and at 270°, the flame height decreases sharply owing to pinch-off. Thus, it was confirmed that the flame height decreases as u'/\bar{u} is increased.

The effects of acoustic excitation on the flame height must be analyzed from various perspectives. Figure 5.3 confirmed that the flame height changes with the excitation frequency. Similarly, Fig. 5.4 confirmed that the flame height decreases as u'/\bar{u} is increased while Fig. 5.5 confirmed that the pinch-off phenomenon occurs as u'/\bar{u} is increased when the forcing frequency is 80 Hz. It is known that the NO_x emissions vary with the flame height and temperature. Therefore, it is necessary to confirm the effects of the dynamic characteristics of the flame on the NO_x emissions during the acoustic excitation of non-premixed flames. In this study, because the fuel and air flow rates were kept constant, the adiabatic flame temperature was constant ($T_{ad} = 2380$ K), and the changes in the flame height in response to acoustic excitation were analyzed as a characteristic affecting the NO_x emissions.

5.4 Effects of acoustic excitation on EINO_x and CO concentration

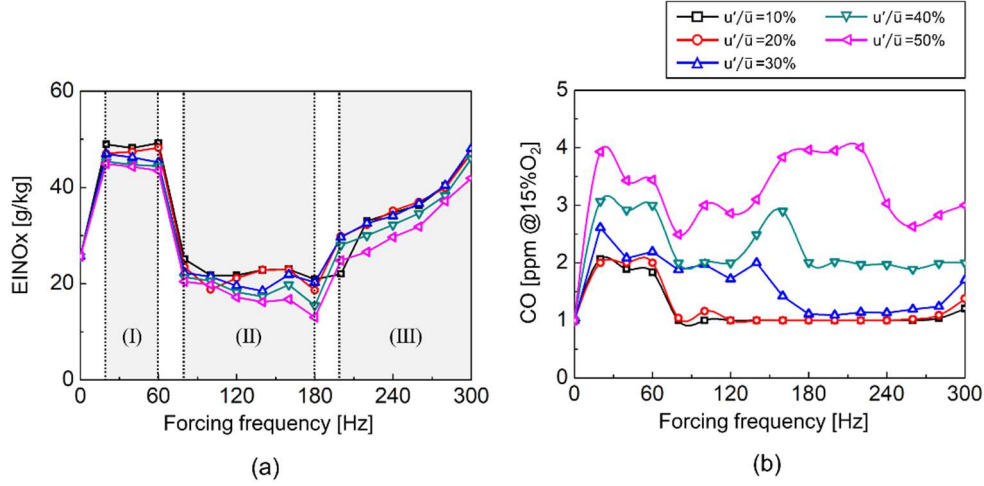


Fig. 5.7 Changes in EINO_x and CO concentration with forcing frequency for different u'/\bar{u} values: (a) EINO_x and (b) CO concentration (at 15% O₂).

Figure 5.7 shows the effects of the excitation frequency on EINO_x [30,37,72] and the CO concentration for different u'/\bar{u} values. First, we discuss the changes in EINO_x. As can be seen from Fig. 5.7(a), EINO_x decreases overall with an increase in u'/\bar{u} . It was confirmed from Fig. 5.4 that the flame height decreased with an increase in u'/\bar{u} at the three investigated frequencies while Fig. 5.6 confirmed that the flame height decreased with an increase in u'/\bar{u} at 80 Hz. A similar trend was observed in the case of EINO_x as well. As the flame height increases, the flame residence time increase as well and so do the NO_x emissions. Thus, it was confirmed that the flame height decreases as u'/\bar{u} is increased and so does EINO_x.

The curve showing the effects of the forcing frequency on EINO_x can be divided into three regions (Regions I–III). Region (I) corresponds to a forcing frequency range of 20–60 Hz, in which the emissions are higher compared with those at 0 Hz. In this range, the curve is flat, and EINO_x is approximately 45–50. Region (II) corresponds to a forcing frequency range of 80–180 Hz, and the emissions are equal to or less than those at 0 Hz. The last region, that is, Region (III), corresponds to 200–300 Hz, and EINO_x increases from 200 Hz onward. Thus, the forcing frequency has a different effect on the dynamic behavior of the flame in each

region [104]. Region (I) corresponds to a flickering flame with large fluctuations in the vertical direction. However, this is a nonpinch-off flame. In contrast, Region (II) corresponds to a pinch-off flame. Finally, Region (III) is a high-forcing-frequency region, wherein the flame response is weakened, and wrinkles are observed on the flame surface.

Figure 5.7(b) shows the effects of the forcing frequency and u'/\bar{u} on the CO concentration. Overall, the trend is opposite to that for EINO_x , with the CO concentration increasing with u'/\bar{u} . For the forcing frequency range of 20–60 Hz, the CO concentration is high, and the trend is similar to that in Region (I) in Fig. 5.7(a). The flame behavior in Region (I) was characterized by large fluctuations in the vertical direction. Because of this behavior, Region (I) of Fig. 5.7(a) and the 20–60 Hz range in Fig. 5.7(b) show similar trends. In the forcing frequency range of 80–300 Hz, for u'/\bar{u} values of 10% and 20%, the CO concentration is similar to that at 0 Hz without acoustic excitation. In addition, the CO concentration was almost insignificant at these values. Even at $u'/\bar{u} = 30\%$, the CO emission was insignificant in the 180–280 Hz range. However, when u'/\bar{u} was increased beyond 40%, the CO emission increased. This is because complete combustion does not occur at higher u'/\bar{u} values.

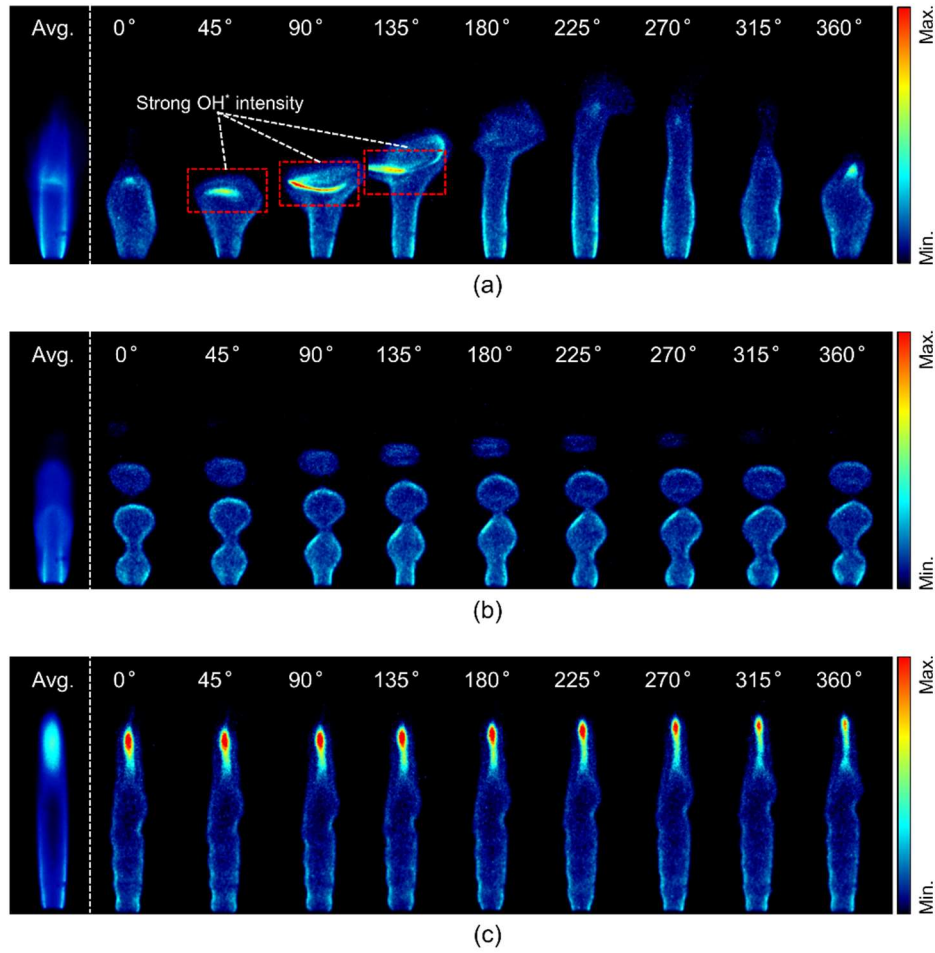


Fig. 5.8 Changes in instantaneous flame image with phase at $u'/\bar{u} = 30\%$ and frequencies of (a) 20, (b) 140, and (c) 260 Hz.

Figure 5.8 shows the flame dynamic behavior at three frequencies (20, 140, and 260 Hz), which represent Regions (I)–(III), respectively, of Fig. 5.7(a). The images were obtained to determine the correlation between $EINO_x$ and the acoustic excitation frequency. In Fig. 5.8 (a), at 20 Hz, a flame with large fluctuations in the vertical direction was observe; this is correlated to the large $EINO_x$ value of Region (I) in Fig. 5.7(a). During the transitory process in which the compressed flame is stretched by acoustic excitation at 45-130°, a high-intensity OH^* region is formed at the flame tip, and a large amount of heat is dissipated in the area marked by the red dashed box (Fig. 5.7(a)). Therefore, at 20 Hz, the NO_x emissions from the

flame tip increase owing to the effect of the acoustic excitation. Figure 5.8(b) shows the trend in $EINO_x$ in Region (II) at 140 Hz. The $EINO_x$ values in Region (II) are the same or smaller than those at 0 Hz, and the difference between F_M and F_P can be seen clearly because of the pinch-off phenomenon, owing to which the flame is separated into different components. Moreover, compared with the $EINO_x$ values for the other forcing frequency frequencies, those in Region (II) of Fig. 5.7(a) are low and so is the flame height.

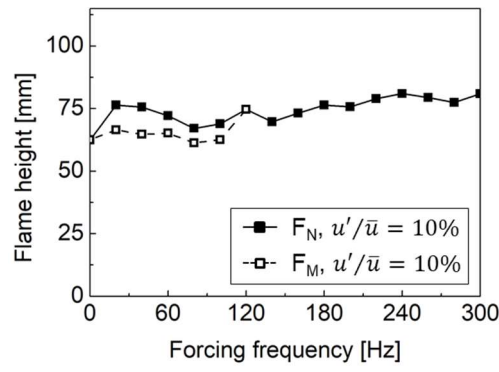
Figure 5.8(c) shows the flame behavior at 260 Hz and the corresponding forcing frequency is well represented by Region (III) in Fig. 5.7(c). Region (III) is the region where the flame response decreased with an increase in the forcing frequency. This can be confirmed from the corresponding image, which shows that the flame was phase-dependent. Only weak fluctuations were observed on the flame surface, and no significant changes were observed in the flame height and structure. However, a high-intensity OH^* region was observed at the flame tip; this was in keeping with the OH^* image for frequencies higher than 240 Hz in Fig. 5.3. In the high-forcing-frequency range, a high-intensity OH^* region is formed at the flame tip with increasing frequency, resulting in increased NO_x emissions. This is in keeping with the increase in $EINO_x$ with increases in the excitation frequency (see Region (III) in Fig. 5.7(a)).

5.5 Effects of velocity perturbation intensity (u'/\bar{u}) and forcing frequency on main flame (F_M) and net hot product (F_N)

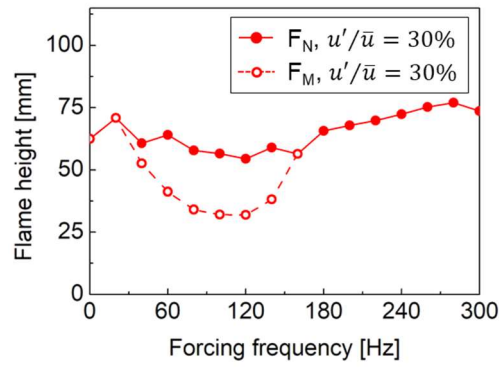
Figure 5.9 shows the effects of the forcing frequency and u'/\bar{u} on the flame heights (i.e., those of F_M , F_T , and F_P) as defined based on the pinch-off flame in Fig. 5.2. Based on the phase, the average of the OH* images was obtained, and the flame heights were calculated. The dashed line represents F_M (the flame attached to the nozzle) while the solid line represents F_N . The sum of F_M and F_P is defined in Fig. 5.2(b). It can be seen from Fig. 5.6 that the flame height decreased with the increase in u'/\bar{u} at 80 Hz. However, a comparative analysis of the F_M and F_N heights was not performed. Therefore, Fig. 5.9 shows the changes in the flame height with increases in u'/\bar{u} and the forcing frequency.

The curve for the flame height as a function of the forcing frequency decreases as u'/\bar{u} is increased from 10% to 50%. When $u'/\bar{u} = 10\%$ (see Fig. 5.9(a)), the flame height is slightly higher than that at 0 Hz (i.e., without excitation), and the pinch-off phenomenon occurs. In addition, the observed height distance between the F_M and F_N flames is small except at velocity perturbation intensities of 30% to 50%, where the difference is large.

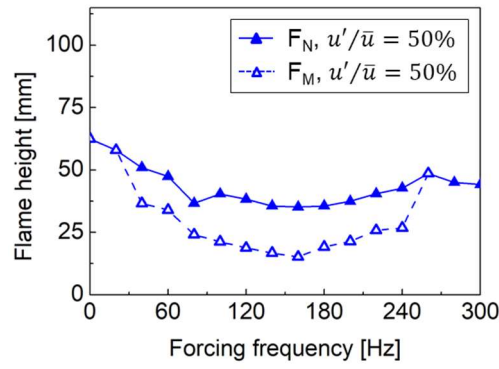
In Fig. 5.9(b), for $u'/\bar{u} = 30\%$, the trend in the flame height is different over the investigated range of forcing frequencies. The F_N flame height in the forcing frequency range of 40-160 Hz was equal to or lower than that at 0 Hz and lower still for F_M . In addition, the gap between the F_M and F_N flames is larger than that in Fig. 5.9(a). In Fig. 5.9(c), at $u'/\bar{u} = 50\%$, pinch-off occurs over a wide forcing frequency range, and the flame heights at most of the frequencies are lower compared with those at 0 Hz. Finally, on comparing the F_M flames in Fig. 5.9, it is observed that the F_M flame in Fig. 5.9(c) exhibits the lowest height. Therefore, it was confirmed that increasing u'/\bar{u} reduces the heights of the F_N and F_M flames.



(a)



(b)



(c)

Fig. 5.9 Effects of velocity perturbation intensity (u'/\bar{u}) on flame heights (dotted line is flame height without acoustic excitation): (a) $u'/\bar{u} = 10\%$, (b) $u'/\bar{u} = 30\%$, and (c) $u'/\bar{u} = 50\%$.

5.6 Effects of Strouhal number and forcing frequency on flame residence time (τ_{res})

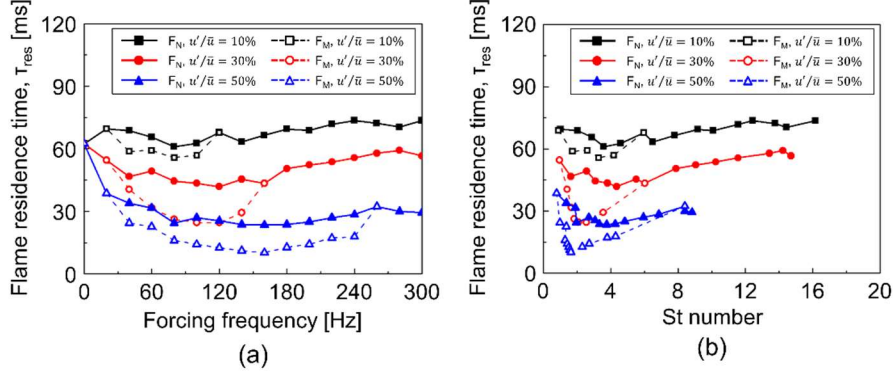
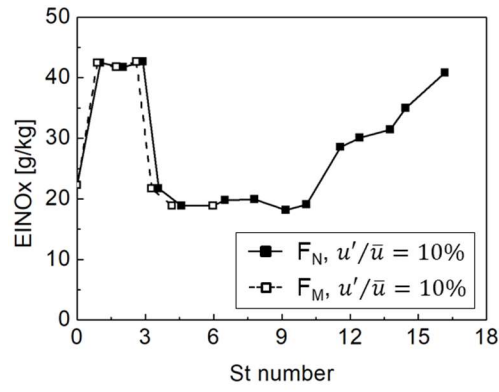


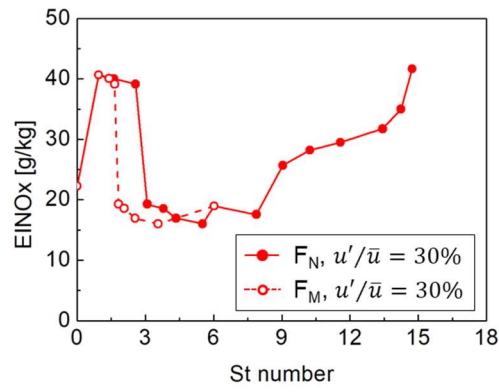
Fig. 5.10 Effects of (a) forcing frequency and (b) Strouhal (St) number on flame residence time (τ_{res}) at various u'/\bar{u} values.

Figure 5.10 shows effects of the forcing frequency and Strouhal number ($St = fL/u$, where f = forcing frequency, L = flame height, and u = mean velocity) on the flame residence time (τ_{res} , $\tau = L/u$, where L = flame height and u = mean velocity). For the analysis, the forcing frequency and St were calculated using the flame height data for the F_M and F_N flames in Fig. 5.9. In addition, the τ_{res} analysis was performed from two perspectives, that is, based on the F_N and F_M flames corresponding to the pinch-off flame. First, from the F_N perspective, the τ_{res} value at $u'/\bar{u} = 10\%$ is greater compared with that at 0 Hz while those at 30% and 50% are smaller. Therefore, τ_{res} decreases with increasing u'/\bar{u} . From the F_M point of view, τ_{res} decreases more than F_N . Thus, it was confirmed that τ_{res} decreases as u'/\bar{u} is increased. This trend is similar to that for $EINO_x$ shown in Fig. 5.7(a). However, there was no difference between Regions (I)–(III) of the forcing frequency, as shown in Fig. 5.7(a).

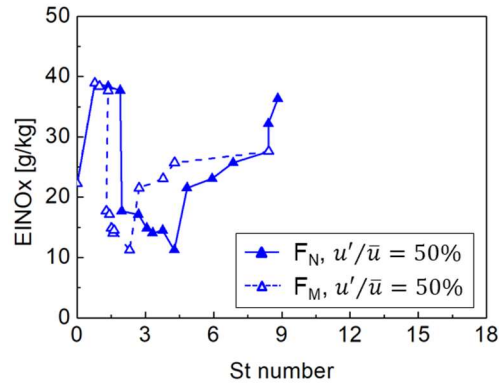
Figure 5.10(b) shows the St value results on τ_{res} at various u'/\bar{u} values. First, an analysis of the F_N perspective. As u'/\bar{u} increases, the τ_{res} and maximum St value of F_N decrease. The τ_{res} remains relatively constant as the St value increases at u'/\bar{u} of 10%, but the τ_{res} tends to increase slowly after an initial drop with the increase in St value at u'/\bar{u} of 50%. At 10% u'/\bar{u} , the trends of F_N and F_M are similar. However, in F_M of 30% and higher, the τ_{res} tends to increase slowly with the increase in St value after an initial rapid decrease. As in Fig. 5.10 (a), it was confirmed through St value analysis that the τ_{res} decreased with increasing u'/\bar{u} .



(a)



(b)



(c)

Fig. 5.11 Changes in $EINO_x$ with St: (a) $u'/\bar{u} = 10\%$, (b) $u'/\bar{u} = 30\%$, and (c) $u'/\bar{u} = 50\%$.

Figure 5.11 shows the changes in $EINO_x$ with an increase in St for different u'/\bar{u} values for both the F_M and F_N flames. First, with respect to the F_N flame, the maximum St value decreases with increasing u'/\bar{u} . The maximum St value in Fig. 5.11(a) is approximately 17. However, in Fig. 5.11(c), it decreases to approximately 9. Thus, the maximum St value decreases with increasing u'/\bar{u} .

The trend in $EINO_x$ at $u'/\bar{u} = 10\%$ in Fig. 5.11(a) can be described as follows: $EINO_x$ first increases sharply, then decreases sharply at $St = 3$, and finally plateaus at $St = 9$. Subsequently, it increases again from $St = 9$ to the maximum St value. The trends shown in Figs. 5.11(b) and (c) are similar to those in (a). However, there are points where the heights of the F_N and F_M flames have the same value as $EINO_x$ at some St value. For $St \leq 6$ in Fig. 5.11(a), the F_M and F_N flames have almost similar $EINO_x$ values despite having different St values. This trend is also shown in Figs. 5.11(b) and (c). Figure 5.11(b) shows the trend in $EINO_x$ for $St \leq 6$ while Fig. 5.11 (c) shows the trend in $EINO_x$ for $St \leq 9$. Thus, the NO_x emissions of the F_N and F_M flames, which had different heights in the pinch-off flame, were similar. This result is in contrast to the increase in the NO_x emissions with an increase in the flame height. Thus, it was confirmed that, in the case of pinch-off flames, both F_M and F_N can be used for the analysis of the exhaust emission characteristics.

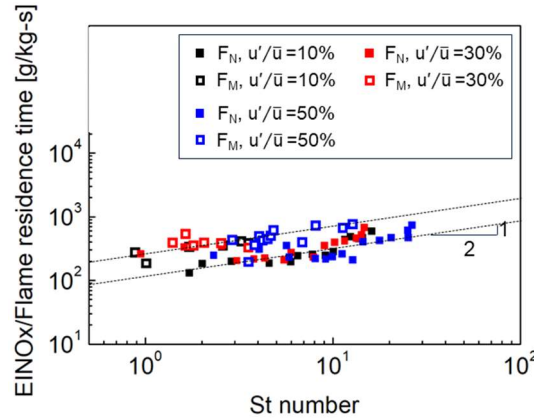


Fig. 5.12 Effect of St on $EINO_x$ normalized with respect to flame residence time (τ_{res}) as analyzed from viewpoints of F_M and F_N .

Figure 5.12 shows the effect of St on $EINO_x$ normalized with respect to τ_{res} . The solid

squares represent F_N while the open squares represent F_M . In the case of F_N , for every u'/\bar{u} value, the normalized $EINO_x$ value follows the 1/2-power scaling law. The same trend is observed in the case of F_M . However, the intercepts in the cases of F_M and F_N are different even though the slopes of their curves are the same. This is an interesting result indicating that the NO_x emission trends of F_N and F_M are similar and can predict increases in the St value. The following conclusions can be drawn from the results of the scaling of $EINO_x$ for the F_N and F_M flames. When analyzing and predicting the characteristics of the exhaust emissions from pinch-off flames, a specific flame structure, through the factor of flame height, it was confirmed that both F_M and F_N match well.

CHAPTER 6

EFFECTS OF STRAIN RATE AND SHEAR STRESS ON STRUCTURE OF PINCH-OFF AND NONPINCH-OFF FLAMES

6.1 Objectives

Oscillating combustion, which is used for NO_x reduction in industrial radiant tube burner systems, has been actively researched recently [3,150,151]. It involves generating flame-puffing [44] by forcibly controlling fuel flow rates using a control valve. Although several studies have focused on NO_x reduction and heat transfer for oscillating combustion, research on the flame structure, which is essential for elucidating the mechanism of NO_x reduction, remains insufficient.

Oscillating combustion involves a periodic flow structure in which lean and rich fuel mixtures are provided cyclically, and fuel lean and rich are gradually attenuated downstream of the flame [3]; this reduces NO_x emissions and increases the heat transfer rate. However, as the number of oscillating cycles increases, the NO_x reduction effect is weakened [152]. When the number of oscillating cycles is increased, the oscillating combustion effect is reduced if the ejected flame downstream merges with the next flame front. In oscillating combustion, the flame structure changes owing to the shear effect caused by the intrinsic process of periodically ejecting the flame. Therefore, it is important to study the shear effect of the flame surface to perform physical analysis of oscillating combustion.

Acoustic excitation in a non-premixed flame exhibits various flame structures [111,153] according to the frequency and velocity perturbation intensity. Kim et al. [30] confirmed NO_x reduction with the flame height decreasing at the resonance frequency and local flame extinguishment being caused by excessive strain rates [50]. Ahn et al. [51] analyzed the heat release [104] from a pinch-off flame during acoustic excitation in a Burke-Schumann-based [53] flame and examined the pinch-off mechanism under a high strain rate and vortical structure. In addition, through pinch-off mapping, pinch-off was confirmed to occur in the low-frequency range. Although sufficient research has been conducted on the strain rate in flame extinction, few studies have focused on the correlation between strain rate and shear

stress.

Therefore, in this study, the correlation between the strain rate and shear stress was analyzed by simulating oscillating combustion through acoustic excitation. The aim was to understand the physical phenomenon of pinch-off through a correlation analysis of the strain rate and shear stress under various fuel and air velocities. For this purpose, simultaneous measurements with OH* chemiluminescence and particle image velocimetry (PIV) were performed, and the strain rate and shear stress were calculated through post-processing. In one of our previous studies [104], the shearing between the fuel and air boundary layer was assumed to have minimal effect under the same fuel and air velocity (Burke-Schumann flame [53]). In this study, a shear effect due to differences between the fuel and air velocity—that is, the two fluid boundary layers—was considered. Therefore, the shear effect reduces the strain rate and is thus expected to play an important role in suppressing pinch-off. Accordingly, we intended to analyze the correlation between the strain rate and shear effect for pinch-off and nonpinch-off flames when two fluid boundary layers exist.

6.2 Experimental setup and methodology

Figure 6.1 (a) shows a schematic of the combustor of a non-premixed flame. It is a rectangular combustor with dimensions of 50×50 mm, and the fuel nozzle ($D_{\text{inner}}=5$ mm) is a burner mounted at the center. The top of the combustor is equipped with quartz windows on four sides for visualization, and the field of view is 35 × 90 mm. The cameras for visualization analysis are each located on the side of the combustor. Fuel and air are supplied from the bottom of the nozzle, and loudspeakers (Beyma, 8 inch, 100 W) for acoustic excitation provide perturbation to the fuel and air, respectively. Acoustic data are acquired using a hot-wire anemometer (HWA) mounted on the bottom of the nozzle, and the amplitude (λ) and phase ($^\circ$) are manually controlled using LabVIEW.

The OH* chemiluminescence measurement system for flame structure included the following components: A high-speed camera (LaVision, Highspeedstar 8, maximum resolution 1024 × 1024 @7 kHz) and an intensifier (LaVision, Highspeed IRO) were used to amplify the OH intensity. A Nikon UV 100 mm f/2.8 lens, an OH band pass filter (VZ-Image, Filter LIF for OH enhanced 310±20 nm), and an intensifier gate of 300 μ s were used. The PIV setup for flow field measurements comprised the following devices: an Nd:YLF laser (Photonics Industries DM, 527 nm; 2.7 mJ/pulse @3.5 kHz), a high-speed camera (LaVision, Highspeedstar 8, maximum resolution 1024 × 1024 @7 kHz), a NIKKOR AF MICRO 105 mm f/2.8 lens, and a 527 nm bandpass filter (VZ-image, Filter 527±5 nm).

In this study, flow field analysis was performed through simultaneous measurement of OH* chemiluminescence and PIV. The time interval between the OH chemiluminescence camera and PIV camera was 200 μ s, and the resolution of the PIV image was 1.10×10⁻¹ mm/pixel. Vector calculations were performed using LaVision Davis 8.3. For this purpose, post-processing was performed in the multi-pass mode with a decreasing interrogation window size. The first process involved three passes at a 48 × 48 pixel interrogation window size with 50% overlap, and the second process involved four passes at a 32 × 32 pixel interrogation window size with 75% overlap. Fast Fourier transform (FFT)-based cross-correlation was also performed. PIV particles were supplied to the air and fuel supply lines, and titanium (IV) oxide particles (powder, <5 μ m, ≥99.9% trace metals basis) were used.

The strain rate (6-1) and shear stress (6-2) were used as parameters for the flow field analysis which was performed using LaVision Davis 8.3 and MATLAB. The strain rate was

calculated using the following formula:

$$\text{Strain rate (1/s)} = 1/2 \left(\frac{\partial u_y}{\partial x} + \frac{\partial u_x}{\partial y} \right) \quad (6-1)$$

The shear stress was calculated in MATLAB using the extracted velocity component, based on the following equation:

$$\text{Shear stress (1/s)} = \mu \frac{\partial u_x}{\partial y} + \eta \frac{\partial u_y}{\partial x} \quad (6-2)$$

where μ is the dynamic molecular viscosity of the fluid, and η is the dynamic eddy viscosity, which depends on the state of the turbulent motion. Figure 6.1 (b) shows the result of simultaneous measurement; the left side shows the PIV raw image of the vortical structure, and the right side shows the OH^* image. The vortical structure was confirmed to have formed inside the flame structure due to acoustic excitation. The flame surface was indicated by the stoichiometric contour, and the position of the contour was defined based on a previous study [7,104].

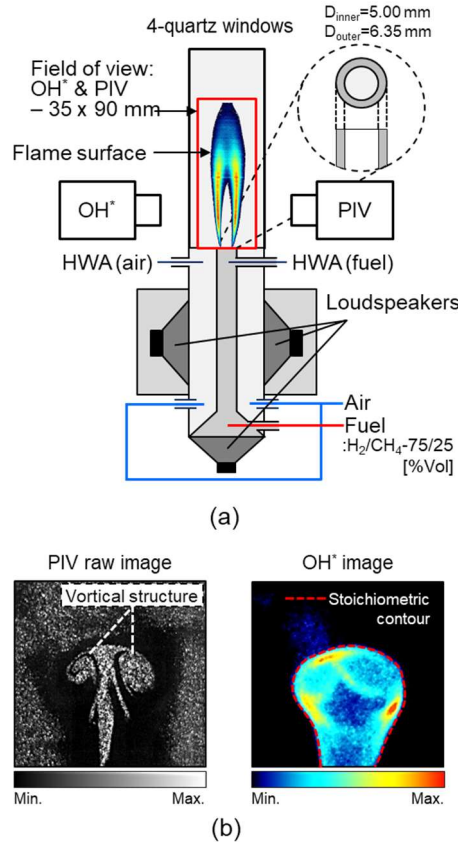


Fig. 6.1 (a) Schematic of the experimental setup; (b) Simultaneous measurement results for acoustic excitation at 80 Hz. Left: vortical structure of PIV raw image; right: OH* image.

Table 6.1 lists the experimental conditions used in this study. The fuel was a mixture of 75% H₂ and 25% CH₄ by volume, and air was used as the oxidizer. The aforementioned volume ratio was selected for the following reasons: The ultimate aim of this study was to design a low-NO_x burner capable of combustion in pure hydrogen. To this end, 100% pure hydrogen combustion was targeted in the flame stability analysis under fuel composition (H₂/CH₄-75/25%). The acoustic excitation was 80 Hz, and a velocity perturbation intensity (u'/\bar{u}) was 10–50%. u'/\bar{u} is the ratio of the axial velocity perturbation (u') to the average velocity (\bar{u}) and is defined as the normalized intensity of the acoustic amplitude (λ). The phases of fuel and air were manually controlled, and the experiment was performed when the acoustic signal was within 5° in-phase.

Table 6.1 Experimental conditions

Parameter	Condition
Fuel composition [%Vol]	H ₂ /CH ₂ - 75/25
Oxidizer	Air
Forcing frequency [Hz]	0–300 (20 Hz steps)
Velocity perturbation intensity (u'/\bar{u})	0–50% (10% steps)

Table 6.2 lists experimental conditions in terms of the fuel and air bulk velocity and the Reynolds number (Re). Case 1 refers to our previous study [104], where the shear effect was assumed to not have any theoretical effect. In Cases 2 and 3, the shear effect not considered in our previous study could be confirmed.

Table 6.2 Various fuel (u_F) and air (u_A) bulk velocities.

Case	1	2	3
u_F [m/s]	1.0	1.0-4.5	1.0
u_A [m/s]	1.0	1.0	1.0-4.5
Re	3012	3012-3357	3012-13208

Table 6.3 shows the correlation between the strain rate and shear stress under the experimental conditions listed in Table 6.2; two pinch-off and two nonpinch-off conditions are observed. Based on Case 1-1, the conditions in the previous study, the pinch-off conditions (Case 2-1), and the nonpinch-off (Case 2-2) conditions for increasing u_F were analyzed. In addition, the shear stress for the nonpinch-off conditions with increasing u_A (Case 3-1) was analyzed.

Table 6.3 Experimental conditions for analyzing the flame characteristics of pinch-off and non-pinch-off.

Case	Pinch	Pinch	Nonpinch	Nonpinch
	1-1	2-1	2-2	3-1
u_F [m/s]	1.0	2.5	3.0	1.0
u_A [m/s]	1.0	1.0	1.0	3.0
Re	3012	3160	3209	8838

6.3 Flame response characteristics according to fuel and air bulk velocity

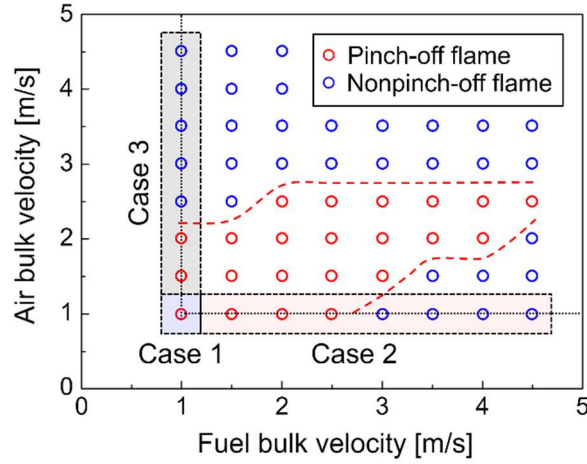


Fig. 6.2 Pinch-off mapping of fuel (u_F) and air (u_A) bulk velocity at 80 Hz and $u'/\bar{u}=50\%$.

Figure 6.2 (a) shows the mapping of pinch-off and nonpinch-off according to various fuel (u_F) and air (u_A) bulk velocities. All data points were manually and uniformly controlled with a u'/\bar{u} value of 50% at a forcing frequency of 80 Hz. As mentioned, in Case 1 ($u_F=u_A=1$ m/s) [104], it was theoretically assumed that the shear effect was negligible. In Case 2, shear due to u_F was considered under the condition that u_F increases when u_A is fixed. Case 3 included a shear effect due to u_A under the condition opposite to that in Case 2.

The trend of pinch-off with increasing u_F (Case 2) was as follows: A transition boundary, which is a boundary between pinch-off and nonpinch-off, is formed in the range of $u_F=2.5$ – 3.0 m/s. This boundary shifts to the right with increasing u_A . By contrast, the pinch-off (Case 3) with an increase in u_A tends to form a transition boundary in the range of $u_A = 2.0$ – 2.5 m/s but does not increase beyond 2.5 m/s. This trend is considered to be due to the difference in flow rate between u_F and u_A (as shown in Table 6.2, u_A is 3.9 times u_F). Moreover, the response is confirmed to be weak when the flow rate is larger, even for the same u'/\bar{u} .

In this study, based on Fig. 6.2, the correlation between the strain rate and shear stress was confirmed at four points. For Case 1, the pinch-off (Case 2-1) and nonpinch-off (Case 2-2) according to the increase in u_F and the nonpinch-off (3-1) according to the increase in u_A was analyzed. In the following section, we analyze the correlation between the strain rate and shear stress according to u_A and u_F .

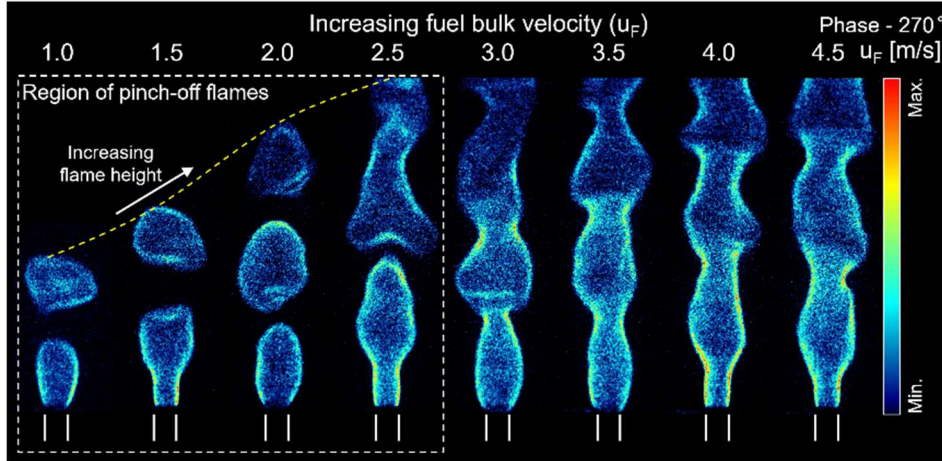


Fig. 6.3 OH* images for Case 2 for various u_F at 80 Hz, $u'/\bar{u}=50\%$, when $u_A=1$ m/s constant.

The OH* image in Fig. 6.3 shows a transition from a pinch-off flame to a nonpinch-off flame when u_F increases (Case 2). Based on the flame structure analysis, the flame height increased as the fuel flow increased with increasing u_F . The pinch-off is in the range of $u_F=1.0\text{--}2.5$ m/s; nonpinch-off occurs for $u_F > 3.0$ m/s. The Richardson number ($\xi= Ri_s^{1/3} x/d_s$) [123] was calculated to confirm the position of the transition boundary. For $u_F=2.5\text{--}3.0$ m/s, $1 \leq \xi$ was observed. In the pinch-off region, the Richardson number was momentum-dominant, but in the nonpinch-off region, it was confirmed to transition to buoyancy-dominant.

As u_F increased, the shear effect of the flame intensified, and the flame structure became deformed. In the Case of $u_F=u_A=1.0$ m/s, the main flame [104] attached to the nozzle and the pocket flame separated from the nozzle are pinch-off flames. However, at $u_F=2.5$ m/s, the shape of the pocket flame is distorted, and the distance between the main flame and the pocket flame is reduced.

In the nonpinch-off region, where the shear effect increases with increasing u_F , a constant waveform of the flame surface appears. This is because, as the forcing frequency increases, the acoustic properties of the decreasing wavelength are projected onto the flame surface [104]. The experimental was conducted with a fixed frequency of 80 Hz, and a certain waveform was projected. However, the waveform changed as the forcing frequency increased.

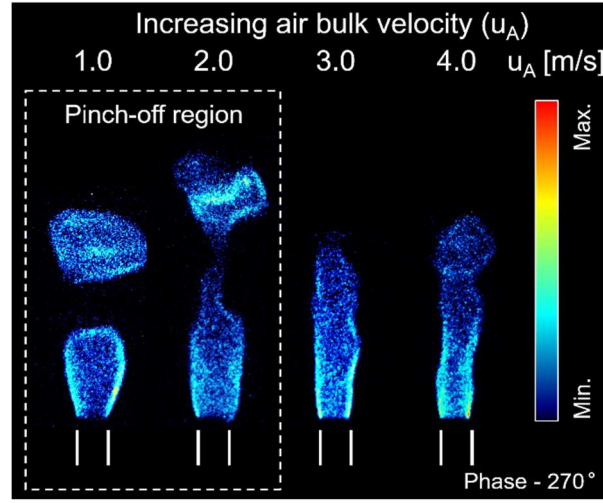


Fig. 6.4 OH* images for Case 3 for various u_A at 80 Hz, $u'/\bar{u}=50\%$, when $u_A=1$ m/s constant.

The OH* image in Fig. 6.4 depicts a transition from a pinch-off to a nonpinch-off flame when u_A increases (Case 3). The transition from pinch-off to nonpinch-off occurs at $u_A = 3.0$ m/s or more. In Case 2 of Fig. 6.3, the flame height also increases with increasing fuel flow rate. In Case 3, however, the flame height is almost unchanged. The factor that determines the flame height is the velocity of the fuel flow, and Case 2 shows a constant flame height because the fuel flow is fixed. The mechanism of nonpinch-off in Case 3 is as follows: As u_A increases, the oscillation magnitude decreases because the vortices are rapidly pushed downstream [14]. Similar to that in Case 2, the Richardson number calculation showed that the transition tendencies of pinch-off and nonpinch-off were similar in Case 3 as well.

The global flame responses in Cases 2 and 3 were confirmed through OH* image analysis, and the structures of the pinch-off and nonpinch-off flames were compared. In the following section, the correlation between the strain rate and shear stress of the pinch-off and nonpinch-off flames is analyzed based on the simultaneous measurement of OH* chemiluminescence and PIV.

6.4 Characteristics of pinch-off flame with increasing fuel bulk velocity

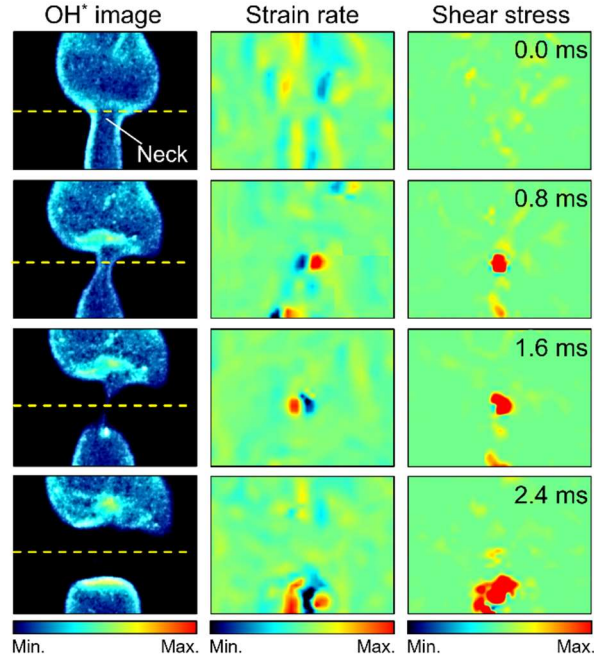


Fig. 6.5 Instantaneous simultaneous measurement result of Case 2-1 at 80 Hz, $u'/\bar{u}=50\%$, from left- OH^* image of pinch-off, strain rate, and shear stress.

Figure 6.5 shows the results of simultaneous OH^* chemiluminescence and PIV measurements in Case 2-1 ($u_F=2.5$ m/s, $u_A=1.0$ m/s). The flame neck was enlarged to analyze the pinch-off process. The pinch-off process in Case 1-1 ($u_F=u_A=1.0$ m/s) is explained in detail in our previous study [104]. The pinch-off process in Case 2-1 is similar to that in Case 1-1, despite the shear effect. The pinch-off process can be explained simply as follows: The deformation of the flame neck occurs during 0.0–0.8 ms. At 0.0 ms, the diameter of the neck begins to change due to local deformation, and at 0.8 ms, the neck becomes very thin. After 1.6 ms, the flame is separated into the main flame and pocket flame and is pinched off.

The middle and right images in Fig. 6.5 depict the strain rate and shear stress field, respectively. Strain rate is an indicator of flame deformation, and shear stress is an indicator of the shear effect due to fuel and air. The main location where the strain rate affects is near the neck [30] where the flame deforms. Shear stress also affects the strain rate at a similar

location [154]. It can be inferred that the two factors are correlated with the flame deformation considering the agreement between the strain rate and the location of the shear stress field. To analyze the correlation between pinch-off and the strain rate and shear stress two factors, the strain rate and shear stress were calculated along the yellow dashed line shown in the OH* image in Fig. 6.5. In addition, comparative verification was performed using the data of a previous study (Case 1-1) [104] and the current data.

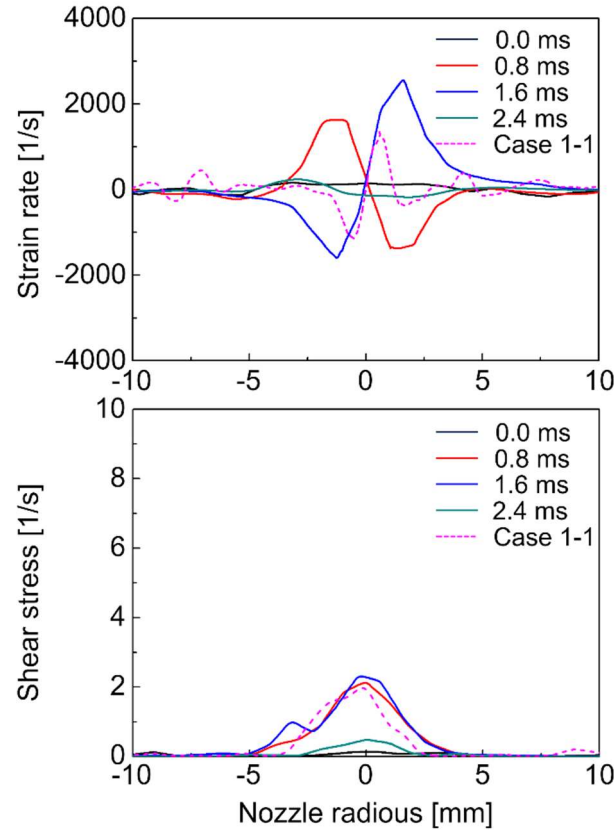


Fig. 6.6 Strain rate and shear stress calculated along the yellow dashed line in Fig. 6.5.

Figure 6.6 shows the strain rate (1/s) and shear stress (1/s) calculated along the yellow dashed line in Fig. 6.5. At 0.8 ms, when the flame neck was formed, the strain increased to 1625 1/s. At 1.6 ms, when the flame was completely separated, the strain rate had a maximum value of 2593.447 1/s. Contrarily, when the flame deformation was not large, the strain rate was relatively low. These results were compared with those of Case 1-1 [104], where the

maximum strain rate was 1387.187 1/s at pinch-off. Thus, the strain rate in this study was approximately 85% higher than that in the previous study.

Even in Case 2-1, the strain rate increased, despite the greater shear effect due to the increase in u_F . The trend was opposite to that based on the hypothesis that the effect of the strain rate would weaken if the shear stress increased. The reason for this is that as the fuel flow rate increases, the strain rate for pinch-off also increases. However, it is necessary to understand whether this tendency is specific to a pinch-off flame.

The shear stress calculated from the strain rate measured in the previous study was compared with the shear stress calculated along the yellow dashed line in Fig. 6.5. The shear stress at 0.8 ms, when the flame neck is formed, was 2.1338 1/s, and the shear stress at 1.6 ms, when the flame is completely separated, was 2.329 1/s, which is the maximum value. When the flame deformation was not large, the shear stress was low. The shear stress in Case 1-1 was 2.008 1/s, which was 15% lower than that in this study.

The comparative analysis of Case 1-1 and Case 2-1 revealed that the shear stress increased with u_F , but only by approximately 15%. Compared with the 85% increase in the strain rate, the increase in the shear stress was relatively low. Thus, when u_F increases in a pinch-off flame, the shear stress also increases but not significantly.

6.5 Characteristics of non-pinch-off flame by increasing fuel bulk velocity

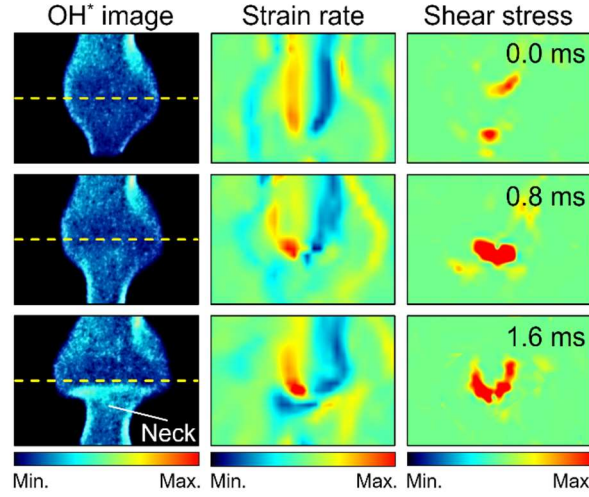


Fig. 6.7 Instantaneous simultaneous measurement result of Case 2-2 at 80 Hz, $u'/\bar{u}=50\%$, from the left- OH^* image of the nonpinch-off, strain rate, and shear stress.

Figure 6.7 shows the nonpinch-off results obtained via simultaneous measurement of OH^* chemiluminescence and PIV in Case 2-2 ($u_F=3.0$ m/s, $u_A=1.0$ m/s). The values of u_F in Case 2-1 ($u_F=2.5$ m/s) and Case 2-2 ($u_F=3.0$ m/s) did not differ significantly; however, Case 2-2 included a nonpinch-off flame. A physical analysis is necessary to determine the factors that cause the transition from pinch-off to nonpinch-off. The process of nonpinch-off is simple. The flame diameter decreases sufficiently to form a flame neck with flame deformation, and the diameter does not decrease sufficiently to cause pinch-off. In acoustic excitation, the flow is caused by reverse flow and entrainment of the surrounding air by the vortical structure[111]. At this time, a stagnation point[104] is formed around the nozzle tip, and the stagnation point of nonpinch-off is formed further downstream than that of pinch-off, which reduces the effect of reverse flow. The reduced reverse flow effect is a factor that makes it a nonpinch-off flame.

The distributions of the strain rate and shear stress field in Fig. 6.7 are similar to those shown in Fig. 6.5; the same observation was confirmed even under the nonpinch-off conditions. This section analyzes the correlation between the strain rate and shear stress under nonpinch-off conditions and the role of this correlation in nonpinch-off. For this purpose, the strain rate and shear stress calculated along the yellow dashed line were analyzed, as shown

in Fig. 6.6.

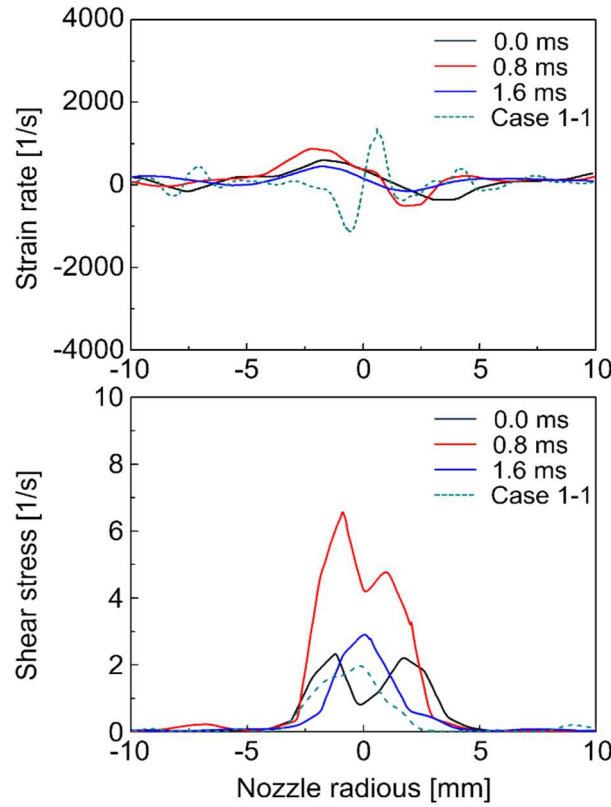


Fig. 6.8 Strain rate and shear stress calculated along the yellow dashed line in Fig. 6.7.

The strain rate (1/s) and shear stress (1/s) calculated along the yellow dashed line in Fig. 6.7 are shown in Fig. 6.8 and compared with those in Case 1-1. Overall, the strain rate of nonpinch-off is lower than that in Case 1-1 (1387.187 1/s). Although u_F increased more than in Case 2-1 ($u_F=2.5$ m/s), the strain rate (peak value: 875.9441 1/s) was reduced by approximately 65%. In Fig. 6.6, the strain rate increased even when u_F increased, but in Fig. 6.8, it decreased. Thus, it was confirmed that the strain rate can decrease as u_F increases. It can be approximated that there is some correlation between u_F and strain rate. It is therefore necessary to identify the factors that cause the strain rate to decrease with increasing u_F .

The shear stress calculated in the previous study (Case 1-1) was compared with that calculated along the yellow dashed line in Fig. 6.8. Unlike in Fig. 6.6 (Case 2-1), the shear stress value is large. The peak shear stress is 6.6560 1/s, which is 3.3 times the value Case 1-

1 (2.0087 1/s). Although the strain rate decreased by about 65%, the shear stress increased. According to these results, when the strain rate increases, the shear stress decreases, and this seems to be a factor inhibiting each other. In the pinch-off region (Fig. 6.6), the strain rate plays a major role, whereas the shear stress is controlled. However, in the non-pinch-off region (Fig. 6.8), the shear stress plays a major role, while the strain rate is suppressed and reduced.

6.6 Characteristics of nonpinch-off flame with increasing air bulk velocity

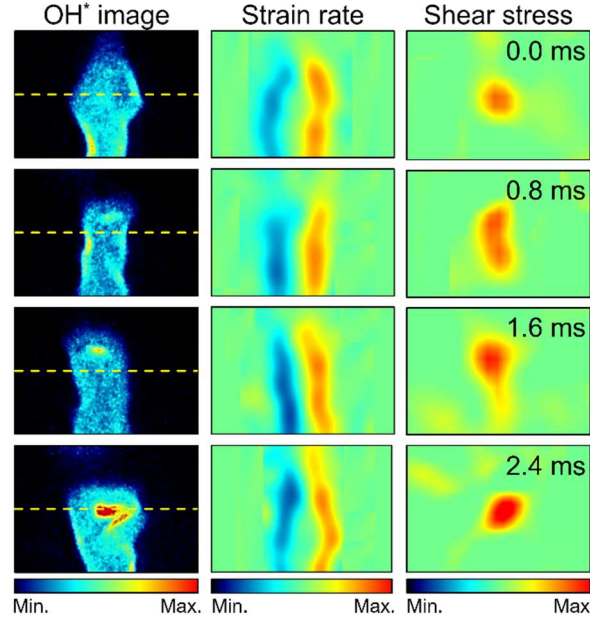


Fig. 6.9 Instantaneous simultaneous measurement result of Case 3-1 at 80 Hz, $u'/\bar{u}=50\%$, from the left-OH* image of the nonpinch-off, strain rate, and shear stress.

Figure 6.9 shows the nonpinch-off results obtained via simultaneous measurement of OH* chemiluminescence and PIV in Case 3-1 ($u_A=3.0$ m/s, $u_F=1.0$ m/s). To verify the correlation between the strain rate and shear stress in Case 2-2 (nonpinch-off), analysis was performed under nonpinch-off conditions by increasing u_A .

The nonpinch-off in Fig. 6.9 (Case 3-1) is the same as in Fig. 6.7 (Case 2-2). However, in Fig. 6.9, the direction of action of the shear layer is opposite. Figure 6.7 shows the shear effect rotating outward with respect to the fuel jet, and Fig. 6.9 shows the shear effect of internal rotating in the fuel jet direction owing to an increase in coaxial air. Therefore, the flame structure formed by the opposite shear effect has the following characteristics. The distinction of flame neck is not clear, and the change in flame diameter is small. In Fig. 6.3 (Case 2), it is easy to distinguish the flame neck, and there is a change in the flame diameter due to the waveform of the flame surface. However, in Fig. 6.9 (Case 3-1), the projection of

the waveform of the flame surface is not clear, so the change in flame diameter is not clear.

The strain rate (1/s) and shear stress (1/s) calculated along the yellow dashed line in Fig. 6.9 are shown in Fig. 6.10 and compared with those in the previous study (Case 1-1). In this section, the nonpinch-off in Case 3-1 ($u_A=3.0$ m/s), with the shear stress acting in the direction opposite to that in Case 2-2 ($u_F=3.0$ m/s), is analyzed. In addition, analysis was performed to verify the results of strain rate and shear stress for the nonpinch-off region shown in Fig. 6.8 (Case 2-2).

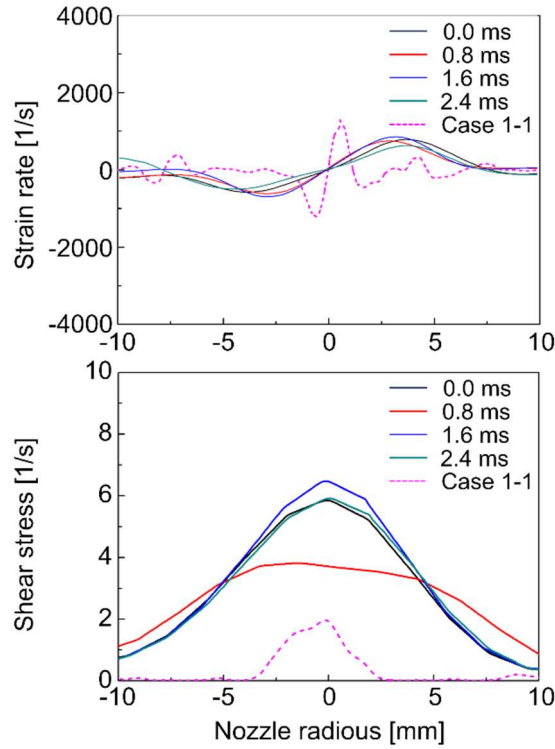


Fig. 6.10 Strain rate and shear strength calculated along the yellow dashed line in Fig. 6.9.

The strain rate in Case 3-1 (826.921 1/s) is lower than that in Case 1-1 (1387.187 1/s) by approximately 60%. The shear stress exhibits a tendency similar to that in Case 2-2. The peak shear stress in Case 2-3 is 6.5028 1/s, which is 3.2 times that in Case 1-1 (2.0087 1/s). The strain rate decreased by about 60%, and the shear stress increased by 3.2 times. This tendency is consistent with that shown in Fig. 6.8 (Case 2-2), and the tendencies of strain rate and shear stress in the nonpinch-off region were re-verified. Accordingly, when the shear effect exceeds

a certain threshold, the shear stress is considered to play a role in suppressing the strain rate. However, when the shear effect is below the threshold, the strain rate has a major influence. In this case, although the shear effect affects the flow, it is a factor that suppresses the shear stress. These research results have the potential to be utilized for artificially controlling the flame structure. They are also valuable as an analysis of the physical phenomenon of oscillating combustion to reduce NO_x.

CHAPTER 7

CONCLUSION

7.1 Conclusions

This study was aimed at understanding the flame response characteristics on the effect of acoustic excitation. OH* chemiluminescence, OH PLIF, and PIV measurements were used to analyze response characteristics and local flame extinction, the main parameters being flame height, FTF, NO_x emission index, strain rate, and shear strength.

The primary conclusions of this thesis are as follows.

First, flame response characteristics analysis confirmed that the non-premixed and premixed flames had nonlinear and linear characteristics, respectively. This difference is due to the flame structure caused by acoustic excitation. Linear and nonlinear characteristics were verified by comparing the structures of two flames with parameters of flame height.

Secondly, the mechanism of pinch-off, occurring under specific acoustic conditions, was analyzed. It was confirmed that the flame neck was formed by the flow characteristics of the vertical structure, and the pinch-off was due to the high strain rate. Thirdly, the structure of the pinch-off flame was defined, and the correlation between the NO_x emission index and the flame height was determined. Even though the Strouhal numbers were different, the EINO_x emission characteristics were similar, indicating that flame height and EINO_x may not be proportional. NO_x scaling by the flame residence time and the normalized NO_x emission index confirmed that the data fit the 1/2-power scaling law curve.

Finally, it was confirmed that the strain rate dominates in the pinch-off region and the shear effect dominates in the non-pinch-off region. The fuel bulk velocity (shear effect) and the strain rate increase, while the strain rate decreases in the non-pinch-off region where the shear strength is dominant. Accordingly, the correlation between strain rate and shear strength was confirmed.

The results described in Chapter 3 are helpful in designing the burner of the TAPS combustor. In general, non-premixed flames are more stable flames than premixed flames. However, the result of the response characteristics of this study confirmed that the premixed flame had a stable frequency, similar to the non-premixed flame. Therefore, the TAPS combustor suggested operating the system within a stable frequency to provide information

on unstable frequencies using the main and the pilot flame.

Chapters 4 and 6 are studies on local flame extinction, using strain rate and shear strength as parameters. Correlation analysis of strain rate and shear strength has value as a new indicator in the field of flame extinction. In the field of oscillation combustion utilizing the flame extinction phenomenon, there are very few studies on the flame structure. The results of this study help elucidate the mechanism of NO_x emission reduction in oscillation combustion.

Chapter 5 describes the NO_x analysis of the pinch-off flame. The correlation between specific flames and NO_x can provide insight into non-premixed flames and specific flame structures such as oscillation combustion. In addition, it can be utilized in the TAPS combustor that burns the main flame and the pilot flame simultaneously

7.2 Limitation and future work

1. Individual comparison of non-premixed and premixed flames is a limitation of this study. The TAPS combustor simultaneously utilizes the main flame and the pilot flame. Therefore, the response study cannot directly help the TAPS combustor study. Therefore, as a future study, a lab-scale TAPS burner is manufactured, and the response characteristics are analyzed by simultaneous reaction of the main flame and the pilot flame. In addition, by comparing this result and individual data, the response of a single nozzle and the result of a lab-scale burner are verified.

2. In this study, H_2/CH_4 mixed fuel was used in volume ratios of 50/50 and 75/25. Ultimately, the goal was pure H_2 combustion with 0% CH_4 and 100% H_2 . Therefore, the characteristics of NO_x emissions generated during pinch-off flame in pure H_2 will be analyzed in further studies.

3. A strain rate parameter was introduced to analyze local flame extinction. A high strain rate was confirmed at 80 Hz and specific range of velocity perturbation intensities. However, there is a limit, and the exact threshold value for pinch-off was not confirmed. It will be expensive and time-consuming to identify the pinch-off threshold experimentally. Therefore, rather than empirically, we will try to identify it by computational methods (i.e. ANSYS, OpenFOAM, Cantera, etc.). Although the correlation between strain rate and shear strength was analyzed, it is unclear whether a causal relationship is present. Therefore, a threshold study of strain rate is expected to determine whether strain rate and shear strength are causal.

REFERENCES

- [1] M.J. Foust, D. Thomsen, R. Stickles, C. Cooper, W. Dodds, Development of the GE aviation low emissions TAPS combustor for next generation aircraft engines, 50th AIAA Aerosp. Sci. Meet. Incl. New Horizons Forum Aerosp. Expo. (2012) 936–944. <https://doi.org/10.2514/6.2012-936>.
- [2] J.E. Temme, P.M. Allison, J.F. Driscoll, Combustion instability of a lean premixed prevaporized gas turbine combustor studied using phase-averaged PIV, *Combust. Flame*. 161 (2014) 958–970. <https://doi.org/10.1016/j.combustflame.2013.09.021>.
- [3] John C. Wagner, Nox Emission Reduction By Oscillating Combustion Final Report, 2004.
- [4] S. Dodo, T. Asai, H. Koizumi, H. Takahashi, S. Yoshida, H. Inoue, Performance of a multiple-injection dry low NO_x combustor with hydrogen-rich syngas fuels, *J. Eng. Gas Turbines Power*. 135 (2013) 1–7. <https://doi.org/10.1115/1.4006691>.
- [5] N.A. Magina, Dynamics of harmonically forced nonpremixed flames, Ph.D. Thesis, Georg. Inst. Technol. (2016).
- [6] R.D. Ray, Combustion Processes in Propulsion Control, Noise and Pulse Detonation, 2005. <https://doi.org/10.1016/B978-0-12-369394-5.X5000-8>.
- [7] S.A. Kaiser, J.H. Frank, Spatial scales of extinction and dissipation in the near field of non-premixed turbulent jet flames, *Proc. Combust. Inst.* 32 (2009) 1639–1646. <https://doi.org/10.1016/j.proci.2008.05.082>.
- [8] H. Kobayashi, A. Hayakawa, K.D.K.A. Somarathne, E.C. Okafor, Science and technology of ammonia combustion, *Proc. Combust. Inst.* 37 (2019) 109–133. <https://doi.org/10.1016/j.proci.2018.09.029>.
- [9] C.T.C. Chi-Ming Lee, NASA Environmentally Responsible Aviation Project Develops Next-Generation Low-Emissions Combustor Technologies (Phase I), *J. Aeronaut. Aerosp. Eng.* 02 (2013) 1–10. <https://doi.org/10.4172/2168-9792.1000116>.
- [10] H.C. Cho, K.W. Cho, NO_x Emission Characteristics in Radiant Tube Burner with Oscillating Combustion Technology, *J. Energy Power Eng.* 5 (2011) 105–111.
- [11] C. Li, S. Li, X. Cheng, M. Zhu, Measurements and modeling of the dynamic response of a pilot stabilized premixed flame under dual-input perturbation, *J. Eng.*

- Gas Turbines Power. 140 (2018). <https://doi.org/10.1115/1.4040175>.
- [12] R.M. Jones, N.Z. Shilling, IGCC Gas Turbines for Refinery Applications, 2003.
 - [13] W. York, M. Hughes, J. Berry, T. Russell, Y.C. Lau, S. Liu, M.D. Arnett, A. Peck, N. Tralshawala, M. Benjamin, M. Iduate, J. Kittleson, A. Garcia-, J. Delvaux, F. Casanova, B. Lacy, B. Brzek, P. Palafox, B. Ding, B. Badding, D. McDuffie, Advanced IGCC/Hydrogen Gas Turbine Development, 2015.
 - [14] H. Gohari Darabkhani, Q. Wang, L. Chen, Y. Zhang, Impact of co-flow air on buoyant diffusion flames flicker, *Energy Convers. Manag.* 52 (2011) 2996–3003. <https://doi.org/10.1016/j.enconman.2011.04.011>.
 - [15] G. Leach, The energy transition, *Energy Policy.* 20 (1992) 116–123. [https://doi.org/10.1016/0301-4215\(92\)90105-B](https://doi.org/10.1016/0301-4215(92)90105-B).
 - [16] A.B. Gallo, J.R. Simões-Moreira, H.K.M. Costa, M.M. Santos, E. Moutinho dos Santos, Energy storage in the energy transition context: A technology review, *Renew. Sustain. Energy Rev.* 65 (2016) 800–822. <https://doi.org/10.1016/j.rser.2016.07.028>.
 - [17] J. Tian, L. Yu, R. Xue, S. Zhuang, Y. Shan, Global low-carbon energy transition in the post-COVID-19 era, *Appl. Energy.* (2021) 118205. <https://doi.org/10.1016/j.apenergy.2021.118205>.
 - [18] T. Capurso, M. Stefanizzi, M. Torresi, S.M. Camporeale, Perspective of the role of hydrogen in the 21st century energy transition, *Energy Convers. Manag.* 251 (2022) 114898. <https://doi.org/10.1016/j.enconman.2021.114898>.
 - [19] W.D. York, W.S. Ziminsky, E. Yilmaz, Development and testing of a low NOx hydrogen combustion system for heavy duty gas turbines, *Proc. ASME Turbo Expo.* 2 (2012) 1395–1405. <https://doi.org/10.1115/GT2012-69913>.
 - [20] A. Haj Ayed, K. Kusterer, H.H.W. Funke, J. Keinz, C. Striegan, D. Bohn, Improvement study for the dry-low-NOx hydrogen micromix combustion technology, *Propuls. Power Res.* 4 (2015) 132–140. <https://doi.org/10.1016/j.jprr.2015.07.003>.
 - [21] H. Kang, T. Lee, U. Jin, K.T. Kim, Experimental investigation of combustion instabilities of a mesoscale multinozzle array in a lean-premixed combustor, *Proc. Combust. Inst.* 38 (2021) 6035–6042. <https://doi.org/10.1016/j.proci.2020.06.099>.
 - [22] M. Fleifil, A.M. Annaswamy, Z.A. Ghoneim, A.F. Ghoniem, S. Ducruix, D. Durox,

- S. Candel, V. Moreau, R.J.M. Bastiaans, S.G. Meyer, A.B. Collier, C.J. Rodger, C.A. Armitage, R. Balachandran, E. Mastorakos, R.S. Cant, C. Combustion, Theoretical and experimental determinations of the transfer function of a laminar premixed flame, *Combust. Flame*. 33 (2013) 1–6.
<https://doi.org/10.1016/j.apm.2007.12.005>.
- [23] T. Schuller, D. Durox, S. Candel, A unified model for the prediction of laminar flame transfer functions: Comparisons between conical and V-flame dynamics, *Combust. Flame*. 134 (2003) 21–34. [https://doi.org/10.1016/S0010-2180\(03\)00042-7](https://doi.org/10.1016/S0010-2180(03)00042-7).
- [24] D. Durox, T. Schuller, S. Candel, Combustion dynamics of inverted conical flames, *Proc. Combust. Inst.* 30 (2005) 1717–1724.
<https://doi.org/10.1016/j.proci.2004.08.067>.
- [25] K.T. Kim, J.G. Lee, B.D. Quay, D.A. Santavicca, Response of partially premixed flames to acoustic velocity and equivalence ratio perturbations, *Combust. Flame*. 157 (2010) 1731–1744. <https://doi.org/10.1016/j.combustflame.2010.04.006>.
- [26] B.D. Bellows, M.K. Bobba, A. Forte, J.M. Seitzman, T. Lieuwen, Flame transfer function saturation mechanisms in a swirl-stabilized combustor, *Proc. Combust. Inst.* 31 II (2007) 3181–3188. <https://doi.org/10.1016/j.proci.2006.07.138>.
- [27] W. Polifke, C. Lawn, On the low-frequency limit of flame transfer functions, *Combust. Flame*. 151 (2007) 437–451.
<https://doi.org/10.1016/j.combustflame.2007.07.005>.
- [28] D. Kim, J.G. Lee, B.D. Quay, D.A. Santavicca, K. Kim, S. Srinivasan, Effect of Flame Structure on the Flame Transfer Function in a Premixed Gas Turbine Combustor, *J. Eng. Gas Turbines Power*. 132 (2010) 021502.
<https://doi.org/10.1115/1.3124664>.
- [29] B. Ćosić, J.P. Moeck, C.O. Paschereit, Nonlinear instability analysis for partially premixed swirl flames, *Combust. Sci. Technol.* 186 (2014) 713–736.
<https://doi.org/10.1080/00102202.2013.876420>.
- [30] M. Kim, Y. Choi, J. Oh, Y. Yoon, Flame-vortex interaction and mixing behaviors of turbulent non-premixed jet flames under acoustic forcing, *Combust. Flame*. 156 (2009) 2252–2263. <https://doi.org/10.1016/j.combustflame.2009.08.004>.
- [31] A. Khosousi, S.B. Dworkin, Detailed modelling of soot oxidation by O₂ and OH in

- laminar diffusion flames, *Proc. Combust. Inst.* 35 (2015) 1903–1910.
<https://doi.org/10.1016/j.proci.2014.05.152>.
- [32] A. Veshkini, S.B. Dworkin, A computational study of soot formation and flame structure of coflow laminar methane/air diffusion flames under microgravity and normal gravity, *Combust. Theory Model.* 21 (2017) 864–878.
<https://doi.org/10.1080/13647830.2017.1308558>.
- [33] L. Zimmer, S. Kostic, S.B. Dworkin, A novel soot concentration field estimator applied to sooting ethylene/air laminar flames, *Eng. Appl. Comput. Fluid Mech.* 13 (2019) 470–481. <https://doi.org/10.1080/19942060.2019.1609583>.
- [34] K.C. Smyth, J.E. Harrington, E.L. Johnsson, W.M. Pitts, Greatly enhanced soot scattering in flickering CH₄/air diffusion flames, *Combust. Flame.* 95 (1993) 229–239.
- [35] J. Oh, Q.S. Khan, Y. Yoon, Nitrogen dilution effect on flame stability in a lifted non-premixed turbulent hydrogen jet with coaxial air, *Fuel.* 89 (2010) 1492–1498.
<https://doi.org/10.1016/j.fuel.2009.10.001>.
- [36] J. Oh, J. Hwang, Y. Yoon, EINO_x scaling in a non-premixed turbulent hydrogen jet with swirled coaxial air, *Int. J. Hydrogen Energy.* 35 (2010) 8715–8722.
<https://doi.org/10.1016/j.ijhydene.2010.04.159>.
- [37] J. Oh, P. Heo, Y. Yoon, Acoustic excitation effect on NO_x reduction and flame stability in a lifted non-premixed turbulent hydrogen jet with coaxial air, *Int. J. Hydrogen Energy.* 34 (2009) 7851–7861.
<https://doi.org/10.1016/j.ijhydene.2009.07.050>.
- [38] A. Mansouri, N.A. Eaves, M.J. Thomson, S.B. Dworkin, Influence of pressure on near nozzle flow field and soot formation in laminar co-flow diffusion flames, *Combust. Theory Model.* 23 (2019) 536–548.
<https://doi.org/10.1080/13647830.2018.1557746>.
- [39] D.S. Bento, K.A. Thomson, Ö.L. Gülder, Soot formation and temperature field structure in laminar propane-air diffusion flames at elevated pressures, *Combust. Flame.* 145 (2006) 765–778. <https://doi.org/10.1016/j.combustflame.2006.01.010>.
- [40] H.G. Darabkhani, Y. Zhang, Methane diffusion flame dynamics at elevated pressures, *Combust. Sci. Technol.* 182 (2010) 231–251.
<https://doi.org/10.1080/00102200903418252>.

- [41] R.R. Skaggs, J.H. Miller, Tunable diode laser absorption measurements of carbon monoxide and temperature in a time-varying, methane/air, non-premixed flame, *Symp. Combust.* 26 (1996) 1181–1188. [https://doi.org/10.1016/S0082-0784\(96\)80334-1](https://doi.org/10.1016/S0082-0784(96)80334-1).
- [42] N.A. Magina, Dynamics of harmonically forced nonpremixed flames, Ph.D. Thesis, Georg. Inst. Technol. (2016).
- [43] C.R. Shaddix, J.E. Harrington, K.C. Smyth, Quantitative measurement of enhanced soot production in a flickering methane/air diffusion flame, *Combust. Flame.* 99 (1994) 723–732.
- [44] C.R. Kaplan, C.R. Shaddix, K.C. Smyth, Computations of enhanced soot production in time-varying CH₄/air diffusion flames, *Combust. Flame.* 106 (1996) 392–398. [https://doi.org/10.1016/0010-2180\(95\)00258-8](https://doi.org/10.1016/0010-2180(95)00258-8).
- [45] A.W. Strawa, B.J. Cantwell, Investigation of an excited jet diffusion flame at elevated pressure, *J. Fluid Mech.* 200 (1989) 309–336. <https://doi.org/10.1017/S0022112089000674>.
- [46] J. Carpio, M. Sanchez-Sanz, E. Fernández-Tarrazo, Pinch-off in forced and non-forced, buoyant laminar jet diffusion flames, *Combust. Flame.* 159 (2012) 161–169. <https://doi.org/10.1016/j.combustflame.2011.06.008>.
- [47] Y. Gao, X. Yang, C. Fu, Y. Yang, Z. Li, H. Zhang, F. Qi, 10 kHz simultaneous PIV/PLIF study of the diffusion flame response to periodic acoustic forcing, *Appl. Opt.* 58 (2019) C112–C120. <https://doi.org/10.1364/ao.58.00c112>.
- [48] C. Fu, X. Yang, Z. Li, H. Zhang, Y. Yang, Y. Gao, Experimental investigation on an acoustically forced flame with simultaneous high-speed LII and stereo PIV at 20 kHz, *Appl. Opt.* 58 (2019) C104–C111. <https://doi.org/10.1364/ao.58.00c104>.
- [49] M. Tyagi, N. Jamadar, S.R. Chakravarthy, Oscillatory response of an idealized two-dimensional diffusion flame: Analytical and numerical study, *Combust. Flame.* 149 (2007) 271–285. <https://doi.org/10.1016/j.combustflame.2006.12.020>.
- [50] G.F. Carrier, F.E. Fendell, F.E. Marble, The effect of strain rate on diffusion flames, *SIAM J. Appl. Math.* 28 (1975) 463–500. <https://doi.org/10.1137/0130047>.
- [51] T. Kim, M. Ahn, J. Hwang, S. Kim, Y. Yoon, The experimental investigation on the response of the Burke-Schumann flame to acoustic excitation, *Proc. Combust. Inst.* 36 (2017) 1629–1636. <https://doi.org/10.1016/j.proci.2016.06.116>.

- [52] J.M. Donbar, J.F. Driscoll, C.D. Carter, Strain rates measured along the wrinkled flame contour within turbulent non-premixed jet flames, *Combust. Flame*. 125 (2001) 1239–1257. [https://doi.org/10.1016/S0010-2180\(01\)00246-2](https://doi.org/10.1016/S0010-2180(01)00246-2).
- [53] S.P. Burke, T.E.W. Schumann, Diffusion flames, *Ind. Eng. Chem.* 20 (1928) 998–1004. <https://doi.org/10.1021/ie50226a005>.
- [54] T. Kim, M. Ahn, J. Hwang, S. Kim, Y. Yoon, The experimental investigation on the response of the Burke-Schumann flame to acoustic excitation, *Proc. Combust. Inst.* 36 (2017) 1629–1636. <https://doi.org/10.1016/j.proci.2016.06.116>.
- [55] T. Kim, M. Ahn, D. Lim, Y. Yoon, Velocity and mass diffusivity effects on the linear and nonlinear phenomena of the Burke-Schumann flame with acoustic excitation, *J. Mech. Sci. Technol.* 33 (2019) 3019–3029. <https://doi.org/10.1007/s12206-019-0552-2>.
- [56] N. Magina, V. Acharya, T. Sun, T. Lieuwen, Propagation, dissipation, and dispersion of disturbances on harmonically forced, non-premixed flames, *Proc. Combust. Inst.* 35 (2015) 1097–1105. <https://doi.org/10.1016/j.proci.2014.07.050>.
- [57] A.M. Steinberg, I. Boxx, M. Stöhr, C.D. Carter, W. Meier, Flow-flame interactions causing acoustically coupled heat release fluctuations in a thermo-acoustically unstable gas turbine model combustor, *Combust. Flame*. 157 (2010) 2250–2266. <https://doi.org/10.1016/j.combustflame.2010.07.011>.
- [58] J.M. Seitzman, A. Üngüt, P.H. Paul, R.K. Hanson, Imaging and characterization of OH structures in a turbulent nonpremixed flame, *Symp. Combust.* 23 (1991) 637–644. [https://doi.org/10.1016/S0082-0784\(06\)80311-5](https://doi.org/10.1016/S0082-0784(06)80311-5).
- [59] S.R. Turns, *An introduction to combustion: concepts and applications* (2nd edition), 2000. <https://doi.org/10.1016/j.ijhydene.2008.07.121>.
- [60] P. Petersson, R. Wellander, J. Olofsson, H. Carlsson, C. Carlsson, B.B. Watz, N. Boetkjaer, M. Richter, M. Aldén, L. Fuchs, X. Bai, Simultaneous high-speed PIV and OH PLIF measurements and modal analysis for investigating flame-flow interaction in a low swirl flame, *16th Int Symp Appl. Laser Tech. to Fluid Mech.* (2012) 9–12.
- [61] Z. Li, J. Rosell, M. Aldén, M. Richter, Simultaneous Burst Imaging of Dual Species Using Planar Laser-Induced Fluorescence at 50 kHz in Turbulent Premixed Flames, *Appl. Spectrosc.* 71 (2017) 1363–1367.

- <https://doi.org/10.1177/0003702816678866>.
- [62] A.M. Steinberg, J.F. Driscoll, Straining and wrinkling processes during turbulence-premixed flame interaction measured using temporally-resolved diagnostics, *Combust. Flame*. 156 (2009) 2285–2306.
<https://doi.org/10.1016/j.combustflame.2009.06.024>.
 - [63] A.M. Steinberg, C.M. Arndt, W. Meier, Parametric study of vortex structures and their dynamics in swirl-stabilized combustion, *Proc. Combust. Inst.* 34 (2013) 3117–3125. <https://doi.org/10.1016/j.proci.2012.05.015>.
 - [64] A.M. Steinberg, B. Coriton, J.H. Frank, Influence of combustion on principal strain-rate transport in turbulent premixed flames, *Proc. Combust. Inst.* 35 (2015) 1287–1294. <https://doi.org/10.1016/j.proci.2014.06.089>.
 - [65] C. Fu, X. Yang, Z. Li, H. Zhang, Y. Yang, Y. Gao, Experimental investigation on an acoustically forced flame with simultaneous high-speed LII and stereo PIV at 20 kHz, *Appl. Opt.* 58 (2019) C104. <https://doi.org/10.1364/ao.58.00c104>.
 - [66] X. Yang, C. Fu, G. Wang, Z. Li, T. Li, Y. Gao, Simultaneous high-speed SO₂ PLIF imaging and stereo-PIV measurements in premixed swirling flame at 20 kHz, *Appl. Opt.* 58 (2019) C121. <https://doi.org/10.1364/ao.58.00c121>.
 - [67] J. Zhang, A. Ratner, Experimental study on the excitation of thermoacoustic instability of hydrogen-methane/air premixed flames under atmospheric and elevated pressure conditions, *Int. J. Hydrogen Energy*. 44 (2019) 21324–21335. <https://doi.org/10.1016/j.ijhydene.2019.06.142>.
 - [68] O. Lammel, H. Ax, L. Rainer, W. Meier, M. Aigner, D.-Stuttgart, J. Heinze, Detailed Investigation of Flame Stabilization, *Proc. Asme Turbo Expo 2017*. 140 (2017) 1–13. <https://doi.org/10.1115/1.4038126>.
 - [69] C.M. Arndt, R. Schießl, W. Meier, OH planar laser-induced fluorescence measurements with high spatio-temporal resolution for the study of auto-ignition, *Appl. Opt.* 58 (2019) C14. <https://doi.org/10.1364/ao.58.000c14>.
 - [70] K. Ahn, J.H. Kim, Y. Yoon, Application of PIV to Over-Expanded Supersonic Flows: Possibilities and Limits, *J. Vis.* 6 (2003) 353–361. <https://doi.org/10.1007/BF03181742>.
 - [71] G. Pont, C.P. Cadou, A.R. Karagozian, O.I. Smith, Emissions reduction and pyrolysis gas destruction in an acoustically driven dump combustor, *Combust.*

- Flame. 113 (1998) 249–257. [https://doi.org/10.1016/S0010-2180\(97\)00172-7](https://doi.org/10.1016/S0010-2180(97)00172-7).
- [72] R.H. Chen, J.F. Driscoll, Nitric oxide levels of jet diffusion flames: Effects of coaxial air and other mixing parameters, *Symp. Combust.* 23 (1990) 281–288. [https://doi.org/10.1016/S0082-0784\(06\)80271-7](https://doi.org/10.1016/S0082-0784(06)80271-7).
- [73] W. Lang, T. Poinso, S. Candel, Active control of combustion instability, *Combust. Flame.* 70 (1987) 281–289. <https://doi.org/10.1109/CHICC.2008.4605146>.
- [74] T. Lieuwen, H. Torres, C. Johnson, B.T. Zinn, A mechanism of combustion instability in lean premixed gas turbine combustors, *J. Eng. Gas Turbines Power.* 123 (2001) 182–189. <https://doi.org/10.1115/1.1339002>.
- [75] K.T. Kim, D.A. Santavicca, Interference mechanisms of acoustic/convective disturbances in a swirl-stabilized lean-premixed combustor, *Combust. Flame.* 160 (2013) 1441–1457. <https://doi.org/10.1016/j.combustflame.2013.02.022>.
- [76] V. Yang, W. Anderson, *Liquid Rocket Engine Combustion Instability*, 1995. <https://doi.org/10.2514/4.866371>.
- [77] V.G. Bazarov, V. Yang, Liquid-propellant rocket engine injector dynamics, *J. Propuls. Power.* 14 (1998) 797–806. <https://doi.org/10.2514/2.5343>.
- [78] H. Zhou, Z. Liu, C. Tao, M. Zhou, Passive Suppression of Self-Excited Combustion Instabilities in Liquid Spray Flame Using Microperforated Plate, *J. Eng. Gas Turbines Power.* 142 (2020) 1–12. <https://doi.org/10.1115/1.4047768>.
- [79] H. Zhou, Z. Liu, C. Tao, M. Zhou, Mitigating self-excited thermoacoustic oscillations in a liquid fuel combustor using dual perforated plates, *J. Acoust. Soc. Am.* 148 (2020) 1756–1766. <https://doi.org/10.1121/10.0002007>.
- [80] H. Zhou, Z. Liu, H. Fang, C. Tao, M. Zhou, L. Hu, Attenuation effects of perforated plates with heterogeneously distributed holes on combustion instability in a spray flame combustor, *J. Mech. Sci. Technol.* 34 (2020) 4865–4875. <https://doi.org/10.1007/s12206-020-1042-2>.
- [81] S. Sarkar, K.G. Lore, S. Sarkar, V. Ramanan, S.R. Chakravarthy, S. Phoha, A. Ray, Early detection of combustion instability from hi-speed flame images via deep learning and symbolic time series analysis, *Proc. Annu. Conf. Progn. Heal. Manag. Soc. PHM.* (2015).
- [82] A. Akintayo, K.G. Lore, S. Sarkar, S. Sarkar, Prognostics of combustion instabilities from Hi-speed flame video using a deep convolutional selective

- autoencoder, *Int. J. Progn. Heal. Manag.* 7 (2016) 1–14.
<https://doi.org/10.36001/ijphm.2016.v7i4.2461>.
- [83] T. Kobayashi, S. Murayama, T. Hachijo, H. Gotoda, Early detection of thermoacoustic combustion instability using a methodology combining complex networks and machine learning, *Phys. Rev. Appl.* 11 (2019).
<https://doi.org/10.1103/PhysRevApplied.11.064034>.
- [84] O. Hwang, M.C. Lee, W. Weng, Y. Zhang, Z. Li, Development of novel ultrasonic temperature measurement technology for combustion gas as a potential indicator of combustion instability diagnostics, *Appl. Therm. Eng.* 159 (2019) 113905.
<https://doi.org/10.1016/j.applthermaleng.2019.113905>.
- [85] G. Kelsall, C. Troger, Prediction and control of combustion instabilities in industrial gas turbines, *Appl. Therm. Eng.* 24 (2004) 1571–1582.
<https://doi.org/10.1016/j.applthermaleng.2003.10.025>.
- [86] F. Duchaine, F. Boudy, D. Durox, T. Poinso, Sensitivity analysis of transfer functions of laminar flames, *Combust. Flame.* 158 (2011) 2384–2394.
<https://doi.org/10.1016/j.combustflame.2011.05.013>.
- [87] W.J. Song, D.J. Cha, Temporal kurtosis of dynamic pressure signal as a quantitative measure of combustion instability, *Appl. Therm. Eng.* 104 (2016) 577–586. <https://doi.org/10.1016/j.applthermaleng.2016.05.094>.
- [88] T. Poinso, Prediction and control of combustion instabilities in real engines, *Proc. Combust. Inst.* 36 (2017) 1–28. <https://doi.org/10.1016/j.proci.2016.05.007>.
- [89] L. Crocco, Aspects of combustion stability in liquid propellant rocket motors part I: fundamentals. low frequency instability with monopropellants, *J. Am. Rocket Soc.* 21 (1951) 163–178. <https://doi.org/10.2514/8.4393>.
- [90] L. Crocco, Research on combustion instability in liquid propellant rockets, *Symp. Combust.* 12 (1969) 85–99. [https://doi.org/10.1016/S0082-0784\(69\)80394-2](https://doi.org/10.1016/S0082-0784(69)80394-2).
- [91] H.S. Tsien, The transfer functions of rocket nozzles, *J. Am. Rocket Soc.* 22 (1952) 139–143. <https://doi.org/10.1016/B978-0-12-398277-3.50038-5>.
- [92] T. Schuller, S. Ducruix, D. Durox, S. Candel, Modeling tools for the prediction of premixed flame transfer functions, *Proc. Combust. Inst.* 29 (2002) 107–113.
[https://doi.org/10.1016/S1540-7489\(02\)80018-9](https://doi.org/10.1016/S1540-7489(02)80018-9).
- [93] J.H. Cho, T. Lieuwen, Laminar premixed flame response to equivalence ratio

- p>oscillations,
- Combust. Flame*
- . 140 (2005) 116–129.
-
- <https://doi.org/10.1016/j.combustflame.2004.10.008>
- .
- [94] P. Palies, D. Durox, T. Schuller, S. Candel, Nonlinear combustion instability analysis based on the flame describing function applied to turbulent premixed swirling flames, *Combust. Flame*. 158 (2011) 1980–1991.
<https://doi.org/10.1016/j.combustflame.2011.02.012>.
- [95] S. Oh, J. Kim, Y. Kim, FDF-based combustion instability analysis for evolution of mode shapes and eigenfrequency in the multiple flame burner, *Appl. Therm. Eng.* 124 (2017) 695–706. <https://doi.org/10.1016/j.applthermaleng.2017.06.084>.
- [96] B. Varoquié, J.P. L  gier, F. Lacas, D. Veynante, T. Poinsot, Experimental analysis and large eddy simulation to determine the response of non-premixed flames submitted to acoustic forcing, *Proc. Combust. Inst.* 29 (2002) 1965–1970.
[https://doi.org/10.1016/S1540-7489\(02\)80239-5](https://doi.org/10.1016/S1540-7489(02)80239-5).
- [97] D. Durox, T. Schuller, N. Noiray, S. Candel, Experimental analysis of nonlinear flame transfer functions for different flame geometries, *Proc. Combust. Inst.* 32 I (2009) 1391–1398. <https://doi.org/10.1016/j.proci.2008.06.204>.
- [98] S.K. Dhanuka, J.E. Temme, J.F. Driscoll, Unsteady aspects of lean premixed prevaporized gas turbine combustors: Flame-flame interactions, *J. Propuls. Power*. 27 (2011) 631–641. <https://doi.org/10.2514/1.B34001>.
- [99] C. Li, H. Tang, L. Jing, M. Zhu, Investigations of the stabilities of piloted flames using blast furnace gas, *J. Eng. Gas Turbines Power*. 138 (2016).
<https://doi.org/10.1115/1.4031348>.
- [100] C.J. Sung, C.K. Law, Structural sensitivity, response, and extinction of diffusion and premixed flames in oscillating counterflow, *Combust. Flame*. 123 (2000) 375–388. [https://doi.org/10.1016/S0010-2180\(00\)00175-9](https://doi.org/10.1016/S0010-2180(00)00175-9).
- [101] D. Durox, T. Yuan, F. Baillot, J.M. Most, Premixed and diffusion flames in a centrifuge, *Combust. Flame*. 102 (1995) 501–511. [https://doi.org/10.1016/0010-2180\(95\)00051-7](https://doi.org/10.1016/0010-2180(95)00051-7).
- [102] A.M. Steinberg, I. Boxx, M. St  hr, C.D. Carter, W. Meier, Flow-flame interactions causing acoustically coupled heat release fluctuations in a thermo-acoustically unstable gas turbine model combustor, *Combust. Flame*. 157 (2010) 2250–2266.
<https://doi.org/10.1016/j.combustflame.2010.07.011>.

- [103] H. Gotoda, K. Maeda, T. Ueda, R.K. Cheng, Periodic motion of a Bunsen flame tip with burner rotation, *Combust. Flame*. 134 (2003) 67–79.
[https://doi.org/10.1016/S0010-2180\(03\)00082-8](https://doi.org/10.1016/S0010-2180(03)00082-8).
- [104] M. Ahn, D. Lim, T. Kim, Y. Yoon, Pinch-off process of Burke–Schumann flame under acoustic excitation, *Combust. Flame*. 231 (2021) 111478.
<https://doi.org/10.1016/j.combustflame.2021.111478>.
- [105] H. Gotoda, T. Ueda, Transition from periodic to non-periodic motion of a Bunsen-type premixed flame tip with burner rotation, *Proc. Combust. Inst.* 29 (2002) 1503–1509. [https://doi.org/10.1016/S1540-7489\(02\)80184-5](https://doi.org/10.1016/S1540-7489(02)80184-5).
- [106] L. Kabiraj, R.I. Sujith, Nonlinear self-excited thermoacoustic oscillations: Intermittency and flame blowout, *J. Fluid Mech.* 713 (2012) 376–397.
<https://doi.org/10.1017/jfm.2012.463>.
- [107] M. Kim, Y. Choi, J. Oh, Y. Yoon, Flame-vortex interaction and mixing behaviors of turbulent non-premixed jet flames under acoustic forcing, *Combust. Flame*. 156 (2009) 2252–2263. <https://doi.org/10.1016/j.combustflame.2009.08.004>.
- [108] A. Cuquel, D. Durox, T. Schuller, Impact of flame base dynamics on the non-linear frequency response of conical flames, *Comptes Rendus - Mec.* 341 (2013) 171–180. <https://doi.org/10.1016/j.crme.2012.11.004>.
- [109] V. Acharya, Shreekrishna, D.H. Shin, T. Lieuwen, Swirl effects on harmonically excited, premixed flame kinematics, *Combust. Flame*. 159 (2012) 1139–1150.
<https://doi.org/10.1016/j.combustflame.2011.09.015>.
- [110] K. Lakshminarasimhan, M.D. Ryan, N.T. Clemens, O.A. Ezekoye, Mixing characteristics in strongly forced non-premixed methane jet flames, *Proc. Combust. Inst.* 31 (2007) 1617–1624. <https://doi.org/10.1016/j.proci.2006.08.095>.
- [111] K. Lakshminarasimhan, N.T. Clemens, O.A. Ezekoye, Characteristics of strongly-forced turbulent jets and non-premixed jet flames, *Exp. Fluids*. 41 (2006) 523–542.
<https://doi.org/10.1007/s00348-006-0164-3>.
- [112] N.A. Magina, T.C. Lieuwen, Effect of axial diffusion on the response of diffusion flames to axial flow perturbations, *Combust. Flame*. 167 (2016) 395–408.
<https://doi.org/10.1016/j.combustflame.2016.01.012>.
- [113] A. Orchini, S.J. Illingworth, M.P. Juniper, Frequency domain and time domain analysis of thermoacoustic oscillations with wave-based acoustics, *J. Fluid Mech.*

- 775 (2015) 387–414. <https://doi.org/10.1017/jfm.2015.139>.
- [114] S. Park, Y. Kim, Effects of nitrogen dilution on the NO_x formation characteristics of CH₄/CO/H₂ syngas counterflow non-premixed flames, *Int. J. Hydrogen Energy*. 42 (2017) 11945–11961. <https://doi.org/10.1016/j.ijhydene.2017.02.080>.
- [115] M. Dutka, M. Ditaranto, T. Løvås, NO_x emissions and turbulent flow field in a partially premixed bluff body burner with CH₄ and H₂ fuels, *Int. J. Hydrogen Energy*. 41 (2016) 12397–12410. <https://doi.org/10.1016/j.ijhydene.2016.05.154>.
- [116] D. Bartos, M. Sirignano, M.J. Dunn, A. D'Anna, A.R. Masri, Soot inception in laminar coflow diffusion flames, *Combust. Flame*. 205 (2019) 180–192. <https://doi.org/10.1016/j.combustflame.2019.03.026>.
- [117] I. Esquivia-Dano, H.T. Nguyen, D. Escudie, Influence of a bluff-body's shape on the stabilization regime of non-premixed flames, *Combust. Flame*. 127 (2001) 2167–2180. [https://doi.org/10.1016/S0010-2180\(01\)00318-2](https://doi.org/10.1016/S0010-2180(01)00318-2).
- [118] K.F. Zohra, A. Mounir, C. Salah, Numerical simulation of CH₄-H₂-AIR non-premixed flame stabilized by a bluff body, *Energy Procedia*. 139 (2017) 530–536. <https://doi.org/10.1016/j.egypro.2017.11.249>.
- [119] V. Raman, H. Pitsch, Large-eddy simulation of a bluff-body-stabilized non-premixed flame using a recursive filter-refinement procedure, *Combust. Flame*. 142 (2005) 329–347. <https://doi.org/10.1016/j.combustflame.2005.03.014>.
- [120] N. Noiray, D. Durox, T. Schuller, S. Candel, A unified framework for nonlinear combustion instability analysis based on the flame describing function, *J. Fluid Mech*. 615 (2008) 139–167. <https://doi.org/10.1017/S0022112008003613>.
- [121] S.P. Burke, T.E.W. Schumann, Diffusion flames, *Ind. Eng. Chem*. 20 (1928) 998–1004. <https://doi.org/10.1021/ie50226a005>.
- [122] W.R. Boyette, T.F. Guiberti, G. Magnotti, W.L. Roberts, Structure of turbulent nonpremixed syngas flames at high pressure, *Proc. Combust. Inst*. 37 (2019) 2207–2214. <https://doi.org/10.1016/j.proci.2018.09.004>.
- [123] L. Muñoz, M.G. Mungal, Effects of heat release and buoyancy on flow structure and entrainment in turbulent nonpremixed flames, *Combust. Flame*. 126 (2001) 1402–1420. [https://doi.org/10.1016/S0010-2180\(01\)00253-X](https://doi.org/10.1016/S0010-2180(01)00253-X).
- [124] D.B. Bryant, K.A. Whilden, S.A. Socolofsky, K.A. Chang, Formation of tidal starting-jet vortices through idealized barotropic inlets with finite length, *Environ.*

- Fluid Mech. 12 (2012) 301–319. <https://doi.org/10.1007/s10652-012-9237-4>.
- [125] C.K. Law, D.L. Zhu, G. Yu, Propagation and extinction of stretched premixed flames, *Symp. Combust.* 21 (1986) 1419–1426. [https://doi.org/10.1016/S0082-0784\(88\)80374-6](https://doi.org/10.1016/S0082-0784(88)80374-6).
- [126] V.R. Katta, C.D. Carter, G.J. Fiechtner, W.M. Roquemore, J.R. Gord, J.C. Rolon, Interaction of a vortex with a flat flame formed between opposing jets of hydrogen and air, *Symp. Combust.* 27 (1998) 587–594. [https://doi.org/10.1016/S0082-0784\(98\)80450-5](https://doi.org/10.1016/S0082-0784(98)80450-5).
- [127] R. Jarpala, N. Burle, M. Voleti, R. Sadanandan, Effect of swirl on the flame dynamics and pollutant emissions in an ultra-lean non-premixed model gas turbine burner, *Combust. Sci. Technol.* 189 (2017) 1832–1848. <https://doi.org/10.1080/00102202.2017.1333500>.
- [128] W. Wang, A.E. Karatas, C.P.T. Groth, Ö.L. Gülder, Experimental and numerical study of laminar flame extinction for syngas and syngas-methane blends, *Combust. Sci. Technol.* 190 (2018) 1455–1471. <https://doi.org/10.1080/00102202.2018.1452128>.
- [129] L.M. Das, Hydrogen-oxygen reaction mechanism and its implication to hydrogen engine combustion, *Int. J. Hydrogen Energy.* 21 (1996) 703–715. [https://doi.org/10.1016/0360-3199\(95\)00138-7](https://doi.org/10.1016/0360-3199(95)00138-7).
- [130] G. Dahl, F. Suttrop, Engine control and low-NO_x combustion for hydrogen fuelled aircraft gas turbines, 23 (1998) 695–704.
- [131] J.W. Heffel, NO_x emission and performance data for a hydrogen fueled internal combustion engine at 1500 rpm using exhaust gas recirculation, *Int. J. Hydrogen Energy.* 28 (2003) 901–908. [https://doi.org/10.1016/S0360-3199\(02\)00157-X](https://doi.org/10.1016/S0360-3199(02)00157-X).
- [132] J.W. Heffel, NO_x emission reduction in a hydrogen fueled internal combustion engine at 3000 rpm using exhaust gas recirculation, *Int. J. Hydrogen Energy.* 28 (2003) 1285–1292. [https://doi.org/10.1016/S0360-3199\(02\)00289-6](https://doi.org/10.1016/S0360-3199(02)00289-6).
- [133] N.A. Samiran, J.H. Ng, M.N. Mohd Jaafar, A. Valera-Medina, C.T. Chong, H₂-rich syngas strategy to reduce NO_x and CO emissions and improve stability limits under premixed swirl combustion mode, *Int. J. Hydrogen Energy.* 41 (2016) 19243–19255. <https://doi.org/10.1016/j.ijhydene.2016.08.095>.
- [134] H.H.W. Funke, N. Beckmann, S. Abanteriba, An overview on dry low NO_x

- micromix combustor development for hydrogen-rich gas turbine applications, *Int. J. Hydrogen Energy*. 44 (2019) 6978–6990.
<https://doi.org/10.1016/j.ijhydene.2019.01.161>.
- [135] Z. Li, S. Li, Kinetics modeling of NO_x emissions characteristics of a NH₃/H₂ fueled gas turbine combustor, *Int. J. Hydrogen Energy*. 46 (2021) 4526–4537.
<https://doi.org/10.1016/j.ijhydene.2020.11.024>.
- [136] Z. Wang, S. Zhou, Y. Feng, Y. Zhu, Research of NO_x reduction on a low-speed two-stroke marine diesel engine by using EGR (exhaust gas recirculation)–CB (cylinder bypass) and EGB (exhaust gas bypass), *Int. J. Hydrogen Energy*. 42 (2017) 19337–19345. <https://doi.org/10.1016/j.ijhydene.2017.06.009>.
- [137] S. Zhou, R. Gao, Y. Feng, Y. Zhu, Evaluation of Miller cycle and fuel injection direction strategies for low NO_x emission in marine two-stroke engine, *Int. J. Hydrogen Energy*. 42 (2017) 20351–20360.
<https://doi.org/10.1016/j.ijhydene.2017.06.020>.
- [138] L. Zhu, B. Li, A. Li, W. Ji, Y. Qian, X. Lu, Z. Huang, Effects of fuel reforming on large-bore low-speed two-stroke dual fuel marine engine combined with EGR and injection strategy, *Int. J. Hydrogen Energy*. 45 (2020) 29505–29517.
<https://doi.org/10.1016/j.ijhydene.2020.07.266>.
- [139] A. Abu-Jrai, A. Tsolakis, A. Megaritis, The influence of H₂ and CO on diesel engine combustion characteristics, exhaust gas emissions, and after treatment selective catalytic NO_x reduction, *Int. J. Hydrogen Energy*. 32 (2007) 3565–3571.
<https://doi.org/10.1016/j.ijhydene.2007.02.014>.
- [140] I.A. Resitoglu, A. Keskin, Hydrogen applications in selective catalytic reduction of NO_x emissions from diesel engines, *Int. J. Hydrogen Energy*. 42 (2017) 23389–23394. <https://doi.org/10.1016/j.ijhydene.2017.02.011>.
- [141] P. Dimitriou, M. Kumar, T. Tsujimura, Y. Suzuki, Combustion and emission characteristics of a hydrogen-diesel dual-fuel engine, *Int. J. Hydrogen Energy*. 43 (2018) 13605–13617. <https://doi.org/10.1016/j.ijhydene.2018.05.062>.
- [142] O. Delabroy, F. Lacas, T. Poinsot, S. Candel, T. Hoffmann, J. Hermann, S. Gleis, D. Vortmeyer, A study of NO_x reduction by acoustic excitation in a liquid fueled burner, *Combust. Sci. Technol.* 119 (1996) 397–408.
<https://doi.org/10.1080/00102209608952007>.

- [143] Y.C. Chao, Y.W. Huang, D.C. Wu, Feasibility of controlling NOX emissions from a jet flame by acoustic excitation, *Combust. Sci. Technol.* 158 (2000) 461–484.
<https://doi.org/10.1080/00102200008947345>.
- [144] J. Carpio, M. Sanchez-Sanz, E. Fernández-Tarrazo, Pinch-off in forced and non-forced, buoyant laminar jet diffusion flames, *Combust. Flame.* 159 (2012) 161–169.
<https://doi.org/10.1016/j.combustflame.2011.06.008>.
- [145] J.F. Driscoll, R.H. Chen, Y. Yoon, Nitric oxide levels of turbulent jet diffusion flames: Effects of residence time and damkohler number, *Combust. Flame.* 88 (1992) 37–49. [https://doi.org/10.1016/0010-2180\(92\)90005-A](https://doi.org/10.1016/0010-2180(92)90005-A).
- [146] C.E. Baukal, P.B. Eleazer, Quantifying NOx for industrial combustion processes, *J. Air Waste Manag. Assoc.* 48 (1998) 52–58.
<https://doi.org/10.1080/10473289.1998.10463664>.
- [147] K. Deng, M. Wang, Z. Shen, Y. Hu, Y. Zhong, Effect of different acoustic parameters on NOx emissions of partially premixed flame, *Appl. Sci.* 9 (2019) 1490. <https://doi.org/10.3390/APP9071490>.
- [148] J.A. Curcio, H.S. Stewart, C.C. Petty, A Method for the Determination of Flame Temperature from Emission in the Ultraviolet OH Band, *J. Opt. Soc. Am.* 41 (1951) 173–179.
- [149] C. Mirat, D. Durox, T. Schuller, Stability analysis of a swirl spray combustor based on flame describing function, *Proc. Combust. Inst.* 35 (2015) 3291–3298.
<https://doi.org/10.1016/j.proci.2014.08.020>.
- [150] J. Matthes, P. Waibel, M. Vogelbacher, H.J. Gehrman, H.B. Keller, A new camera-based method for measuring the flame stability of non-oscillating and oscillating combustions, *Exp. Therm. Fluid Sci.* 105 (2019) 27–34.
<https://doi.org/10.1016/j.expthermflusci.2019.03.008>.
- [151] B. Jang, C. Oh, S. Ahn, Y. Kim, J. Park, M. Choi, Y. Sung, Nitric oxide emission reduction and thermal characteristics of fuel-pulsed oscillating combustion in an industrial burner system, *Energy.* 216 (2021) 119263.
<https://doi.org/10.1016/j.energy.2020.119263>.
- [152] H.C. Cho, K.W. Cho, H.J. Kim, NOx emission characteristics in radiant tube burner with oscillating combustion technology, *J. Energy Power Eng.* 32 (2011) 100–106.
<https://doi.org/10.3795/KSME-B.2008.32.2.100>.

- [153] N. Magina, V. Acharya, T. Lieuwen, Forced response of laminar non-premixed jet flames, *Prog. Energy Combust. Sci.* 70 (2019) 89–118.
<https://doi.org/10.1016/j.pecs.2018.08.001>.
- [154] D. Wendt, S. Sthle, J.A. Piotrowski, H. Wendt, M. Thielmann, H. Jakob, W. Kowalczyk, Comparison of flow dynamics of Perimount Magna and Magna Ease aortic valve prostheses, *Biomed. Tech.* 57 (2012) 97–106.
<https://doi.org/10.1515/bmt-2011-0076>.

초 록

연소불안정의 발생 원인과 메커니즘은 현재까지 정확하게 규명되지 않았으나 반응물의 유동 섭동, 열방출량 섭동, 연소실의 음향학적 경계에 의한 섭동의 상호작용에 의해 발생 유무가 결정된다고 알려져 있다. 위의 세 가지 섭동이 양성 피드백 루프(positive feedback loop)를 형성하면 연소불안정이 발생할 확률이 높아지며, 음성 피드백 루프(negative feedback loop)를 형성하면 그 확률이 낮아지는 것으로 알려져 있다. 따라서 연소불안정 발생 저감을 위해 연소불안정 발생 조건 및 인자를 파악하는 것은 필수적이다. 본 연구에서는 연소불안정 현상의 인자 중 열 방출량 섭동과 속도 섭동의 상호관계에 대한 연구를 수행하였으며, 특정 음향 가진 조건에서 화염이 끊기는 현상인 pinch-off 화염에 대해 OH PLIF와 PIV 레이저 동시계측을 통해 발생 메커니즘을 실험적으로 규명하였으며, pinch-off 화염과 nonpinch-off 화염의 NOx 배출 특성, 연료와 공기의 유동경계층에 대한 유동 특성 분석을 수행하였다. 음향 가진 발생을 위해서 스피커를 활용하였으며, 화염구조 분석을 위해서 OH* 자발광과 OH-PLIF 레이저 계측기법을 활용하였으며, 유동장 특성분석을 위해 OH-PLIF와 PIV 동시계측을 활용하였다. 열 방출량 계측을 위해서 광전자증폭관(Photo Multiplier Tube, PMT)를 활용하였으며 이를 통해 화염전달함수를 계측하였다.

연소불안정 예측을 위해 음향 가진에 따른 비예혼합화염과 예혼합화염의 응답특성 및 동특성 비교 연구를 수행하였다. 다른 연소 반응을 가진 두 화염은 음향 가진에 따라 동적거동 특성이 상이하다. 비예혼합화염은 화염 면에서 음향학적 파동이 투영되며, 펄럭이는 동적 거동 특성이며 화염 끝 단이 열린 화염형상이다. 반면에 단일 노즐인 예혼합화염은 코니컬 화염(conical flame)의 형태로 수직으로 크게 섭동한다. 비예혼합화염은 가진주파수 증가에 따라서 화염 면의 모듈레이션(modulation) 개수가 증가할 뿐 화염 구조는 크게 변하지 않지만, 예혼합화염은 가진주파수와 속도섭동강도에 따라 다양한 화염 구조가 나타난다. 음향 가진 시 두 화염의 열 방출량 측정을 통해 화염전달함수를 분석한 결과 비예혼합화염은 비선형적인 결과를 나타내었으며, 예혼합화염은 선형적인 결과를 나타내었다. 화염길이와 스트로울 수(Strouhal number)를 도입하여 열방출량과 화염구조의 상관관계 분석을 수행하였으며, 수치해석적 연구와 비교하였다. 비예혼합화염은 20%이상의 속도섭동에서 수치해석결과와 일치하며, 비선형성을 검증하였으며, 예혼합화염은 일부 스트로울 수에서 수치해석 결과와 다르다. 이는 스트로울 수를 계산할 때, 화염 면 곡률, 화염 전파 속도, 화염 끝단 형상 등을 고려한 스트로울 수에 도입해야 함을 확인하였다.

벽-유만 화염의 한가지 케이스인 비예혼화염에서 음향 가진 시 속도섭동강도와 가진주파수에 따른 다양한 화염 구조를 관찰하였다. 일정 가진주파수와 속도섭동강도 범위에서는 화염이 끊기는 pinch-off 화염이 나타남을 확인하였다. pinch-off 화염은 화염이 끊기는 현상으로 정의하며 노즐에 부착된 화염은 메인(main) 화염과 떨어져 나간 화염을 포켓(pocket) 화염으로 정의한다. Pinch-off 화염의 메커니즘 규명을 위해 OH PLIF&PIV 동시계측을 수행하였다. 가진 주파수와 속도섭동강도에 따른 화염 구조를 맵핑(mapping)하여 3가지 동적 거동으로 구별하였다. 낮은 주파수 범위에서는 화염이 상-하로 크게 섭동하는 flickering 화염이다. 중간 주파수 범위에서는 화염이 끊기는 pinch-off 화염, 그리고 높은 주파수 범위에서는 화염 면의 모들레이션이 생기는 wrinkled 화염으로 구별하였다. 비반응장 유동에서 음향 가진 시 조수 유동(tidal flow)에 의한 double dipole vortex을 미 산란(Mie scattering)으로 확인하였다. 반응장 유동의 화염이 pinch-off 시 vortical structure에 의한 공기 유입이 화염 변형을 야기함을 확인하였으며, 화염 목 부분에 강한 strain rate을 관찰하였다. 이에 따라 pinch-off flame은 vortical structure에 의한 외부 공기 유입과 강한 strain rate에 의한 상호작용임을 확인하였다.

pinch-off 화염의 떨어져나간 포켓 화염을 고려한 질소산화물(NOx), 일산화탄소(CO) 배출 특성 분석을 수행하였다. 질소산화물은 속도섭동강도 증가에 따라 배출량은 감소한다. 이는 속도섭동강도가 증가하면 연료와 산화제 혼합도가 증가하기 때문이며 혼합이 잘 이루어져 완전연소하면 질소산화물 배출이 적어진다. 반면에 일산화탄소는 속도섭동강도 증가에 따라 배출이 증가하는 특성을 나타내었지만, 그 배출량이 매우 작음을 확인하였다. 배출특성의 지표인 EINOx(Emission Index of NOx)와 화염체류시간(flame residence time) 분석을 위해서 pinch-off 화염의 높이를 주화염과 포켓화염으로 세분화하여 정의하였다. 세분화한 화염길리와 화염체류시간 분석 결과, 화염체류시간이 감소함에 따라 질소산화물 배출이 저감되는 경향은 일치하지만, 가진주파수에 따른 경향을 따르지는 않았다. 따라서 화염체류시간만으로 질소산화물 배출 특성을 분석하는데에 그 한계점이 있음을 밝혔다. 스트롤 수와 EINOx의 상관관계 분석 결과 스트롤 수가 다름에도 EINOx 배출이 같은 경향을 확인하였다. 이는 화염길리는 주화염 또는 포켓화염 어느 것을 선택하여도 경향성 분석에 무관함을 의미한다. 이러한 경향성 검증을 위해 화염체류시간으로 정규화한 EINOx가 $1/2$ -power를 잘 따르는 것을 확인하였다.

Pinch-off와 nonpinch-off조건에서 strain rate과 shear stress 상관관계 분석을

수행하였다. 연료와 공기 속도가 같아 이론적으로 shear stress가 없는 조건을 기준으로 연료와 공기 속도를 각각 변화시키며 shear stress를 생성하였다. 연료와 공기속도의 유동경계층 분석을 위해서 OH* 자발광과 PIV 동시계측을 수행하였다. 다양한 연료와 공기속도에 따라 pinch-off의 매핑을 수행하여 물리적인 경계를 확인하였다. 연료 속도 증가에 따른 pinch-off 조건에서 shear 효과가 증가함에 따라 strain rate가 기존 데이터에 비해 약 80% 증가하였으며, shear stress는 15% 증가하였다. 연료속도를 더 증가시켜 nonpinch-off 조건에서 계측한 결과 shear 효과는 더 증가하였지만 strain rate은 기존데이터와 비교했을 때 50% 감소하였고 shear stress는 3.3배 증가하였다. 공기속도 증가에 따른 nonpinch-off 조건에서 strain rate과 shear stress의 상관관계를 분석하여 경향성을 재검증하였다. 결과적으로 strain rate이 주요하게 영향을 미칠 때 shear stress는 감소되는 경향이며, shear stress는 pinch-off를 제어할 수 있는 파라미터로서 활용가능성을 확인하였다.

주요어: 비예혼합화염, Pinch-off 화염, 벽-슈만 화염, 예혼합화염, 음향 가진, 연소불안정, 화염전달합수, 화염 구조, OH 평면 레이저유도 형광 (PLIF), OH* 자발광, 입자 영상 유속계 (PIV), 레이저 동시계측, 질소산화물, 질소산화물 배출 인덱스 (EINOx), 화염체류시간, 유동변형율, 전단변형율

학 번: 2017-34984

Flame Response Characteristics of
Non-premixed Flames on Acoustic Excitation

비에혼합화염의 음향 가진에 따른 화염응답특성

지도교수 윤 영 빈

이 논문을 공학박사 학위논문으로 제출함

2021 년 11 월

서울대학교 대학원

기계항공공학부

안 명 근

안명근의 공학박사 학위논문을 인준함

2021 년 12 월

위 원 장 : 余載羽

부위원장 : 尹寧彬

위 원 : 李福植

위 원 : 孫采熏

위 원 : 金大植